COUPLING LIGHT AND MATTER IN METALLIC NANOPARTICLE ARRAYS

Said Rahimzadeh Kalaleh Rodriguez

The front cover shows a light extinction measurement of a metallic nanoparticle array covered by a dye-doped polymer layer. The avoided resonance crossing is due to the strong coupling between surface lattice resonances of the array and molecular excitations. The back cover shows an avoided crossing between bright and dark surface lattice resonances in the light extinction spectrum of a metallic nanoparticle array.

ISBN: 978-94-6259-270-4

A catalogue record is available from the Eindhoven University of Technology Library.

Coupling Light and Matter in Metallic Nanoparticle Arrays

PROEFSCHRIFT

ter verkrijging van de graad van doctor aan de Technische Universiteit
Eindhoven, op gezag van de rector magnificus prof.dr.ir. C.J. van Duijn,
voor een commissie aangewezen door het College voor Promoties, in het
openbaar te verdedigen op dinsdag 2 september 2014 om 16:00 uur

door

Said Rahimzadeh Kalaleh Rodriguez

geboren te Monterrey, Mexico

Dit proefschrift is goedgekeurd door de promotoren en de samenstelling van de promotiecommissie is als volgt:

voorzitter: prof.dr.ir. G.M.W. Kroesen
1e promotor: prof.dr. J. Gómez Rivas
2e promotor: prof.dr. A. Fiore
leden: prof.dr. F. J. García Vidal (Universidad Autonoma de Madrid)
prof.dr. S. Maier (Imperial College London)
prof.dr. A. Polman (Universiteit van Amsterdam)
prof.dr.ir. M.K. Smit
prof.dr. G.W. 't Hooft (Philips Research)

This work was supported by the Netherlands Foundation for Fundamental Research on Matter (FOM) and the Netherlands Organization for Scientific Research (NWO), and is part of an industrial partnership program between Philips and FOM.

To my family, especially Abbas, Veva, and Marina, with gratitude for their love and support

“Try and penetrate with our limited means the secrets of nature and you will find that, behind all the discernible laws and connections, there remains something subtle, intangible and inexplicable. Veneration for this force beyond anything that we can comprehend is my religion.”

- Albert Einstein, in “Einstein: His Life and Universe” by Walter Isaacson

Contents

CHAPTER 1

INTRODUCTION

The coupling of light and matter has marked the history of humankind. Our perception of the material world is assembled mostly through vision, for which light is the information-carrying field. In a scientific context, light has played an instrumental role in revealing the structures of which matter is composed, e.g. molecules, atoms, and electrons. Conversely, material structures have enabled us to discover the general laws governing the dynamics of light, e.g. refraction, reflection, and diffraction. Still, most of the time light and matter couple only weakly: they behave as separate entities, and we learn from one by probing it with the other. However, under exceptional circumstances light and matter can mix to an extent that they become indistinguishable. This is the essence of the strong light-matter coupling regime, which heralds the onset of fascinating effects that we shall explore in this thesis.

This chapter gives a general introduction to the phenomenon of light-matter coupling. We begin by examining the conditions determining the coupling strength. This calls for an understanding of the characteristic scales and properties of light and matter. For reasons that will become clear, our system of choice for studying and controlling the coupling of light and matter is a periodic array of resonant metallic nanostructures. Depending on the particular configuration, such an array can also couple to distinct optical modes. These include diffracted modes in the plane of the array, and guided modes in a dielectric slab. We will introduce in this chapter the basic physics underlying each one of these modes separately, and we will touch upon the physics that can emerge in case they mutually couple. Details of the coupled systems are left for subsequent chapters. Here we will highlight some of the important experimental and theoretical developments that have shaped the current scientific understanding of light-matter interactions, thereby placing ourselves in proper context. Finally, we will provide an outline for this thesis, which deals with the coupling of light and matter in metallic nanoparticle arrays, with an emphasis on its potential to modify light emission.

1.1 Characteristic scales and properties of light and matter

Light is both an electromagnetic wave and a particle. Therefore, to design material structures optimally coupled to light, it is essential to consider the length and energy scales characterizing light waves and particles (photons), respectively. For visible light in free-space, the wavelength λ is roughly 400-700 nm. From Planck's relation $E = hc/\lambda$, with h Planck's constant and c the speed of light in vacuum, it follows that the associated photon's energy range is 1.8-3.1 eV. Thus, polarizable objects with features of a few hundred nm in spatial extent and energetic (e.g. electronic) transitions of a few eV are a good starting point for controlling light.

In general, the strength of light-matter interaction depends on the following:

i. the properties of the material object, such as geometry, volume, electron density, and chemical composition,

ii. the properties of the light, such as polarization, frequency, and intensity,

iii. the properties of the configuration, such as angle of incidence, phase relationships when dealing with multiple interacting bodies, and the environment.

An optical resonance occurs when these factors contrive to maximize the response of a system. A resonance is never the consequence of one of the above sets of properties alone. It is always the interplay between the "intrinsic" properties of light and matter, and their configuration, which determines resonant behavior. Furthermore, the fact that we live in a causal world imposes strict restrictions on the frequency-dependent response of a resonant system integrated over the entire spectrum [1]. Since the origin and effects of optical resonances are central to this work, we proceed with a brief review of the related physics.

1.2 Optical resonance: The Lorentz oscillator

The theory of optical resonances is largely based on the monumental work of H. A. Lorentz. Lorentz postulated that matter, composed of point-like electric charges, responds harmonically to the electromagnetic field. An inspired discussion of this postulate and its consequences for optics is provided in a series of lectures delivered by Lorentz in 1906 [2]. For a modern treatment of optical resonances, we refer to Allen and Eberly [3]. To illustrate the Lorentzian mechanics, we consider the Hamiltonian of a collection of electric dipoles driven by an electric field E:

$$H = \frac{1}{2m}\sum_a (p_a^2 + (\omega_0 m r_a)^2 - e\sum_a r_a \cdot E(t, r_a). \tag{1.1}$$

p_a and r_a are the canonical momentum and position of the ath dipole, which is composed of a mass m with a charge e oscillating at a frequency ω_0 . Applying Hamilton's equations,

$$\dot{q} = \frac{\partial H}{\partial p} \quad \text{and} \quad \dot{p} = -\frac{\partial H}{\partial q} \tag{1.2}$$

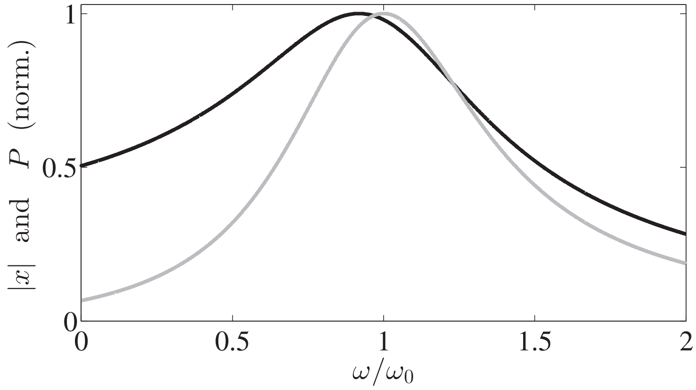

Figure 1.1: For an oscillator with eigenfrequency ω_0 and quality factor $Q = 2.5$, the black line corresponds to the magnitude of its displacement from equilibrium $|x|$, and the gray line corresponds to its dissipated power.

with q and p generalized position and momentum coordinates, we arrive to the equations of motion for the point charges:

$$\ddot{x}_a + \omega_0^2 x_a = \frac{e}{m} E(t, r_a). \tag{1.3}$$

The above equation describes a simple harmonic oscillator with frequency ω_0, driven by an electric force $F = eE(t, r_a)$. We will concern ourselves with time-harmonic driving fields, for which $E = E_0 e^{-i\omega t}$. Thus, we expect solutions of the form $x_a = Ce^{-i\omega t}$ with C a constant. We would also like to include in our analysis the influence of energy dissipation, which damps the motion of the charges. To first order, we can assume this process to exert a force that is linear with the velocity of the oscillating charge. The proportionality constant, γ, will be hereafter referred as the loss rate. With these assumptions, solving for x_a in equation 1.3 leads to the following result

$$x_a = \frac{\frac{e}{m} E(t, r_a)}{\omega^2 - \omega_0^2 - i\gamma\omega}. \tag{1.4}$$

The above expression is the origin of the well-known Lorentzian lineshape, which successfully describes the frequency-dependent response of practically all isolated resonators. For $\gamma \ll \omega_0$ the electron's displacement is maximized at the resonance condition $\omega = \omega_0$. In case γ is only "slightly" smaller than ω_0, e.g. resonators with quality factors $Q = \frac{\omega_0}{\gamma} \sim 2 - 10$, the resonance frequency is modified. Consequently, the frequency-dependence of the oscillator's amplitude and velocity can differ significantly. We illustrate this in Fig. 1.1(a), where we compare for a single oscillator the magnitude of its displacement from equilibrium, $|x|$, and its dissipated power given by $P = \frac{1}{2}\Re[F^* \dot{x}]$ with $\dot{x}$ its velocity. For the calculation, we choose $Q = 2.5$. It is clear that the maximum in $|x|$ is at a lower frequency than the maximum in P. The large damping of the oscillator magnifies this effect. We shall return to this point in Chapter 3, as it bears an interesting analogy with how metallic nanoparticles modify the electromagnetic spectrum in the far or near field.

1.3 Surface plasmons, light emission, and optical antennas

The optical response of deep sub-wavelength isolated metallic nanostructures resembles faithfully the Lorentz oscillator. Conduction electrons are driven primarily by the electric field of light, and their oscillatory motion is damped by Joule heating and the emission of radiation - radiative damping. The collective, damped, electronic oscillation results in the so-called localized surface plasmon resonance (LSPR).

We begin this section with a survey of seminal theoretical and experimental works that have highlighted the unique optical properties of metallic nanostructures. Where possible, connections to modified light emission will be emphasized. A full historical account of the field is beyond the scope of this thesis. We refer to S. Maier for further details on surface plasmon fundamentals and applications [4]. In this section, we illustrate interesting features present in coupled resonators, namely, Fano resonances. Lastly, we discuss the optical antenna functionality of metallic nanoparticles coupled to light emitters and receivers.

1.3.1 A brief history of surface plasmon related phenomena

Metallic nanoparticles in colloidal form have captivated artists and scientists for centuries. A beautiful example is present in the bright colors of stained glasses found in some churches. The colors of these glasses appear different in reflection than in transmission due to the presence of metallic nanoparticles. It was Gustav Mie who, in 1908, first explained the origin of this curious phenomenon rigorously [5]. Mie found that the light extinction (scattering + absorption) of a metallic colloid depends on the size of the nanoparticles due to the excitation of surface electromagnetic resonances, known today as LSPRs. Theoretical studies on the optical properties of metallic nanoparticles continued for decades, culminating in the classic book by Bohren and Huffman [6]. As discussed therein, it is not only the size, but also the geometry of metallic nanoparticles determining their optical response. While the scattering and absorption properties of LSPRs was well established by the work of Mie, Bohren, and Huffman, among others, the possibility to use these resonances for modified light emission was not realized until later.

An important development in physics, seemingly unrelated to the optics of metallic nanostructures, is due to Purcell in 1946. Purcell noted that the spontaneous emission rate, i.e. the time an excited state takes to relax via the emission of a photon, can be enhanced by coupling the emitter to a resonator [7]. The enhancement factor is proportional to the ratio Q/V, where Q is the quality factor of the resonator and V is the mode's volume. It appears that the first links between Purcell's work at radio frequencies and optical resonances in metals emerged in the 1980's. Gersten, Nitzan, and co-workers investigated fluorescence and Raman scattering of molecules adsorbed on rough metallic surfaces [8, 9]. They noted that light emission from molecules near nanoscale features in metals can be pronouncedly modified. Theoretical work also predicted that well-structured metallic particles with a nanometric gap in between could concentrate energy tremendously in the gap, which could in turn enhance the fluorescence of molecules therein [10][1]. However, the inherent randomness of the rough metallic films used in their experiments rendered experimental confirmation elusive. In particular, it was difficult to disentangle the contributions from geometrical resonances and the so-called lightning rod effect from their observations. The latter refers to the well-known fact from electrostatics that charges tend of accumulate near sharp features. Contemporaries to Gersten and Nitzan studied smooth metallic films, also for their ability to modify light emission. Since the pioneer work by Drexhage in 1970, it was established that even an unstructured mirror can modify the radiative decay rate of an emitter [11]. Barnes provides a comprehensive review of the underlying physics, which is based on a modification of the photonic mode density to which the emitter can decay [12].

The presence of additional decay channels for excited fluorophores in the vicinity of metals is related to the excitation of surface electromagnetic waves at the metal-dielectric interface. These are known as surface plasmon polaritons (SPPs), and they can be categorized as localized or propagating [4, 13]. Metallic films support optical resonances due to propagating SPPs. Since for a given energy the momentum of propagating SPPs is larger than that of a free-space photon, momentum-matching techniques (e.g. a grating or prism) are needed to excite SPPs with light [4]. In contrast, localized SPPs in metallic nanoparticles can be excited directly by free-space photons; the nanoscale curvature of the nanoparticle matches the momentum [4]. Both localized and propagating SPPs provide a resonant mechanism to which light emitters can couple, thereby establishing the link to the work of Purcell. Indeed, a number of pioneer studies showed that excited fluorophores in the vicinity of smooth metallic films can decay efficiently into propagating SPPs [14–17]. On the other hand, research on rough metallic films and metallic nanoparticles established that localized SPPs can accomplish a similar feat [8–10].

Until the 1990's, it seems that SPPs remained as an exciting, yet modest avenue of scientific research. An important experiment in 1998 by Ebbesen and co-workers was destined to change the latter condition, propelling metallic nanostructures to the forefront of scientific research. Ebbesen *et. al.* observed that, at particular wavelengths, the light intensity transmitted across a thin metallic film perforated with tiny holes largely exceeded the intensity that was geometrically incident on the holes [18]. The radius of the holes b was much smaller than the radiation wavelength λ at the extraordinary optical transmission (EOT) condition. Therefore, the effect appeared surprising in view of Bethe's theory for single holes[19], which predicted a cutoff with a transmission scaling as $(b/\lambda)^4$ for $\lambda \gg b$. The physics underlying the EOT effect has generated controversy regarding the role of localized surface plasmons in the holes, propagating surface plasmons through the film, and diffraction by the periodic arrangement of the holes. Details of the intricate physics at play are beyond the scope of this thesis, so we refer to the literature [20–24]. Here we wish to emphasize an important aspect of light-matter interactions that the phenomenon of EOT underlines: at resonance, the effective electromagnetic cross-section

---

[1] A small V boosts the Purcell factor up.

becomes much greater than the geometrical cross-section [6]. This principle applies on equal footing to resonant particles and holes. As a sub-wavelength hole array leads to an extraordinary optical transmission, a sub-wavelength particle array leads to an extraordinary optical extinction [25]. Babinet's principle guarantees the equivalence of these two cases in the limit of an infinitely thin perfect electric conductor which is either perforated by the subwavelength holes or is the material constituting the particles [26][2]. For realistic materials with a finite complex permittivity $\epsilon = \epsilon' - i\epsilon''$, deviations are expected.[3]. Still, a difference remains in that continuous metallic films support propagating SPPs, while isolated metallic particles do not.

The insights obtained from the EOT phenomenon led to important conceptual breakthroughs relevant to this thesis, so we elaborate on another key point. In 2003, Sarrazin *et. al.* [27] and Genet *et. al.* [28] independently noticed that the spectral lineshapes at the EOT condition have a characteristic asymmetry. These lineshapes resembled closely those discussed decades before by Ugo Fano, but in a different context [29]. Fano ascribed asymmetric resonance lineshapes observed in the autoionization spectrum of Helium to the quantum interference between a continuum of states and a discrete state whose energy lies within the continuum [29]. Although EOT involves classical interference (of field amplitudes) whereas Fano described quantum interference (of probabilities), the spectral signature of these effects are alike due to the universal character of wave interference. Thus, a correspondence between Fano resonances and EOT was established as follows: In sub-wavelength hole arrays, the transmission spectrum is modulated by the interplay between resonant and non-resonant transmitted light. The non-resonant transmitted light was ascribed the role of the continuum in Fano's theory, while the light resonantly diffracted in the plane of the hole array (Rayleigh anomalies, as discussed ahead in this chapter) was ascribed the role of the discrete state. Hence, a framework of plasmonic "Fano" resonances in sub-wavelength hole arrays emerged [30, 31]. By Babinet's principle, Fano-like lineshapes are expected in arrays of sub-wavelength metallic particles as well. In classical systems, Fano-like interference arises from the coupling between spectrally broad and narrow Lorentzian resonances, without invoking a continuum of states [32].

1.3.2 Surface plasmons as coupled oscillators and their Fano resonances

In Fig. 1.2 we present an illustrative calculation of Fano-like lineshapes in the spectrum of two coupled harmonic oscillators. In matrix form, the equations of motion for this

---

[2] A material with a dielectric function $\epsilon \to -\infty$ behaves as a perfect electric conductor.

[3] The application of Babinet's principle as formulated here requires that the incident polarization is switched from s to p when exchanging particles for holes and viceversa. A derivation of Babinet's principle for a perfect electric conductor makes use of the invariance of Maxwell's equations under the transformation $\mathbf{E} \to \mathbf{H}$ and $\mathbf{H} \to -\mathbf{E}$, and of the boundary conditions for a plane wave at the surface of such conductor. The boundary conditions are: (i) the tangential component of $\mathbf{E}$ and the normal component of $\mathbf{H}$ both vanish, (ii) the normal component of $\mathbf{E}$ is discontinuous by an amount proportional to the surface charge density, and (iii) the tangential component of $\mathbf{H}$ is discontinuous by an amount proportional to the surface electric current $\mathbf{J}$, and is directed normal to $\mathbf{J}$. [26]

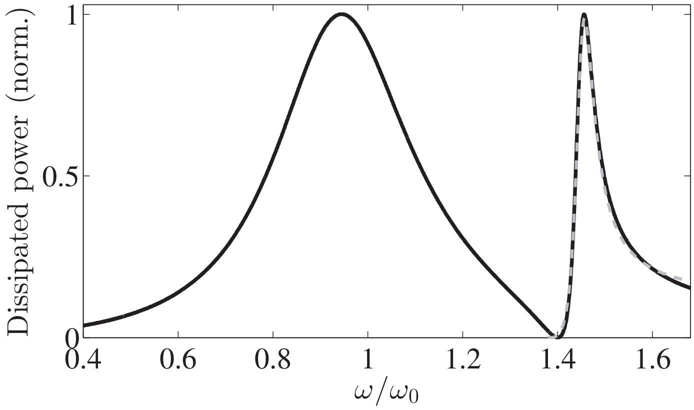

Figure 1.2: Dissipated power by oscillator 1, calculated with equation 1.5, as a black solid line. The gray dashed line is a fit of Fano's formula (Equation 1.6) to the black line. The parameters used in the calculation are given in the text.

system are

$$\begin{pmatrix} \omega_1^2 - \omega^2 - i\gamma_1\omega & \Omega^2 \\ \Omega^2 & \omega_2^2 - \omega^2 - i\gamma_2\omega \end{pmatrix} \begin{pmatrix} x_1 \\ x_2 \end{pmatrix} = \begin{pmatrix} \frac{F}{m} e^{-i\omega t} \\ 0 \end{pmatrix}, \tag{1.5}$$

where $\omega_{1,2}$ are the eigenfrequencies of the bare oscillators, $\gamma_{1,2}$ their respective loss rates, and Ω_{12} is the coupling rate. We plot the dissipated power by the first oscillator in steady-state, given by $\frac{1}{2}\Re[F^* \dot{x}_1]$. For the calculation, we choose $\omega_1 = \omega_0$, $\omega_2 = 1.4\omega_0$, $\gamma_1 = 0.4\omega_0$, $\gamma_2 = 0$, and $\Omega_{12} = 0.35\omega_0$. The amplitude of the driving force per units mass is irrelevant, because we are interested in qualitative behavior only and we therefore normalize the spectrum.

The broad peak near ω_0 is reminiscent of the single oscillator resonance, which may well represent a LSPR. The resonance peak is slightly shifted down in frequency from ω_0 due to the coupling with the second oscillator. The asymmetric resonance near $1.4\omega_0$ is due to the coupling with the second oscillator. Destructive and constructive interference between the 2 oscillators is responsible for the abrupt transition from suppressed to enhanced dissipation, which makes the lineshape asymmetric. We choose $\gamma_2 = 0$ to underline the fact that even for a bound state — one which doesn't couple to the environment and therefore doesn't dissipate — the coupling to the broad resonance (or the continuum in Fano's original framework) grants the lineshape a non-zero width. In other words, the width of the feature near ω_2 is limited by the value of the coupling constant Ω.

On top of the asymmetric feature in the dissipated power spectrum, we fit a lineshape of the form derived by Fano in his famous paper [29]; this is shown as a dashed gray line. The Fano formula for the scattering cross section is

$$\sigma = \frac{[q + 2(\omega - \omega_0)/\gamma]^2}{1 + [2(\omega - \omega_0)/\gamma]^2}, \tag{1.6}$$

where q is a phenomenological constant determining the degree of asymmetry in the lineshape. The other parameters have the same meaning as in the Lorentz oscillator. We shed light into Eq. 1.6 by considering three different values of q: i) For $|q| = \infty$, Eq. 1.6 yields a Lorentzian resonance lineshape, ii) For $q = 0$, Eq. 1.6 yields an upside-down Lorentzian lineshape, also known as an anti-resonance [31], iii) For $q \approx 1$, Eq. 1.6 yields the most asymmetric lineshapes, because in this regime the contributions from the discrete state and the continuum of states (or the narrow and broad resonance) are of comparable magnitude.

From the above discussion it follows that every resonance is a Fano resonance. The ubiquity of Fano resonances seems at odds with much of the excitement in recent years for their observation. Indeed, spectra such as the one observed in Fig. 1.2 will be recurrent throughout this thesis. The extinction spectrum of metallic nanoparticle arrays displays similar lineshapes due to the coupling of LSPRs to diffracted or guided modes. Interestingly, we will see that asymmetric Fano resonances can lead to unconventional effects in the emission spectrum of light sources coupled to metallic nanoparticle arrays. Such effects would be difficult — some perhaps impossible — to achieve with Lorentzian resonances ($|q| = \infty$ Fano resonances). This interesting contrast between extinction and emission of radiation in the spectral region near a Fano resonance is actually related to the difference between the dissipated power spectrum and the displacement spectrum of coupled oscillators. In the forthcoming Chapters, we will explore this effect in depth.

1.3.3 Optical antennas

By the dawn of the 21st century, numerous studies on SPPs had made it clear that the large polarizability of metals combined with the small dimensions of nanostructures (in reference to the free-space driving field) embodies an efficient interface between free-space radiation and localized energy. Therefore, the term optical antenna, or nanoantenna, emerged to describe metallic nanostructures with LSPRs coupled to light sources or receivers [33–39].[4] In contrast to low-frequency antennas in the electrostatic limit, the electric field inside optical antennas is not zero due to the excitation of SPPs [6]. The deviation from electrostatics is an important one, because it disables a simple scaling of the antenna dimensions from the low-frequency regime to the optical regime. Here we recall that Maxwell's equations are frequency-invariant. However, the frequency-dependence of the dielectric function leads to different antenna behavior throughout the spectrum even if the relative dimensions of the antenna and operating wavelength are fixed. In general, electrodynamic effects become increasingly relevant as one approaches the plasma frequency of the material constituting the antenna. In this intriguing spectral region — where the balance between field penetration into the metal and energy dissipation can be tailored — plasmon antennas thrive. We note that for a restricted class of structures, Novotny found that metallic nanoantennas can be characterized by an effective wavelength [41]. However, a general formula for the effective wavelength of arbitrary nanoantennas is not

---

[4] Perhaps the earliest vision — but not conception! — of an optical antenna dates to the famous 1959 lecture "There's Plenty of Room at the Bottom" by R. P. Feynman, who said: "Is it possible, for example, to emit light from a whole set of antennas, like we emit radio waves from an organized set of antennas to beam the radio programs to Europe? The same thing would be to beam the light out in a definite direction with very high intensity." [40].

known yet.

The optical features of LSPR-based nanoantennas have been demonstrated in several recent papers. When coupled to nanoscale light sources, metallic nanostructures can provide directivity gain [42–45], polarization control [46, 47], intensity enhancements [36, 37], decay rate enhancements [48, 49], and spectral shaping [50, 51]. In the following chapters, we will explore how some of these properties, and others, can be further designed by coupling LSPRs to long-range photonic modes in periodic arrays of metallic nanoantennas. The emergent hybrid plasmonic-photonic resonances inherit the strong interaction with light characteristic of plasmonic modes, and the spatially extended modal volumes characteristic of photonic modes. By tailoring the balance between these two, a large number of possibilities open up to modify light emission from extended sources. But first, we turn our attention to another concept which is of paramount relevance to this thesis: wave propagation in periodic media.

1.4 Rayleigh anomalies and Bloch waves

The year 1902 brought a ground-breaking experimental discovery to the history of physics. Wood reported on a remarkable set of bright and dark bands appearing in the reflection spectrum of a diffraction grating [52]. The nature of these bands was unaccounted for by the existing theory, so they became known as “Wood’s anomalies”. It was Lord Rayleigh who, a few years later, postulated that this peculiar distribution of light could be related to the condition whereby a diffraction order radiates grazing to the surface of the grating [53]. Rayleigh formulated the problem based on the existing laws of reflection and refraction, appealing only to wave mechanics and geometrical considerations. He derived relations between the incident and scattered wave vectors in a grating, thereby establishing the foundations of diffraction theory [54]. In its modern form, Rayleigh’s condition is casted as a momentum conservation law, because the wave vector $\mathbf{k}$ is related to the photon’s momentum via the de Broglie relation $\mathbf{p} = \hbar\mathbf{k}$. For propagation in a lattice with reciprocal vector $\mathbf{G} = \frac{2\pi}{a}\mathbf{u}$, where a is the lattice constant and $\mathbf{u}$ is a unit vector along the periodicity axis, the Rayleigh condition states that

$$\mathbf{k}_{\parallel}^{\mathbf{out}} = \mathbf{k}_{\parallel}^{\mathbf{in}} + \mathbf{G}. \tag{1.7}$$

$\mathbf{k}_{\parallel}^{\mathbf{in}}$ and $\mathbf{k}_{\parallel}^{\mathbf{out}}$ are the projections of the incident and diffracted wave vectors parallel to the array, respectively. In his derivation, Rayleigh made no assumptions on the composition of the material constituting the grating (e.g. metal or dielectric). Therefore, Rayleigh’s theory has served to describe light propagation in diverse periodic media, and constitutes a pillar of modern optics. For this reason, we shall hereafter refer to the solution of equation 1.7 as the “Rayleigh anomaly”.

The influence of a metal back coating present in the gratings studied by Wood was largely overlooked by Rayleigh. Wood speculated that resonant effects could have an influence on his observations, as he observed that the position of the bands shift when the refractive index of the medium surrounding the grating increased.[5] Wood's observations and Rayleigh's description bear the seeds of the exciting interplay between optical resonances in metals (SPPs) and wave propagation in periodic media. In forthcoming chapters we will explore this interplay in depth. For now, we turn our attention to another important development in the field of wave propagation in periodic media.

Amongst the most notable contributions to our understanding of wave mechanics in periodic media stands the work of Felix Bloch and Gaston Floquet. Bloch was interested in the conduction of electrons in crystalline solids [55]. His work played a central role in the establishment of quantum mechanics as a successful theory. Unknowingly, he had extended the formalism developed by mathematician Floquet [56]. The essence of the Bloch-Floquet theory states that the amplitude of waves in periodic media acquires the form

$$\psi(\mathbf{r}) = e^{i\mathbf{k}\cdot\mathbf{r}}u(\mathbf{r}) \tag{1.8}$$

where r is the position, u($\mathbf{r}$) is a periodic function in this case representing the potential landscape in which the wave propagates, and $\mathbf{k}$ is the wave vector. For historical reasons, solutions to equation 1.8 are known as Bloch waves, so we shall adhere to that terminology in what follows.

Bloch waves conform to the grating's potential V, for which $V(x) = V(x+a)$. They result from multiplying a plane wave with a periodic function. Comparing 1.7 and 1.8 it is easy to see that a Rayleigh anomaly corresponds to a Bloch wave. The lattice gives a spatially periodic function of the form $e^{i\mathbf{G}\cdot\mathbf{r}}$, which when multiplied with the incident plane wave $e^{i\mathbf{k}^{\mathbf{in}}\cdot\mathbf{r}}$, yields a Bloch wave of the form $e^{i\mathbf{k}^{\mathbf{out}}\cdot\mathbf{r}}$. The dot product with the vector $\mathbf{r}$ picks the parallel component out of the incident and output wave vectors.

1.5 Dielectric waveguide modes

We have so far considered two mechanisms by which optical waves can be tamed: i) nanoantennas with surface plasmon resonances can transform plane waves into localized energy and viceversa, and ii) diffraction gratings can transform plane waves into Bloch waves and viceversa. The first mechanism allows energy to be confined on a deep sub-wavelength scale, but not necessarily to be guided. The second mechanism allows energy to be guided, but does not necessarily provide deep sub-wavelength confinement. In order to achieve full control of electromagnetic waves and couple them efficiently to matter, we are in need of a mechanism that allows simultaneous light confinement and guiding. The simplest and best known structure fulfilling this requirement is a dielectric slab waveguide.

Dielectric slab waveguides support propagating modes that are bound to a high refractive-index layer. The confinement and propagation constant of these waves can be tailored via the refractive index contrast between the high- and the low-index media,

---

[5] The insights provided by Wood in his 1902 paper are enlightening: 'the shift [of the bright and dark bands] is in the same direction as when a resonator is immersed in a medium of high dielectric constant, and though there may be no connexion between the two phenomena, it seems perhaps worth while to mention it as there may be something akin to resonance in the action of this grating [52]."

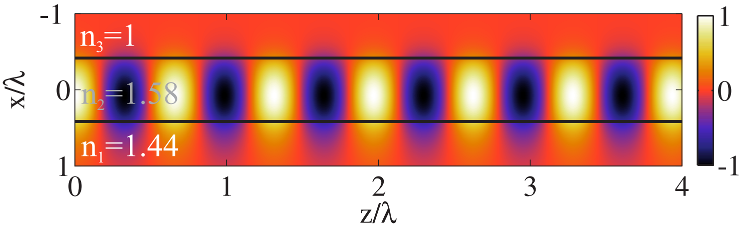

Figure 1.3: Analytical calculation of the electric field distribution for the fundamental TE guided mode in a dielectric slab waveguide.

and the waveguide thickness. The theory of optical waveguides is extensive and well documented in the literature (e.g. Ref. [57]), so we will not reproduce that here. Instead, we provide a motivation for their use in combination with metallic nanoparticle arrays. In this spirit, we present in Fig. 1.3 an illustrative calculation of the fundamental transverse electric (TE) guided mode in a dielectric slab of refractive index $n_2 = 1.58$ covered by semi-infinite media with $n_1 = 1$ above and $n_3 = 1.44$ below. These refractive indices correspond to polystyrene, air, and glass, respectively, all in the visible spectrum, where these materials are only weakly dispersive. The thickness of the middle layer is 0.83 λ, where λ is the free space wavelength. The choice for these refractive indices and thickness will become clear in Chapter 3, where metallic nanoparticle arrays will be embedded in similar waveguides. The mode profile in Fig. 1.3 was analytically calculated using the formalism described by Yariv and Yeh [57]. The horizontal black lines in Fig. 1.3 delimit the high-index layer, where the guided mode propagates. The axes are scaled with respect to the free-space wavelength λ, while the electric field amplitude beats along z at the effective wavelength in the slab. Along x, the amplitude is greatest close to, but not exactly at, the center of the waveguide. The higher refractive index of the substrate with respect to the superstrate induces an asymmetry in the mode profile. This manifests as an enhanced mode amplitude towards the substrate. The index difference also introduces a cut-off for the fundamental mode. This means that there exists a lower limit for the thickness of the high-index layer in order for the fundamental mode to be supported.

Besides the spatial properties of guided modes, we are interested in their dispersion relation, i.e. the relationship between energy and momentum. From Maxwell's equations it follows that in order for bound modes to exist in the dielectric slab, their dispersion relation must lie within the light cone of the high-index layer and outside the light cone of the low-index surrounding media [57]. In a linear time-invariant system such modes can not be excited by free-space light. A momentum-matching technique, such as a prism or grating, is needed for coupling to them. We will focus on the excitation of guided modes with the assistance of a grating, as these will be recurrent throughout this thesis. Of particular interest is the fact that the periodicity of a grating in real space yields an infinite number of Bloch harmonics in momentum-space. Thus, a grating-coupled guided mode can lie outside the light cone of the $m = \pm 1$ diffraction orders radiating in the low-index surrounding medium, but inside the light cone of the $m = 0$ order in the same medium. This means that such mode can be excited by an incident plane wave scattered by the

$m = \pm 1$ orders.

We shed light on the above description by plotting the dispersion relation of the fundamental TE guided mode in the structure of Fig. 1.3, with the additional condition that the dispersion relation is $2\pi/a$ periodic in k-space. The periodicity of the dispersion relation in k-space arises naturally from Bloch's theorem when the guided mode propagates in a periodic medium with lattice constant a. Figure 1.4(a) shows such a calculation, with the same refractive index set and waveguide dimension shown in Fig. 1.3. The two dashed blue lines correspond to counter-propagating guided waves, as it may be deduced from the opposite sign of their group velocity given by $v_g = \partial\omega/\partial k_\parallel$. The radiative zones of the ± 1 diffraction orders are delimited by the solid magenta lines for a refractive index of $n_1 = 1.44$, and by the green lines for $n_2 = 1.58$. These lines are solutions to the Rayleigh anomaly equation with a lattice constant $a = 370$ nm. The gray shaded area is the spectral region where guide modes exist. Notice that at low energies the fundamental guided mode approaches the light line in the $n_1 = 1.44$ medium; here the mode is only weakly confined, with a significant fraction of its energy embedded in the surrounding media. In contrast, at higher energies the same mode approaches the light line in the $n_2 = 1.58$ medium; here the mode is more strongly confined, with a significant fraction of its energy embedded in the high-index layer. Most importantly, these guided modes can now be excited by incident plane waves with arbitrarily small $k_\parallel$, so long as their energy is matched by the incident plane wave.

From Figs. 1.3 and 1.4 it is clear that a simple dielectric slab waveguide provides an efficient mechanism to guide optical energy, with a velocity and confinement determined by the refractive index contrast and waveguide thickness. It is easy to envisage that interesting dynamics may arise from the coupling of optical antennas and waveguides tuned in-resonance with each other. Such coupling can be achieved by placing metallic nanoparticles in close vicinity to the waveguide, or inside the waveguide. If the coupling rate becomes stronger than the loss rates of the modes, a hybrid light-matter quasi-particle known as a waveguide-plasmon polariton is formed [58, 59]. Several features of strongly coupled systems are of universal character, so we finalize this introductory chapter by illustrating these. As an example, we consider the coupling between the fundamental guided mode in Fig. 1.4(a) and a localized mode for which its energy is independent of $k_\parallel$. Such coupled system can be modeled by a simple two-state Hamiltonian,

$$H = \begin{pmatrix} E_1 & \Omega \\ \Omega^* & E_2(k_\parallel) \end{pmatrix}, \tag{1.9}$$

where, in our configuration, E_1 and E_2 $(k_\parallel)$ are the energies of localized and guided states, respectively, while Ω is their coupling rate. Diagonalizing H yields its eigenenergies, which can be expressed in the form,

$$E_\pm = \frac{E_1 + E_2}{2} \pm \frac{\Delta}{2}\sqrt{1 + \left(\frac{2\Omega}{\Delta}\right)^2}, \tag{1.10}$$

where we have defined $\Delta = E_1 - E_2$ as the energy detuning of the bare states. The influence of coupling and detuning on the mixed states $E_\pm$ can be elucidated by Taylor expanding

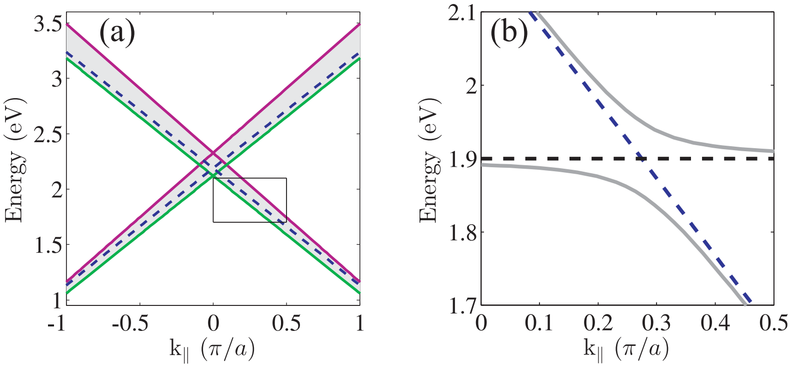

Figure 1.4: (a) The dashed blue line is the dispersion relation of the fundamental TE guide mode in the slab waveguide of Fig. 1.3. The solid magenta and green lines are Rayleigh anomalies for a lattice constant a and a refractive index of $n = 1.44$ and $n = 1.58$, respectively. The shaded gray area is the region where guided modes exist. The dispersion relation of the guided mode has been shifted by $\pm\,\pi/a$ using Bloch's theorem, as explained in the text, but no periodic structure has been used for the calculation. The black rectangle indicates the spectral region considered in (b). (b) the dashed blue line are the same as in (a), the dashed black line is E_1 in the Hamiltonian of equation 1.9, and the gray lines are the eigenenergies of the Hamiltonian, $E_{\pm}$, as given in equation 1.10. This shows how the dispersion relation of the guided mode in (a) would be modified in the presence of coupling to an additional state with energy E_1.

equation 1.10 at different values of $\frac{2\Omega}{\Delta}$. Expanding at $\frac{2\Omega}{\Delta} = 0$ (or $\Delta \to \infty$, i.e. very large detuning) we get,

$$E_{\pm} \approx \tilde{E} \pm \frac{\Delta}{2}\left(1 + \left(\frac{2\Omega}{\Delta}\right)^2 + \left(\frac{2\Omega}{\Delta}\right)^4 \dots\right), \tag{1.11}$$

where we have defined $\tilde{E} = (E_1 + E_2)/2$ as the average energy. In contrast, expanding equation 1.10 at $\frac{2\Omega}{\Delta} = \infty$ (or $\Delta \to 0$, i.e. zero detuning) we get,

$$E_{\pm} \approx \tilde{E} \pm \frac{\Delta}{2}\left(\frac{2\Omega}{\Delta} + \frac{1}{2}\frac{\Delta}{2\Omega} - \frac{1}{8}\left(\frac{\Delta}{2\Omega}\right)^3 \dots\right). \tag{1.12}$$

Retaining only the leading terms of the expansions in equations 1.11 and 1.12, one sees that: i) for large detuning $E_{\pm} = \tilde{E} \pm \Delta/2$, which are identically the energies of the bare states, and ii) for zero detuning $E_{\pm} = \tilde{E} \pm \Omega$, implying an energy splitting of 2Ω for the hybrid states. If we now consider the transition from large negative detuning to large positive detuning, it follows that the hybrid states exchange their resemblance to one or the other of the bare states at zero detuning. At exactly zero detuning, the degeneracy of the bare states is lifted and the hybrid states lie as a linear superposition of the bare states with equal weights.

The above discussion is illustrated in Figure 1.4(b), where we plot $E_{\pm}$ using typical energies of optical waveguide-plasmon coupled systems. For the calculation, we set $E_1 = 1.9$ eV, E_2 equal to the $k_{\parallel}$-dependent energy of the fundamental guided mode as shown in in Fig. 1.4(a), and $2\Omega = 0.1$ eV. The plot in Fig. 1.4(b) focuses on the spectral region enclosed by the black rectangle in Fig. 1.4(a), which is where the energies of the bare (mixed) states cross (anti-cross). The dashed blue line is the fundamental guided mode from Fig. 1.4(a), the dashed black line is the aforementioned localized mode, and the gray lines are the upper and lower hybridized states,$E_{\pm}$, in this case waveguide-plasmon polaritons. Similar physics is expected to arise from the coupling of different propagating states to localized states, such as the coupling of Rayleigh anomalies to localized surface plasmons.

As we will show in forthcoming chapters, hybrid light-matter systems represent an interesting route for controlling light extinction and emission from nanoscale sources. Coupling effects can manifest differently in the far-field than in the near-field, enabling unprecedented optical functionalities.

1.6 Outline of this thesis

In this thesis we investigate the coupling of light and matter in metallic nanoparticle arrays. We explore the interplay between distinct optical modes, including localized surface plasmons, Rayleigh anomalies, dielectric waveguide modes, and light-emitters. Metallic nanostructures have been designed to exhibit resonant effects in the visible or near infrared spectrum. Luminescent materials were selected on the basis of their optical and chemical properties. These light emitters were placed in the vicinity[6] of metallic nanostructures to enhance their mutual coupling. Each chapter is devoted to a particular coupling scheme. While self-contained, each chapter builds on the knowledge developed in previous chapters, thereby deepening our incursion into the richness and complexity of light-matter interactions at the nanoscale. This thesis is organized as follows:

In Chapter 2 we consider the coupling of localized surface plasmons to diffracted orders. This coupling leads to hybrid plasmonic-photonic collective resonances, known as surface lattice resonances (SLRs). We will first investigate the origin and properties SLRs in metallic nanoparticle arrays embedded in fully homogeneous dielectric medium. Next, we will present experimental results for similar arrays but covered by a thin luminescent layer. In particular, we will demonstrate how surface lattice resonances can enhance the directionality and polarization of the emitted light.

In Chapter 3 we consider the coupling of localized surface plasmons to guided modes in dielectric layers. Firstly, we present experiments with a silver nanoparticle array standing on a light-emitting slab waveguide. We provide evidence for an unconventional light emission enhancement at frequencies and wave vectors for which the array is nearly transparent. Secondly, we investigate a complementary system composed of an aluminum nanoparticle array *in* (rather than *on*) a light-emitting waveguide. By varying the waveguide thickness we demonstrate a transition from weak to strong coupling between localized surface plasmons in the nanoantennas and refractive index guided modes in the waveguide. We elucidate the physics of these two systems through models of coupled harmonic oscillators and numerical simulations. The latter explain the unconventional

---

[6] Here, by “vicnity” we refer to a geometrical distance being smaller than the characteristic scales of the optical mode. This can be a few tens of nanometers, or hundreds of nanometers, depending on the spatial decay of the electromagnetic field.

light emission enhancement at the conditions of induced transparency in terms of the local electromagnetic field enhancements in the structure.

In Chapter 4 we build on our knowledge of SLRs in order to access the strong coupling regime with excited electronic states (excitons) in organic molecules. By covering a silver nanorod array with a thin layer of polymer and organic molecules at a high concentration, we observe a hybridization between molecular excitons and SLRs. This hybridization results in a quasi-particle called plasmon-exciton-polariton, which displays an exceptionally light effective mass which is furthermore tunable via the periodicity of the array. As we show therein, PEPs can thermalize, and their effective temperature cool upon increased optical pumping. These properties are relevant for the realization of a quantum condensed state of light and matter in a plasmonic system - a yet unreported phenomenon.

Chapter 5 deals once more with the coupling between localized surface plasmons and diffracted orders in the presence of luminescent molecules, but with an additional complexity. In contrast to most plasmonic structures displaying a dominant electric dipolar response, the structures here investigated display an enhanced magnetoelectric and quadrupolar response. This unconventional response is created by tapering the nanoparticles out of the plane of the periodicity, thereby creating metallic pyramids rather than pillars or rods. Enhanced magnetoelectric and quadrupolar response hold the key to tailor the ratio of forward to backward scattering in anomalous ways, as predicted decades ago by Kerker and co-workers [60]. Here we demonstrate anomalous forward to backward light emission from molecules weakly coupled to an aluminum nanopyramid array. This effect holds great promise for applications to solid-state lighting, where unidirectional light emission is desired.

In Chapter 6 we take a step forward towards actively controlling the resonant light emission enhancements provided by metallic nanoparticle arrays. For this purpose, we cover an array of metallic nanoparticles standing on a light-emitting waveguide with a thermotropic liquid crystal (LC). The LC undergoes a phase transition as a function of temperature. In the low-temperature phase the LC is birefringent (the speed of light depends on the propagation direction), whereas in the high-temperature phase it is isotropic. Therefore, the resonance conditions of the array can be controlled by varying the temperature of the sample. In this way, we demonstrate active control of light emission enhancements from a metallic nanoparticle array with an unprecedented spectral and angular selectivity.

CHAPTER 2

LOCALIZED SURFACE PLASMONS COUPLED TO DIFFRACTED ORDERS

Metallic nanoparticle arrays display hybrid plasmonic-photonic optical resonances known as surface lattice resonances (SLRs). SLRs emerge from the radiative coupling between Localized Surface Plasmon Resonances (LSPRs) and waves diffracted in the plane of the array [Rayleigh Anomalies (RAs)]. Here we investigate the tunable optical properties of SLRs in a given lattice by varying the dimensions of the nanoparticles. This variation changes the energy detuning of the bare LSPR and RA states, and in turn modifies their relative contributions to the plasmonic-photonic admixture. We show that the dispersion, linewidth, and field confinement of SLRs with different modal symmetries can be pronouncedly modified by geometrical design. We demonstrate the potential of SLRs to enhance the light emission directionality and polarization of a nanometric layer covering a metallic nanoparticle array. The advantages of SLRs with respect to LSPRs for enhanced light emission are discussed, and further applications beyond those presented here are envisioned.

2.1 Introduction

The excitation of surface electromagnetic modes grants metallic nanostructures a rich optical response that is tunable by geometrical design. If the electromagnetic fields of distinct optical modes overlap spatially, the modes couple with a strength proportional to the field overlap. Coupled surface modes have been observed in metallic gratings [61–63], arrays of subwavelength holes [20, 64–66], slits [67, 68], voids [69], split rings [70], and stacked nanowire arrays [71]. Recently, periodic arrays of metallic nanoparticles have attracted increasing interest for their ability to support hybrid plasmonic-photonic modes arising from the radiative coupling between Localized Surface Plasmon Resonances (LSPRs) and waves diffracted in the plane of the array [Rayleigh Anomalies (RAs)]. These hybrid modes were first studied by Carron and co-workers [72]. Schatz and co-workers later revived interest in this phenomenon through a series of theoretical papers predicting extremely narrow resonance linewidths (~ 1 meV) [73, 74]. Experimental observation of such sharp resonances remained elusive for several years [75], largely because fabrication and characterization methods did not reproduce faithfully the theoretical conditions. Recent progress in these directions has enabled the observation of sharp optical resonances in the spectrum of metallic nanoparticle arrays, known as surface lattice resonances (SLRs) [23, 25, 76–84]. While hybrid plasmonic-photonic modes also exist in different metallic structures (e.g. arrays of holes, slits, voids, etc.), we will show that SLRs stand at the pinnacle of low-loss tunable plasmonic resonances.

SLRs are collective resonances, i.e., their quality factors Q increase with the number of particles in the array [85][1]. Their dispersion and linewidth are tunable by geometrical design of the particle and lattice [82, 83], which determines the energy detuning between the coupled LSPR and RA states [80]. In contrast to perforated continuous metallic films where LSPRs couple through lossy metals, LSPRs in metallic nanoparticles couple through loss-less dielectrics. For these reasons, metallic nanoparticle arrays are a great system for enhancing spontaneous emission [86–90], lasing [91], and refractive index sensing [92, 93]. In this chapter, we investigate the properties of SLRs in periodic arrays of metallic nanorods with different dimensions. First we present results for arrays embedded in a fully homogeneous and isotropic dielectric medium. The uniform surrounding dielectric aids in bringing out sharp SLRs, and to exclude the influence of dielectric interfaces on their properties [94]. After discussing the tunable properties of SLRs in depth, we demonstrate their potential for modifying the emission spectrum, directionality, and polarization, from a thin luminescent layer covering a metallic nanoparticle array.

---

[1] As explained in Ref [85], the SLR Q-factor increases as long as the size of the array is smaller than the propagation length L_x of the surface mode. For arrays larger than L_x, the spatial decay of surface waves limits the long-range coupling of the particles. For the sharpest SLRs here investigated, L_x can be up to several tens of microns depending on the value of $k_{\|}$.

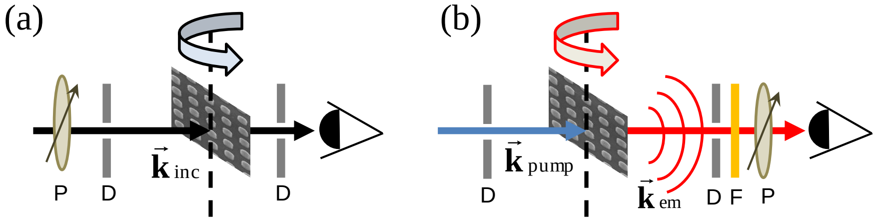

Figure 2.1: Setups used for (a) extinction, and (b) photoluminescence enhancement measurements throughout this thesis. The sample is represented by a scanning electron micrograph of a metallic nanoparticle array. D, F, and P, stand for diaphragm, (spectral) filter, and polarizer, respectively. The vertical dashed lines indicate the axis of rotation for the sample in (a) and detector in (b). The incident polarization and k-vector are specified for each measurement in the text.

2.2 Surface Lattice Resonances in homogeneous media

2.2.1 Extinction experiments

Periodic arrays of gold nanorods were fabricated onto a fused silica substrate by electron beam lithography. The total size of each array is 1.5×1.5 mm^2, and the lattice constants are $a_x = 600$ nm and $a_y = 300$ nm. All nanorods have an approximately rectangular shape in the plane of the array, with a length of 450 ± 20 nm, and a height of 40 ± 2 nm. The width of the nanorods, w, was varied by varying the e-beam exposure. The rectangular shape of the gold nanorods allows to independently tune the LSPRs associated with light polarized along the short or long axis of the nanorods. In this case, we probe the array with light polarized parallel to the short axis of the nanorods, i.e., along a_y. We present results for 5 samples with w =70 nm, 110 nm, 160 nm, 200 nm, and 230 nm. All arrays were embedded in a uniform surrounding medium by covering them with a silica superstrate preceded by n = 1.45 refractive index matching liquid to ensure good optical contact. A scanning electron micrograph of the w = 110 nm array is shown as an inset in Fig. 2.2(b), along with the cartesian coordinates used throughout this chapter. Other arrays display similar structural quality.

Figure 2.1(a) shows a schematic representation of the setup used to measure the variable angle extinction of the array. We measured the transmission of a collimated (angular spread $< 0.1°$) beam from a halogen lamp linearly polarized along the short axis of the nanorods. A computer-controlled stage rotates the sample about the y-axis by an angle θ_{in}, thereby changing the in-plane component of the wave vector $k_\parallel = k_0 \sin(\theta_{in})$ along the long axis of the nanorods. k_0 is the magnitude of the free space wave vector. The angular resolution of the measurements is 0.5°. A fiber-coupled spectrometer in the far-field measures the zeroth order transmittance T_0, from which the extinction follows as $1 - T_0$. The numerical aperture of the detecting system is NA $= 4 \times 10^{-3}$, ensuring negligible angular averaging in collection.

Figure 2.2 displays the extinction of the 5 arrays discussed above, in color as a function of the incident photon energy and $k_\parallel$. The (+1,0) and (-1,0) RAs are plotted as solid and

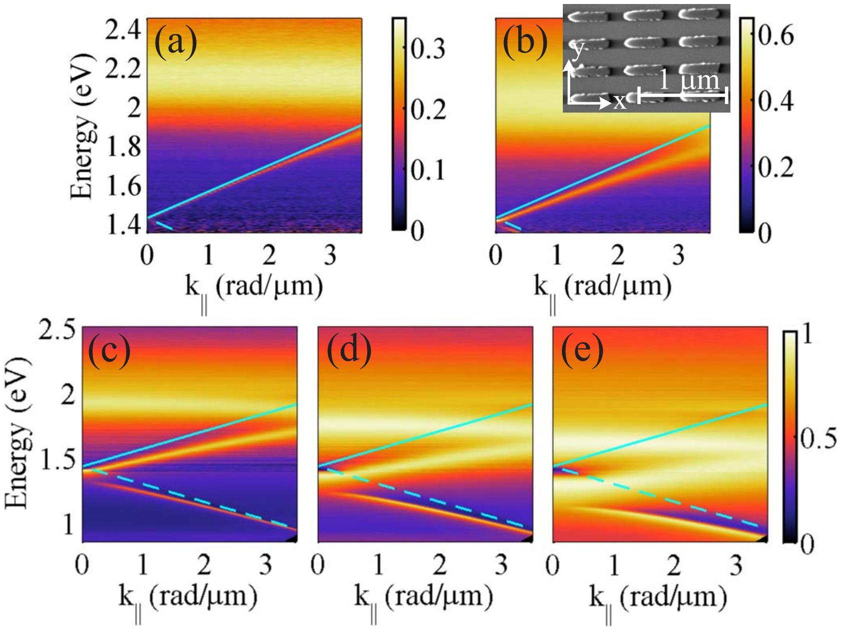

Figure 2.2: Experimentally measured extinction for arrays of gold nanorods with width w given by (a) $w = 70$ nm, (b) $w = 110$ nm, (c) $w = 160$ nm, (d) $w = 200$ nm, and (e) $w = 230$ nm. The solid and dashed lines correspond to the (+1,0) and (-1,0) Rayleigh anomalies, respectively. The inset in (b) shows a scanning electron micrograph of the $w = 110$ nm array.

dashed lines, respectively. These RAs are calculated using Eq. 1.7 for a refractive index $n = 1.45$. The two measurements in Figs. 2.2(a,b) are plotted in the same energy range (corresponding to wavelengths between 506 nm and 918 nm), covered by standard silicon detectors. The three measurements in Figs. 2.2(c,d,e) are plotted in the same energy range (corresponding to wavelengths between 496 nm and 1459 nm), which is more extended than the one in Figs. 2.2(a,b). For this extended spectral range, a combination of Si and InGaAs detectors was used. The momentum range for all plots is 3.5 rad/μm, which corresponds to 16.2 degrees at 500 nm, 30.8 degrees at 918 nm, and 54.4 degrees at 1459 nm.

The broad, dispersionless resonance on the high-energy side of all spectra is reminiscent of the single particle LSPR. The narrow, dispersive resonances on the low-energy side of the RAs are the so-called SLRs. In the array, LSPRs couple to the (±1,0) RAs, so the three resonance bands (one for each bare mode) correspond to hybridized modes with tunable plasmonic-photonic content. In addition, the upper and lower SLRs mutually couple. This leads to an energy gap near $k_\parallel = 0$. The mutual SLR coupling manifests in the SLR anti-crossing near the energies where the RAs cross (1.4 eV for this lattice). At the anti-crossing, the upper SLR is excited strongly by the incident plane wave while the extinction of the lower SLR vanishes. As shown ahead, this is due to the even and odd parity of the upper and lower SLRs, respectively. Hence, we call the symmetric SLR “bright” and the

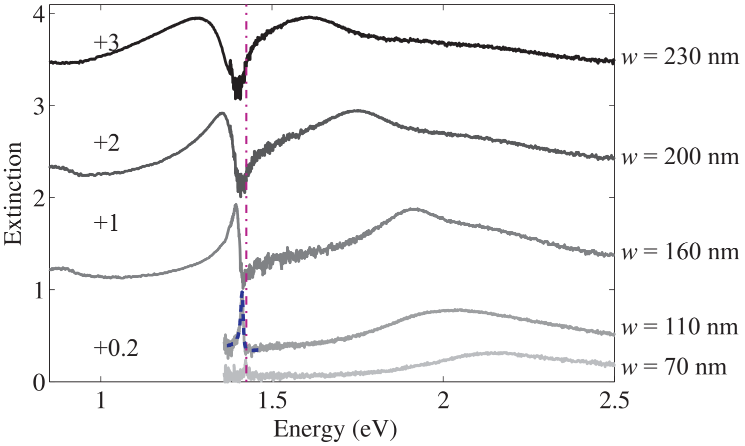

Figure 2.3: Experimental extinction spectra at $k_\parallel = 0$ for arrays with increasing nanorod width (light gray to black lines) as indicated on the right. The spectra have been shifted for clarity by the amount indicated on the left. The dash-dotted line is the Rayleigh anomaly condition at $k_\parallel = 0$, while the dashed line is a Fano fit to the SLR for the $w = 110$ nm array.

anti-symmetric SLR "dark", alluding to their respective excitation strengths by a normal incident plane wave. Further details on the opening of the gap are discussed ahead, in view of numerical simulations.

The hybridization between the 3 coupled modes depends on multiple parameters. Here we focus on two independent ones, namely the nanorod width w and in-plane incident wave vector $k_\parallel$. As w increases, the LSPR is shifted down in energy and spectrally broadened - the expected behavior for single particle resonances due to increased depolarization and radiative damping [4]. Thus, by varying w we probe different LSPR-RA detunings. Furthermore, since RAs are dispersive while LSPRs are not, varying $k_\parallel$ modifies the LSPR-RA detuning for a given array. The measurements in Fig. 2.2(a)-(e) show that the LSPR-RA detuning exerts an important influence on the SLR properties. As w increases the SLRs shift down in energy, their linewidths broaden, their group velocity $v_g = \partial\omega/\partial k_\parallel$ decreases, and the gap between upper and lower SLRs widens. Besides, the $k_\parallel$-dependent LSPR-RA detuning also modifies the SLR characteristics for each array. As $k_\parallel$ increases the detuning between the LSPR and (+1,0) RA decreases. Consequently, the upper SLR peak energy deviates more from the (+1,0) RA, its linewidth broadens, and its group velocity lowers as it approaches the LSPR for which $v_g = 0$. In contrast, as $k_\parallel$ increases the detuning between the LSPR and (-1,0) RA increases. Consequently, the lower SLR becomes more photonic-like at lower energies due to the diminished contribution from the LSPR in the plasmonic-photonic admixture. This grants the lower SLR a narrow linewidth and a peak energy close to the (-1,0) RA at high $k_\parallel$. Let us illustrate the foregoing discussion regarding the influence of the LSPR-RA detuning on the spectral lineshapes, taking as example the spectra at normal incidence ($k_\parallel = 0$).

Figure 2.3 shows the 5 spectra from Fig. 2.2 at $k_\parallel = 0$. For $w = 70$ nm, the LSPR-

RA detuning is high. The low extinction cross section of the nanorods leads to a weak feature near the SLR condition. Increasing to $w = 110$ nm decreases slightly the LSPR-RA detuning, but this has an important influence on the SLR excitation strength at 1.43 eV. This observation is in agreement with calculations by Schatz an co-workers, who predicted that an optimum LSPR-RA detuning exists for sharpening SLRs [73, 74]. As w increases further, the LSPR and RA hybridize more strongly, leading to broader SLR linewidths. For $w = 230$ nm the linewidths of the LSPR and SLR become approximately equal because the LSPR-RA detuning is close to zero. Here the hybrid states are a linear superposition of the bare states with roughly equal weights. Notice also that the detuning between the low-energy resonance (identified as SLR for small w), and the RA indicated by the dash-dotted line, increases with w. This suggests that the LSPR-RA coupling strength increases. As we have seen in Chapter 1, for increasing coupling strength the mixed states detune increasingly more from the bare states.

Let us now focus on a minor spectral feature which has a deep significance for the field of plasmonics. Notice that a dip in extinction arises near — but not always exactly at — the RA condition. The position of the dip appears to red-shift as w increases. For arrays with $w = 110$ nm and $w = 160$ nm, the dip is at the RA condition within the noise of the measurements. In contrast, for arrays with $w = 200$ nm and $w = 230$ nm, the dip is red-shifted. For the $w = 70$ nm array it is hard to tell, but it appears that the SLR peak overlaps with the RA condition. This curious effect is partly responsible for much controversy on the interpretation of the extraordinary optical transmission (EOT) phenomenon for hole arrays discussed in Chapter 1. Some authors attributed the EOT phenomenon to SPPs [20, 28], and others to Rayleigh anomalies [23, 27]. The varying position of the dip in extinction for particle arrays (peak in extinction for hole arrays) made it difficult to disentangle these effects. In this sense, the measurements of Figs. 2.2 and Fig. 2.3 clarify that both LSPRs and RAs are relevant to the phenomenon. Their relative contributions depend on the detuning of the bare modes in a given structure. Furthermore, the deviation of the extinction dip from the RA condition seems to be proportional to both LSPR and SLR linewidths. Here we recall that Rayleigh's condition [equation 1.7] states the conservation of the parallel component of a *real* wave-vector, while waves in lossy media are characterized by a complex wave vector. Therefore, when the imaginary part of the wave vector becomes comparable to the real part (as it occurs for increasing w in the present system) deviations from equation 1.7 are expected.

The measurements in Figs. 2.2 and 2.3 demonstrate the wide spectral tunability of hybrid plasmonic-photonic resonances in metallic nanorod arrays. In particular, the spectrum for $w = 110$ nm demonstrates the extremely narrow resonance linewidths (for plasmonic systems) that can be designed within a simple rectangular lattice. To quantify the linewidth, we fit the extinction measurements with a Fano model of the form given in equation 1.6. From the fit — shown as a dashed line overlying the measurements in Fig. 2.3 — we obtain a linewidth of 8.3 ± 0.6 meV, which is to the best of our knowledge the narrowest linewidth experimentally observed in the optical spectrum of any metallic nanostructure.

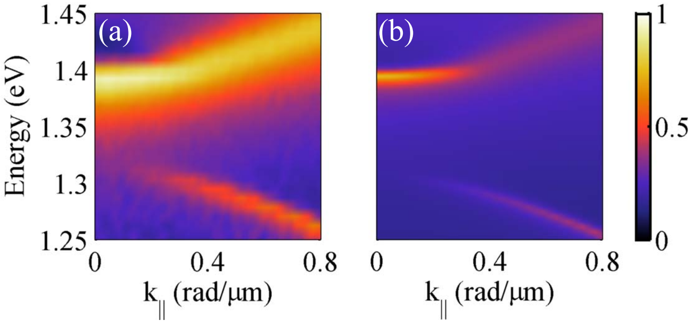

Figure 2.4: (a) Measurements and (b) finite element simulations, of the extinction spectrum of an array of gold nanorods with length of 450 ± 20 nm, height of 40 ± 2 nm , width of 120 ± 20 nm, in a lattice with constants $a_x = 600$ nm and $a_y = 300$ nm, surrounded by glass with $n = 1.45$.

2.2.2 Numerical simulations

We now turn our attention to the spatial properties of SLRs, and their relation with the energy gap in the spectrum. We use finite element method simulations (COMSOL) to elucidate the SLR characteristics in the presence and absence of a driving optical field. For the former, we use plane wave illumination at various angles of incidence as the driving field to obtain the extinction spectra. The extinction is calculated as $1 - T_0$, with T_0 the zeroth order transmittance obtained by Fourier decomposition. For the latter, we use COMSOL's eigenmode solver. In both cases, the dielectric surrounding the nanorods was modeled with a constant refractive index of $n = 1.45$, and the permittivity of gold was taken from Ref. [95]. Bloch-Floquet boundary conditions were used at the sides of the unit cell (along the periodicity axes), while perfectly matched layers were used at the ends (perpendicular to the periodicity axes). Further details on the simulations are provided in Refs. [80, 96].

Figure 2.4(a) shows a zoom into the energy gap observed in extinction measurements of a $w = 120$ nm array, with all other dimensions equal to the 5 arrays in the previous section.[2] Figure 2.4(b) shows the corresponding full-wave simulations, which reproduce well the experimental data. Small discrepancies in the amplitude and spectral width of the resonances are attributed to structural differences between the simulated and fabricated geometries, especially near the corners. Having validated our simulations, we now interpret the results.

The opposite sign for the group velocity $v_g = \partial\omega/\partial k_\|$ of the two SLR bands implies that the gap arises from the coupling of two counter-propagating surface modes. At the high-energy band edge, the dispersion of the upper SLR flattens, meaning v_g is reduced. Standing waves are formed at $k_\| = 0$, i.e., $v_g = 0$. At the low-energy band edge, the lower

---

[2] $w = 120$ nm array was not included in the 5 measurements of Fig. 2.2 because it was fabricated on a different substrate, and structural variations (within the error bars previously quoted) make quantitative comparison between different samples difficult. Nevertheless, qualitative behavior for arrays of varying w in both samples was equal, as shown for example by comparing data in Ref. [80] with Ref. [96]

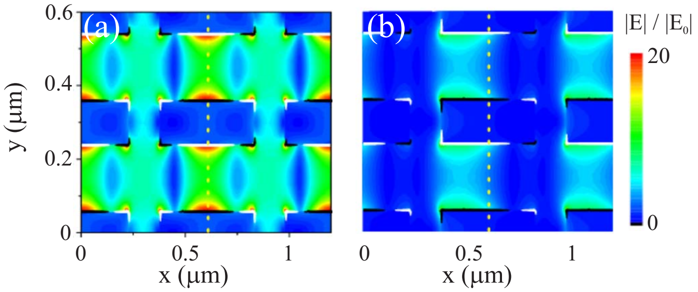

Figure 2.5: Electric field enhancement in color scale and surface charge (at an arbitrary phase) in black and white at the mid-height of the nanorods for the (a) upper and (b) lower surface lattice resonance driven by an incident plane wave with $k_{\|} = 0.15$ rad/μm and polarized along the short axis of the nanorods.

SLR becomes weaker and narrower as $k_{\|}$ decreases. This behavior is characteristic of a mode tending towards subradiance, where radiative damping is suppressed in a collective state with an anti-symmetric wave function [97]. As shown in nanoslit arrays [67], there is an intimate connection between subradiant damping and the opening of a gap in the dispersion relation of SPPs. Next, we elucidate the bright/dark origin of the upper and lower SLRs in terms of their modal symmetries.

In Fig. 2.5 we plot the electric field enhancement with respect to the incident field, in color as a function of the spatial coordinates at the mid-height of the nanorods. Both field plots in Figs. 2.5(a,b) pertain to the simulations in Fig. 2.4(b). In both Figs. 2.5(a,b), the incident plane wave has $k_{\|} = 0.15$ rad/μm, but the energy is different. Figure 2.5(a) corresponds to the peak energy of the upper SLR (1.4 eV), while Fig. 2.5(b) corresponds to the peak energy of the lower SLR (1.3 eV). The small non-zero $k_{\|}$ was chosen such that the lower SLR extinction is not negligible, i.e., it is not dark. Charges of opposite sign at the surface of the nanorods are represented by white and black contours.

Figure 2.5 illustrates the origin of the bright/dark character of SLRs on the modal symmetries. For plane wave excitation at normal incidence, the mode needs to be symmetric with respect to the plane defined by the intersection of the incident wave vector and polarization vector at the center of the nanorods. This symmetry plane is indicated by the dotted lines in Fig. 2.5. The upper SLR has symmetric field and charge distributions with respect to the symmetry plane[3]. Therefore, strong intra-rod and inter-rod dipole moments are excited, leading to a large extinction. This makes the upper SLR bright at normal incidence. In contrast, the lower SLR has an anti-symmetric field and charge distribution at $k_{\|} = 0$. The net dipole moment is therefore zero and the extinction vanishes. For oblique incidence the odd symmetry is broken. This is shown in Fig. 2.5(b) as a quadrupolar surface charge distribution displaced from the symmetry axis. The broken symmetry results in a nonzero intra-rod and inter-rod net dipole moment, which can be recognized from the charges of opposite sign inside the nanorods and for adjacent nanorods along the symmetry axis, respectively. As the incident angle increases, the odd-

---

[3] The symmetry is slightly broken by the oblique incidence.

symmetry progressively breaks, and the lower SLR gradually emerges from the darkness.

Next we consider the SLR eigenfields, i.e., in the absence of a driving field. The y-component of the electric eigenfield, E_y, is shown in Figure 2.6 for the bright and dark SLRs at $k_\parallel = 0$ in the $w = 110$ nm array. In both planes (xz and xy) intersecting the unit cell at its center, E_y displays an even parity for the upper SLR and an odd parity for the lower SLR, both with respect to the aforementioned symmetry axis. The odd parity of the lower SLR makes the mode dark at $k_\parallel = 0$. This confirms our intuition based on the simulations with a driving field impinging at a small angle of incidence.

In Fig. 2.7 we plot the normalized total electric eigenfields $|E|$ for the bright and dark SLRs at $k_\parallel = 0$ in arrays with varying w. The near field confinement of both SLRs increases as w increases. This effect is more clearly visible for the dark SLR [Fig. 2.7(b)], since it lacks a radiative component and its eigenfield decays monotonically out of the periodicity plane. In contrast, the upper SLR retains a radiative component for all w. The radiative fields of the upper SLR are more clearly visible in the spatial region away from the nanorods in Fig. 2.7(a), e.g., around the horizontal thin black line. Notice in this region that $|E|$ increases as w increases for the bright SLR, while the opposite occurs for the lower SLR. Since radiative fields dominate in this spatial region, it follows that the radiative portion of the total loss also increases with increasing w for the bright SLR. This effect, in combination with the increased near field confinement which leads to larger Ohmic losses, broadens the upper SLR linewidth at $k_\parallel = 0$ in the driven system. The latter observation is clear in experiments (Figs. 2.2 and 2.3).

Reference [96] provides further details on the spatial decay of SLRs. Therein, cross-sections of the eigenfields along the white dashed lines in Fig. 2.7 are analyzed. Reference [96] also discusses the dependence of the SLR eigenfields on $k_\parallel$, which modifies the balance between radiative and non-radiative losses for a given band. It should be mentioned that while the symmetries of the upper and lower SLR eigenfields are the same for arrays with different w (other dimensions fixed), the eigenenergies depend on w. Moreover, as the LSPR-RA detuning decreases for increasing w, the lower SLRs red-shifts at higher rate than the upper SLR. This leads to a progressive widening of the energy gap between the SLRs, as observed in experiments.

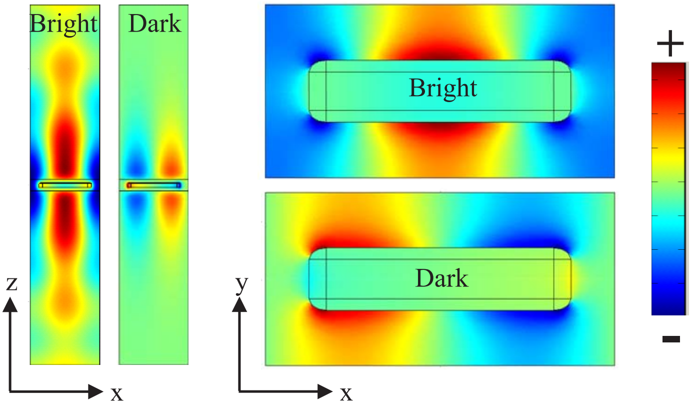

Figure 2.6: y-component of the electric eigenfield for the bright and dark modes at $k_{\parallel} = 0$. The xz and xy plane intersect the nanorods at their center. The nanorod width is $w = 110$ nm.

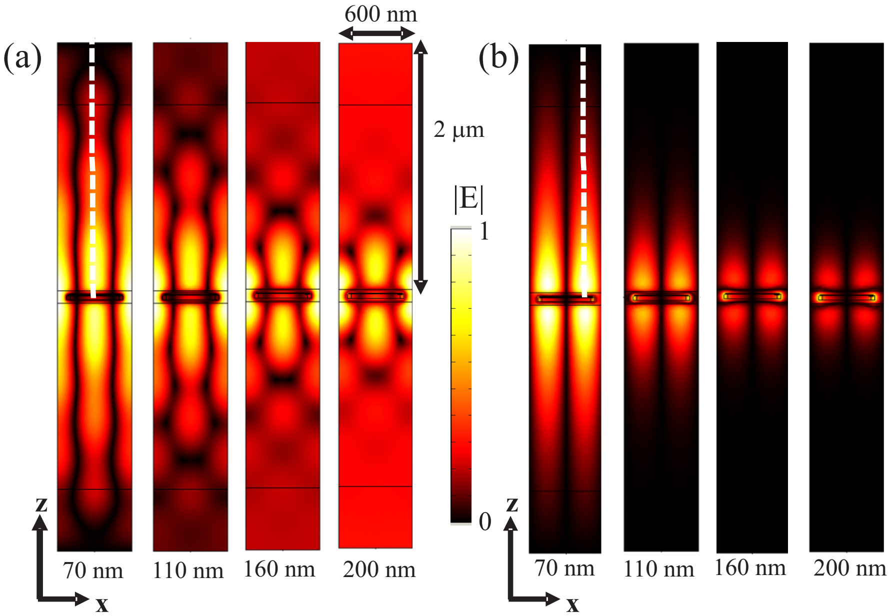

Figure 2.7: Total eigenfield $|E|$ cross-sections at the xz-plane for the (a) bright and (b) dark modes at $k_{\parallel} = 0$ in arrays with different nanorod width w, as indicated on the bottom of each plot. $|E|$ is normalized for each plot.

An interesting question concerns whether the bright and dark character of the upper and lower SLRs, respectively, can be reversed for different structures. For a variable nanorod width and other dimensions held constant, the measurements in Fig. 2.3 show that the upper SLR remains as a bright state and the lower SLR remains as a dark state at $k_\parallel = 0$ for any nanorod width. Interestingly, for lattices of cylindrical [85] or rectangular particles with much shorter lengths than those considered here [98], the bright and dark character of the upper and lower SLRs is reversed. This effect is related to the reversal of the modal symmetries characterizing the two states at $k_\parallel = 0$. Reference [98] explains this phenomenon is terms of the retardation of the scattered electric field with respect to the incident field. The length of the nanorod plays a central role in this retardation because the diffracted waves propagate along this direction.

To summarize, we have explored through numerical simulations the trade-off between field confinement and losses for SLRs in gold nanorod arrays. This is important for the design of structures targeting different applications. On the one hand, spectrally sharp SLRs can be employed to address emitters/receivers with sharp optical transitions. The electromagnetic fields of these sharp SLRs can extend well over a micron out of the periodicity plane, enabling an emission enhancement from emitters distributed in this region. On the other hand, spectrally broad SLRs can be employed to address emitters/receivers with broad optical transitions, and spatially localized on a deep sub-wavelength scale. These two cases correspond to the limit of small and large w discussed in this section. Everything in between can be addressed by smoothly varying w, or another parameter (e.g. lattice constant) that changes the LSPR-RA detuning.

2.2.3 A plane wave description of SLRs

Here we elucidate the properties of bright and dark SLRs in terms of a simple plane wave model taking into account the combination of multiple Bloch waves along the coordinate **x**, and propagating waves along the coordinate **z**. The model we employ is inspired by the paper of Engelen *et. al.* [99].

The combination of multiple Bloch waves and propagating waves leads to field solutions $\psi(x,z)$ to the wave equation of the form,

$$\psi(x,z) = \sum_m a_m e^{izk_z} e^{ix(k_\parallel + mG_x)}. \tag{2.1}$$

Here, m is the order of diffraction defining a Bloch harmonic with amplitude a_m. Each integer order m corresponds to a particular propagation constant component along **x** ($k_x = k_\parallel + mG_x$) and along z ($k_z = \sqrt{n^2k_0^2 - k_x^2}$). In general, $\psi(x,z)$ is given by an infinite number of Bloch harmonics. However, the spectrum of a grating is often strongly dominated by a few harmonics only. In this case, we may sum over those dominant harmonics only and obtain a solution that resembles faithfully the full solution. In this spirit, we proceed to compute the fields $\psi(x,z)$ resulting from the combination of three orders only, namely $m = 0, 1, -1$. To this end, we consider certain values for the coefficients a_m whose physical significance will become clear in brief. Furthermore, we set $k_0 = 0.9G_x$ for the free-space wave-vector magnitude, which has a wavelength satisfying the relation $k_0 = 2\pi/\lambda$, and impinges at normal incidence ($k_\parallel = 0$).

To begin, we let $a_0 = 0$ and $a_{+1} = -a_{-1}$. The resulting field magnitude $|\psi|$ is shown in Fig. 2.8(a). In this case the orders $m = +1$ and $m = -1$ are both evanescent along z. The

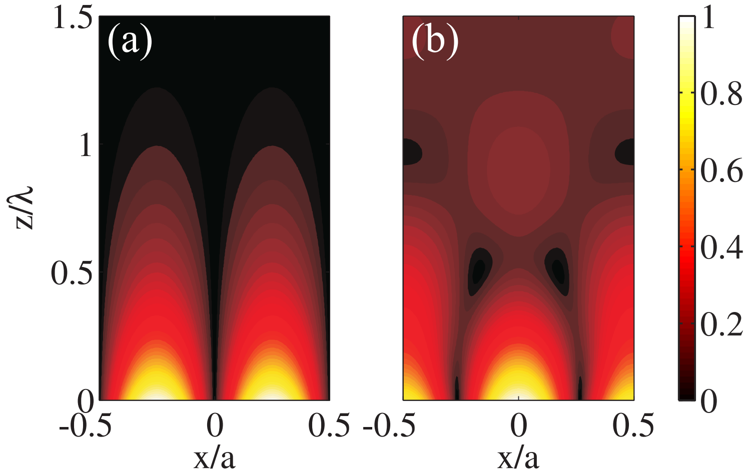

Figure 2.8: Normalized magnitude of the scalar field ψ calculated with equation 1.8 using the coefficients for the Bloch harmonics given in the text. (a) anti-symmetric mode, (b) symmetric mode.

mode is anti-symmetric, and the field ψ is purely imaginary (not evident from the plot, since we look at the complex modulus $|\psi|$) .The odd symmetry together with the condition $a_0 = 0$ forbids the coupling of this mode to radiation, making it dark. This manifests in Fig. 2.8(a) in that $|\psi|$ vanishes for large z, the cut-off being around $z = \lambda$.

Next we consider a symmetric mode which couples to radiation. The even symmetry requires $a_{+1} = a_{-1}$, while the value of a_0 determines the radiative strength. In Fig. 2.8(b) we plot $|\psi|$ for a choice $(a_0, a_{+1}, a_{-1}) = (0.2, 1, 1)$. The central lobe near $z = \lambda$ is the signature of a bright mode that couples to incident (or out-going) plane-waves.

Although the simple model discussed above does not consider the form factor of the grating, the y-dependence of the fields, nor the complex character of the Bloch wave vector in lossy media, a good agreement with numerical simulations is observed. Comparing the results in Fig. 2.8 with those in Fig. 2.7, we observe that the SLR eigenfields at $k_{\|} = 0$ are well reproduced by our model. Hence, we conclude that the few Bloch harmonics considered in the calculation, along with their respective coefficients, are sufficient to capture the essential physics of SLR eigenfields at $k_{\|} = 0$. Reference [96] shows that the SLR eigenfields at $k \neq 0$ are also well captured by our model, taking into account the same three Bloch harmonics here considered.

2.3 Enhancing light emission with SLRs

A central goal in nanophotonics is the development of efficient and tunable (in photon energy, directionality, and polarization) nanoscale light sources. Coupled semiconductor nanocrystal quantum emitters and metallic nanostructures offer a convenient platform for this purpose [35, 43, 46, 49]: the emission energy can be tuned by varying the nanocrystal size due to quantum confinement of charge carriers, while the emitted light can be enhanced and controlled by structuring the metal to sustain surface plasmons which are resonant with the emission. Modified emission spectra [51] and decay rates [49] have been observed by coupling quantum dots to localized excitations in metallic nanostructures. A stringent requirement in this approach concerns the positioning of the emitters relative to the structures. Since LSPR fields are confined on a deep sub-wavelength scale (typically 20 – 40 nm), emitters need to be positioned with this accuracy for their emission to be enhanced. In this section, we demonstrate the potential of SLRs to partially overcome this limitation and fulfill the aforementioned goal.

SLRs are ideal for enhancing the emission from thin luminescent layers. As shown in the previous section, the SLR field localization out of the periodicity plane can be controlled by varying the dimensions of the nanostuctures, e.g. the nanorod width. In the plane of the periodicity, SLR fields can extended several unit cells (>30) by virtue of their collective character [79, 85]. These properties allow to design the field overlap between SLRs and ensembles of emitters distributed in a spatially extended volume in the plane of the periodicity, but with sub-wavelength confinement out of the plane. Furthermore, in emission as in extinction, the tunable SLR dispersion enables to design the angular-dependent spectrum. In addition, the polarization-dependent response of anisotropic metallic nanostructures enables polarization selectivity in emission as well. In this section, we demonstrate polarization-selective directional light emission enhancements from a metallic nanoatenna array coupled to a thin (60 nm) layer of randomly oriented CdSe/CdS core/shell Quantum Rods (QRs). We show that in the presence of the nanoantennas, the otherwise unpolarized Lambertian emission from this thin layer is rendered polarized and directional.

Silver nanoantenna arrays with a total size of 3×3 mm^2 were fabricated by substrate conformal imprint lithography (SCIL) [100] onto a fused silica substrate. The array is comprised of nanorods with dimensions $340 \times 110 \times 20$ nm^3 arranged in a lattice with constants $a_x = 500$ nm and $a_y = 200$ nm. A 20 nm layer of Si_3N_4 was deposited on top of the array for a two-fold purpose: i) to passivate the silver, and ii) to avoid emission quenching by non-radiative processes which dominate at short metal-emitter distances (< 20 nm) [36, 101]. The QRs were synthesized following Carbone *et al.* [102]. They have diameters and lengths of 4.0 ± 0.6 and 36.1 ± 2.7 nm, respectively, and a photoluminescence quantum efficiency in solution of 65%. The absorbance spectrum is shown in Ref. [88], and the emission spectrum is shown ahead in Fig. 2.10(c). The absorption spectrum is not transcendental for the results herein because we investigate exclusively processes at the emission frequencies. Furthermore, the QRs will be optically pumped non-resonantly with respect to both the nanoantennas and the QR themselves, i.e., at much higher energy than the first exciton feature in the QR spectrum. We spin-coated a QR colloidal suspension of circa 11 μM on top of the Si_3N_4 layer, forming a compact layer of QRs with a thickness of 60 nm.

We measured the p-polarized variable angle zeroth-order extinction and photoluminescence enhancement (PLE) spectra of the structure. Figure 2.9(a) shows the extinction as a function of the incident photon energy and the in-plane component of the wave vector along the long axis of the nanorods. For the PLE measurements, the sample was

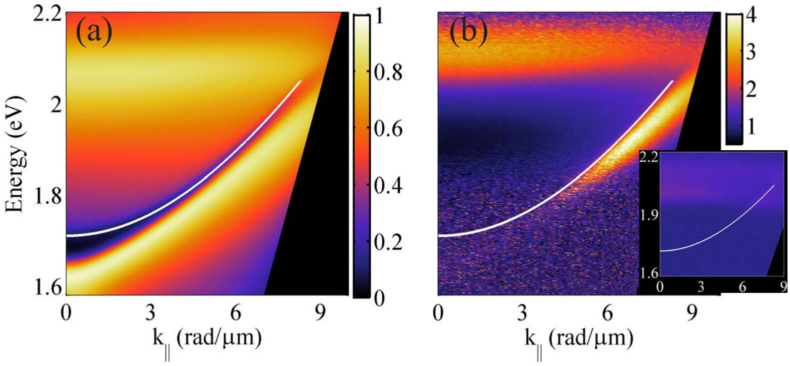

Figure 2.9: p-polarized (a) Extinction and (b) photoluminescence enhancement (PLE) dispersion diagram of a silver nanorod array covered by 40 nm layer of quantum rods. PLE for s-polarization is shown as an inset in (b). The white lines indicate degenerate $(\pm 1, 0)$ Rayleigh anomalies. The energy, wave vector, and color range, are equal for the inset and main panel.

pumped by a continuous wave laser beam with an energy of 2.81 eV and an irradiance of 2 mW/mm^2 at a fixed angle of incidence $\theta = 5°$. The pump irradiance was confirmed to be far below the saturation threshold for the QRs by measurements not shown here. From the variable angle emission of the QRs inside the array I_{in}, and outside the array I_{out}, we define the PLE as I_{in}/I_{out}. Figure 2.1(b) shows a schematic representation of the setup use to measure the variable angle PLE. Figure 2.9(b) shows the PLE dispersion diagram for p-polarized emission in the main panel, and s-polarized emission in the inset. The measurements are shown as a function of the emitted photon energy and $k_\parallel$. The white lines in both Figs. 2.9(a,b) indicate the degenerate $(\pm 1, 0)$ Rayleigh anomalies. The dispersion of the $(\pm 1, 0)$ RAs in this section is different from the previous section because $k_\parallel$ now points along the short axis of the nanorods, rather than along the long axis.

The broad peak in extinction near 2.07 eV in Fig. 2.9(a) corresponds to the LSPR for the short axis of the nanoantennas. The extinction dip near 1.69 eV at $k_\parallel = 0$, shifting towards higher energies for an inclined incidence, is due to degenerate $(\pm 1, 0)$ RAs. The peak in extinction under the RAs is the SLR. As discussed in the previous section, the SLR peak energy, dispersion, and linewidth, are determined by the LSPR-RA detuning. The salient feature of the present system is that only for large values of $k_\parallel$, the p-polarized SLRs cross in energy with the emission bandwidth of the QRs. For this reason, there is a resonant enhancement of the p-polarized emission by the SLRs at large values of $k_{||}$ only, as observed in the main panel in Fig. 2.9(b). Moreover, the PLE attains a dispersive character resembling the dispersion of the SLRs in extinction. The enhancement factor in the region where the QRs emit is roughly proportional to the extinction. At low energies the PLE displays only noise because the QRs do not emit in this spectral region. The inset in Fig. 2.9(b) shows that the SLR enhanced emission is absent for s polarization, where only a weak feature (PLE $\sim$ 1.3) near the RA condition is observed. The contrasting enhancement for s and p polarization arises from the anisotropy of the metallic nanostructures,

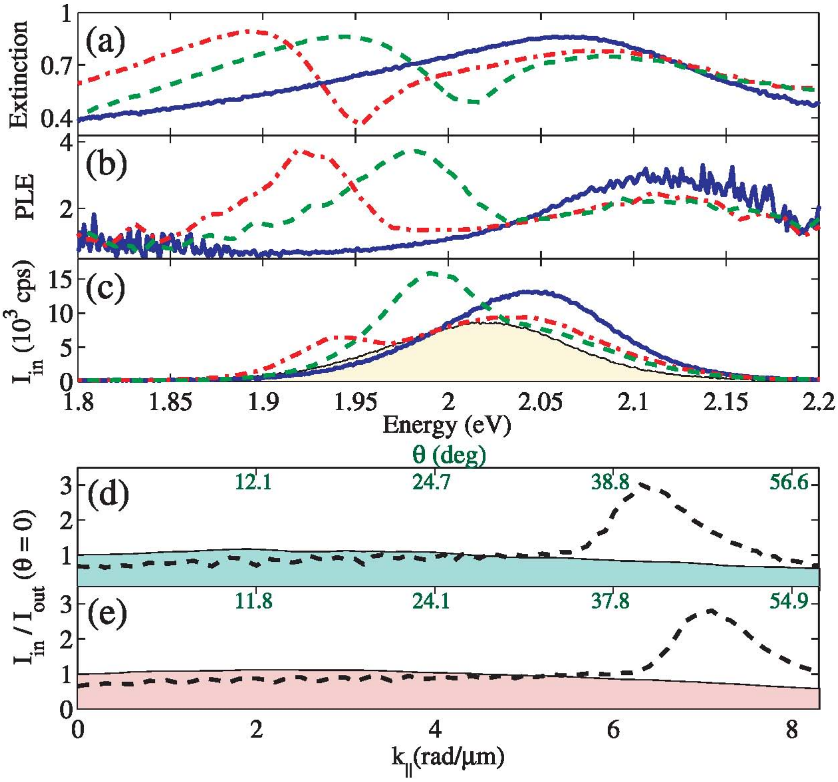

Figure 2.10: Extinction, (b) photoluminescence enhancement (PLE), and (c) emission inside the array, i.e. I_{in}, in 10^3 counts per second, at $k_{\|} = 0$ (blue solid lines), $k_{\|} = 7$ rad/μm (red dash-dot lines), and $k_{\|} = 7.9$ rad/μm (green dashed lines). The filled area in (c) is the emission outside the array, i.e. I_{out}, at $k_{\|} = 0$; I_{out} for the larger values of $k_{\|}$ (not shown here) has the same line shape as in $k_{\|} = 0$, but with a lower amplitude. (d) and (e) show the angular dependent emission for an energy of (d) 1.89 eV, and (e) 1.93 eV, with I_{in} as black dashed lines and I_{out} as a filled area. Both I_{in} and I_{out} are normalized to the value of I_{out} at $\theta = 0$ for each energy. The upper ticks indicate the value of the emission angle θ corresponding to the $k_{\|}$ values in the x-axis. All measurements are shown for p-polarized light.

which makes only p-polarized SLRs overlap with the emission of the QRs. Therefore, the structure acts as an enhanced and directional source of p-polarized light.

In general, the total PLE may be factored into its contributions from the pump and emission energies [51, 86]. We have verified that the influence of resonant pump enhancements is negligible by exciting the sample with different k-vectors and/or polarizations. Moreover, the total enhancement factor may change for different pump conditions, but the features in the PLE dispersion diagram remain unchanged because the emission is molded by the dispersion of the SLRs at the emission energies.

In Figs. 2.10(a,b) we show cuts of the spectra in Figs. 2.9(a,b), with the blue solid, red dash-dotted, and green dashed lines corresponding to $k_{||} = 0$, $k_{||} = 7$ rad/μm, and $k_{||} = 7.9$ rad/μm, respectively. The emission is enhanced in the spectral regions close to where the extinction is greatest, but the features are shifted. We attribute this shift to the different excitation conditions in extinction and PLE measurements. The extinction is governed by interference between incident and scattered fields, while the PLE is governed by local field enhancements at the positions of the emitters. This gives rise to a shift of the far-field with respect to the near-field spectra [103–106]. Here the shift is small, but in the next chapter we will demonstrate how the near-field to far-field contrast can be exploited to create a nearly transparent optical antenna array giving a large PLE.

In Fig. 2.10(c) we show the emission from the array, I_{in}, at the same values of $k_{\parallel}$ considered in Figs. 2.10(a,b). The filled area in Fig. 2.10(c) corresponds to I_{out} at $k_{\parallel} = 0$. For $k_{\parallel} = 0$, where only the LSPR overlaps with the emission of the QRs, there is a blue shift of the peak emission energy. In contrast, a red shift occurs for large $k_{\parallel}$, where the SLRs overlap with the emission of the QRs. In view of the size polydispersion of the QRs, which determines the emission linewidth of the ensemble due to inhomogeneous broadening, we attribute the blue shifted emission to a stronger interaction of the smaller QRs with the LSPR. By the same token, the red shifted emission is due to a stronger interaction of the bigger QRs with the SLRs. To asses the angular modification of the emission by the array, we plot in Figs. 2.10(d,e) I_{in} (dashed lines) and I_{out} (filled area) as a function of $k_{\parallel}$ for two photon energies, namely (d) 1.89 eV and (e) 1.93 eV. Both I_{in} and I_{out} are normalized to the forward emission outside the array, i.e., the value of I_{out} at $\theta = 0$, for each energy. Outside the array the emission is close to Lambertian for both energies. Inside the array the emission is suppressed for small $k_{\parallel}$ but enhanced within a narrow angular sector at large $k_{\parallel}$. The former indicates that resonant pump enhancement is negligible, since the emission is quenched in the absence of a resonant emission enhancement. The latter demonstrates the beaming of different energies into different directions via the coupling of the QR emission to SLRs at large $k_{\parallel}$.

To summarize, we have shown how surface lattice resonances in nanoantenna arrays enhance and modify the luminescence from a thin layer of quantum rods. By achieving spectral and angular overlap between surface lattice resonances and the emission spectra within a narrow angular sector only, a Lambertian source was transformed into a directional source of polarized light.

2.4 Conclusions

We have discussed in this chapter the physics of surface lattice resonances (SLRs), which arise from the coupling of localized surface plasmons to diffracted waves (Rayleigh anomalies) in a metallic nanoparticle array. The spectral and spatial properties of SLRs are widely tunable through the dimensions and geometry of the nanostructures and of the lattice. This tunability is advantageous for enhancing light emission directionality and polarization from thin luminescent layers extending over large areas. While in this chapter we have only explored the SLR properties as a function of a single structural parameter (the nanorod width), varying other parameters can give additional degrees of tunability and complexity in the optical response of the array. For example, in Chapter 5 we demonstrate how more complex structures enable to modify the forward-to-backward luminescence ratio. The mechanisms discussed in this chapter for tuning hybrid plasmonic-photonic resonances are also applicable to different types of modes, such as waveguide-plasmon polaritons as discussed in Chapter 3.

CHAPTER 3

LOCALIZED SURFACE PLASMONS COUPLED TO GUIDED MODES

We investigate the radiative coupling between localized surface plasmons in periodic arrays of metallic nanoantennas and guided modes in luminescent dielectric slab waveguides. In the first part of this Chapter, we investigate a silver nanoparticle array on top of a YAG:Ce optical waveguide. This system supports hybrid modes known as waveguide-plasmon polaritons, which lead to a simultaneously enhanced light emission and far-field induced transparency. In the second part of this Chapter, we investigate an aluminum nanoparticle array inside a dye-doped polymer waveguide. By varying the waveguide thickness we demonstrate the transition from weak to strong coupling between the same two localized surface plasmon and guided modes. The weak to strong coupling transition leads to a non-trivial relationship between extinction and emission dispersion diagrams. This relation allows to modify radiation patterns of nanoantennas without modifying the nanoantennas themselves, thereby representing an unprecedented design strategy for nanoscale light sources.

3.1 Introduction

Coupled systems are ubiquitous in physics. In recent years, the design and description of coupled nanoscale optical resonators has been greatly inspired by the field of atomic physics. Strong and weak coupling phenomena have been reported for light-driven molecular, metallic, and dielectric nanoscale systems. In the weak coupling regime, lineshapes akin to Fano resonances [29] and Electromagnetically Induced Transparency (EIT) [107] have attracted much attention [27, 28, 30, 31, 108–117]. Both of these effects arise from the interference between spectrally broad and narrow resonances, while the energy detuning sets them apart (zero-detuning for EIT vs. large detuning for Fano resonance). Interference can lead to a pronounced spatial and angular redistribution of optical states [118, 119], which has important implications for sensing [92, 120, 121], and enhanced spontaneous emission [59, 86, 88, 90]. On the other hand, the strong coupling regime — wherein the energy exchange rate between the coupled modes exceeds their loss rates — has been observed in various systems combining photons, excitons, and/or surface plasmons [122–129]. Advantageously, strong coupling enables to significantly modify the optical and chemical properties of the participating systems [130, 131]. This follows from the fact that the properties of strongly coupled states are intermediate to those of the bare states.

In this Chapter, we demonstrate the optical properties of localized surface plasmons resonances (LSPRs) coupled to guided modes in a luminescent slab. In the first section of this Chapter, we focus on a single structure composed of a silver nanoantenna array standing *on* a light-emitting dielectric slab waveguide. There, waveguide-plasmon polaritons (WPPs) emerge from the strong LSPR-guided-mode coupling [58]. These light-emitting WPPs display an extraordinarily enhanced emission at frequencies of strong dispersion and far-field induced transparency. In the second section of this Chapter, we investigate a periodic array of aluminum nanoantennas embedded *in* a polymer slab waveguide. There, by varying the waveguide thickness we demonstrate the transition from weak to strong coupling between the same two optical modes. We experimentally observe a non-trivial relationship between the light extinction and emission dispersion diagrams across the weak to strong coupling transition. Overall, the results in this Chapter convey a design principle for optical antenna arrays coupled to waveguides. In particular, we demonstrate the possibility to drastically modify nanoantenna radiation patterns without modifying the nanoantennas themselves.

3.2 Light-emitting waveguide-plasmon polaritons

3.2.1 Extinction and emission experiments

Figure 3.1(a) illustrates the structure we investigate in this section. It comprises a Ag nanoantenna array standing on a light-emitting slab waveguide. The latter is a 230 nm layer of Yttrium Aluminum Garnet doped with Ce^{3+} ions (YAG:Ce), fabricated by a sol-gel method onto a fused silica substrate as described in Ref. [132]. The relatively broad emission bandwidth [~ 0.4 eV full width at half maximum (FWHM)] of YAG:Ce allows us

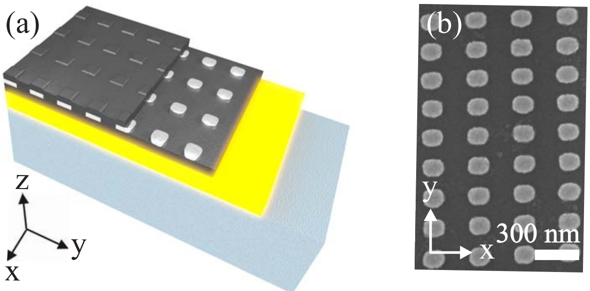

Figure 3.1: (a) 3D schematic of the light-emitting waveguide structure coupled to a silver nanoantenna array. From bottom to top, the layers are, 1 mm of SiO_2, 230 nm of YAG:Ce, and 20 nm silver nanoantennas surrounded by 20 nm of Si_3N_4 on top and bottom. (b) scanning electron micrograph of the fabricated silver nanoantenna array.

to probe the resonances of the structure in a wide spectral range. A 20 nm layer of Si_3N_4 was deposited on top of the slab for a two-fold purpose: i) to planarize the surface, and ii) to avoid emission quenching of Ce^{3+} ions in proximity to the metal [36, 101]. The Ag nanoantenna array was fabricated by substrate conformal imprint lithography [100] onto the Si_3N_4 layer. It has a total size of 2×2 mm^2. Figure 3.1(b) shows a scanning electron micrograph of the array. The dimensions of the nanoantennas are $90 \times 70 \times 20$ nm^3, and the lattice constants are $a_x = 300$ nm and $a_y = 200$ nm. The array was covered by a conformal 20 nm layer of Si_3N_4 to prevent the Ag from oxidizing. In what follows, we will show that despite the higher index of Si_3N_4 ($n \approx 2.0$) with respect to YAG:Ce ($n \approx 1.7$, as determined from ellipsometry) in the spectral range of interest, the small thickness of the Si_3N_4 layer and the presence of the nanoantennas enables the excitation of a guided mode in the YAG:Ce layer.

We measured the variable angle s-polarized extinction spectra of the structure. A collimated white light beam from a halogen lamp was linearly polarized parallel to the short axis of the nanoantennas (y-axis in Fig. 3.1). Using the same setup as in Fig. 2.1(a), the sample was rotated around the y-axis by a computer controlled stage with an angular resolution of 0.2°. This resulted in s-polarized incidence. The zeroth-order transmittance T_0 was collected by a fiber-coupled spectrometer. The extinction, defined as 1-T_0, is shown in Fig. 3.2(a) as a function of the incident photon energy and the wave vector component parallel to the long axis of the antennas, $\mathbf{k}_\parallel = k_0 \sin(\theta_{in})\hat{x}$, with k_0 the free space wave vector and θ_{in} the angle of incidence. We refer to the magnitude of $\mathbf{k}_{||}$ as $k_{||}$.

In Fig. 3.2(a), the extinction peak near 2.1 eV at $k_\parallel = 0$ is due to the dipolar LSPR along the short axis of the antennas. Its flat angular dispersion and broad linewidth are characteristic of localized resonances. The small size (70 nm) of the particle along the polarization axis determines its primarily dipolar response. The narrow peak on the high energy side corresponds to the fundamental TE_0 quasi-guided mode in the YAG:Ce slab. The mode is quasi-guided because it is coupled to the antennas and it is therefore leaky. The dispersion of this mode lies inside the free-space radiative cone because it is excited via the first diffraction order of the nanoantenna array. In light of Bloch's theorem as

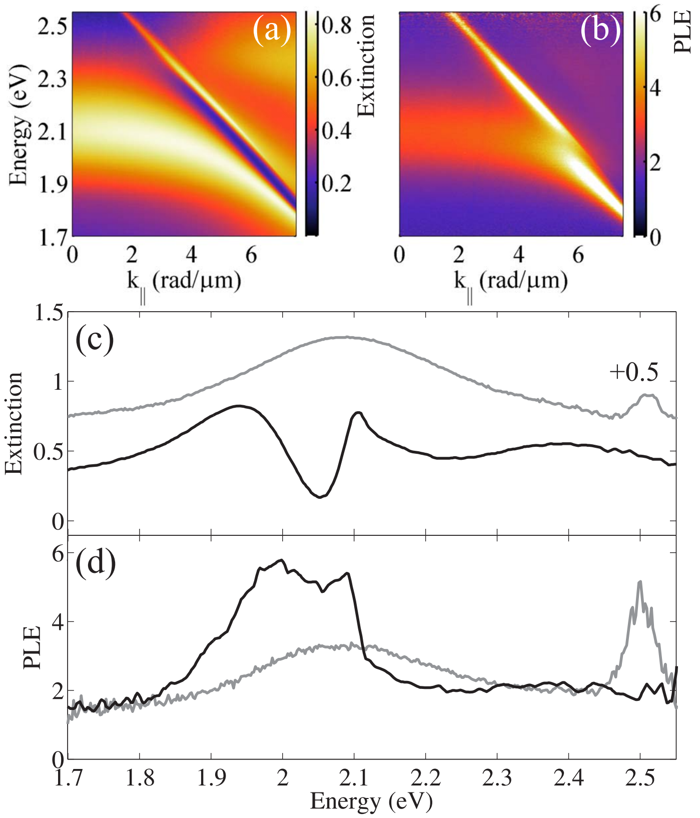

Figure 3.2: (a) Extinction, and (b) PhotoLuminescence Enhancement (PLE) of the emission from the YAG:Ce layer coupled to the antennas, normalized to the layer without antennas. (c) and (d) are cuts of (a) and (b), respectively, at $k_{\parallel} = 2.1$ rad/μm as gray lines and at $k_{\parallel} = 5.5$ rad/μm as black lines. The gray line in (c) is displaced by 0.5 for clarity.

discussed in Chapter 1, guided modes can be excited by free-space light impinging on periodic structures if the mode lies within the cones of the first diffraction order radiating in the high- and low-index media, but inside the free-space radiative cone of the zeroth order. This is the case here. Furthermore, the avoided resonance crossing in the measurements in Fig. 3.2(a) suggests that the coupling between the LSPR and the guided mode is strong. As $k_{\parallel}$ increases, the LSPR becomes dispersive and acquires a narrower linewidth. The opposite occurs for the quasi-guided mode. This exchange of modal properties, as the detuning parameter $k_{\parallel}$ is varied, is the signature of strong coupling.

Next we present photoluminescence enhancement (PLE) measurements. Using the setup described in Fig. 2.1(b), the sample was optically pumped by a continuous wave laser beam with an energy of 2.8 eV, FWHM = 30 meV, a power far below saturation, and impinging at an angle of 10°. The photoluminescence passed through a polarization analyzer, and was collected as a function of the angle θ_{em} subtended by the detector and the normal to the sample. The detector was rotated around the y-axis, collecting s-polarized light with $\mathbf{k}_\parallel = k_0 \sin(\theta_{em})\hat{x}$. The angular resolution was the same as in the extinction measurements.

Figure 3.2(b) shows the measured PLE, defined as I_{in}/I_{out} with I_{in} the emission from the YAG:Ce slab in the presence of the nanoantenna array, and I_{out} without the array. For small $k_\parallel$, where the LSPR and guided mode are largely detuned, the PLE features qualitatively resemble those in extinction. Near zero detuning ($k_\parallel \approx 5.5$ rad/μm), a remarkable contrast between extinction and PLE occurs: the emission is greatly enhanced in a spectral window for which the extinction is reduced, i.e., the sample is nearly transparent. We illustrate examples of large detuning $k_\parallel = 2.1$ rad/μm (gray line) and near zero detuning $k_\parallel = 5.5$ rad/μm (black line), for light extinction in Fig. 3.2(c) and PLE in Fig. 3.2(d). For large detuning, the broad extinction peak due to the LSPR leads to a modest PLE with a similar lineshape. The narrow peak with a Fano-like lineshape due to the quasi-guided mode leads to a larger PLE. This contrasting enhancement is attributed to the different field overlap between the optical modes and the emitters, as we illustrate further below by means of simulations. Near zero detuning (black lines in Fig. 3.2), the LSPR and guided mode are more strongly hybridized. The extinction displays a broad peak split by a narrow window of induced transparency near 2.05 eV. Similar spectral line shapes have been observed in atomic systems near the transition from the EIT regime into the Autler-Townes splitting regime [133, 134], which occurs as the coupling strength between the modes increases. Interestingly, the far-field transparent spectral region displays a strong PLE due to a light-emitting WPP. Such a contrast between the extinction and emission properties of a nanoantenna-coupled system is attractive for enhancing the performance of solid-state light emitting devices. In particular, directional emission enhancements can be obtained by selectively positioning emitters in spatial regions with intense local fields but reduced far-field extinction. Such a configuration benefits from strong local electromagnetic field enhancements at the positions of the emitters, while at the same time minimizes absorption losses in the metal which often hinder the applicability of plasmonic nanoantennas.

Finally, we address the relevance of the excitation source for the PLE results. Notice that at energies far from any resonance the PLE is approximately unity. This indicates that pump enhancements (resonant processes at the excitation energy) are negligible. Thus, the magnitude of the PLE could be further increased by matching the momentum of the pump photons with that of the quasi-guided modes at the excitation energy. This can be achieved with the nanoparticle array, or alternatively with a prism as shown in Ref. [132]. In Ref. [132], a 30-fold pump enhancement was achieved with negligible enhancement at the emission energies. Pumping resonantly with the nanoantennas would increase the PLE magnitude of light-emitting WPPs, but their dispersive properties would remain essentially unchanged.

3.2.2 Numerical simulations

We performed finite element method simulations (COMSOL) under plane wave illumination to illustrate the field distributions associated with the LSPR and quasi-guided

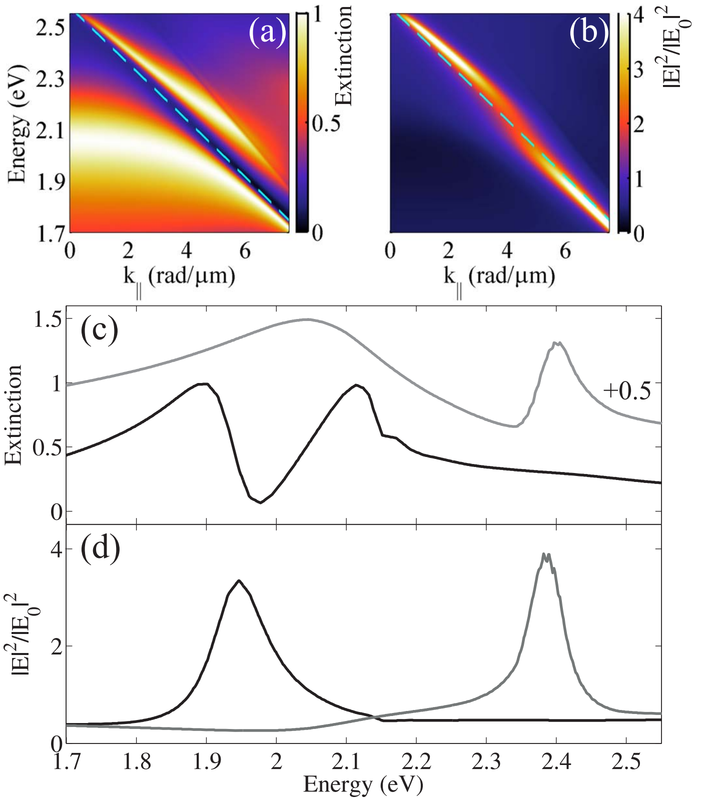

Figure 3.3: Finite element method simulations of (a) the extinction of an array of metallic nanowires with 70 nm width and 300 nm periodicity, and (b) the corresponding average electric field intensity enhancement in the YAG:Ce slab. The dashed line in (a) and (b) is an analytical calculation of the TM_0 guided mode as described in the text. (c) and (d) are cuts of (a) and (b), respectively, at $k_\parallel = 2.1$ rad/μm as gray lines and at $k_\parallel = 5.5$ rad/μm as black lines. The gray line in (c) is displaced by 0.5 for clarity.

modes. For ease of computation, we employ a 2D system (1D periodic) with the same periodicity as the experimental structure along the x-axis, i.e. along $k_\parallel$. The width and height of the simulated metallic wire were chosen to be 70 nm and 20 nm, respectively. These dimensions determine the spectral features of the LSPR. For TM polarization, the coupling between LSPRs along the width of the metallic wire and the fundamental TM guided mode gives rise to the same physics in light extinction observed in our 2D periodic system for TE polarization [58]. The optical data for YAG:Ce was taken from ellipsometry measurements, for Ag it was taken from Ref. [95], and we set a constant refractive index of $n = 2.0$ for Si_3N_4 and $n = 1.43$ for SiO_2. Bloch-Floquet boundary conditions were used for the sides of the unit cell (along the periodicity axis), and perfectly matched layers on the top and bottom.

Figure 3.3(a) shows the simulated extinction spectra. The cyan dashed line indicates the dispersion of the fundamental TM_0 guided mode in an effective YAG:Ce + Si_3N_4 slab sandwiched between air and glass. The calculation is performed as described by Yariv and Yeh [57], and assumes that the refractive index of the middle layer is given by the average refractive index of YAG:Ce and Si_3N_4 weighted by the corresponding areas. The good agreement between the dashed line and the transparency band in Fig. 3.3(a) — arising at the eigenvalue of the bare guided mode — justifies our effective medium approximation for the refractive index of the middle layer. Figure 3.3(b) shows the simulated electric field intensity enhancement in the YAG:Ce slab. It is defined as $|E|^2/|E_0|^2$ with E and E_0 the total and incident electric field, respectively. Both E and E_0 are spatially averaged over the interior of the YAG:Ce slab. Figures 3.3(c) and 3.3(d) display cuts of the extinction and $|E|^2/|E_0|^2$, respectively, at a large detuning of $k_\parallel = 2.1$ rad/μm as gray lines, and near zero detuning of $k_\parallel = 5.5$ rad/μm as black lines. At large detuning, $|E|^2/|E_0|^2$ is greater at the quasi-guided mode energy (2.4 eV) than at the LSPR energy (2.05 eV). The larger field enhancements from the quasi-guided mode at the position of the emitters explain the greater emission enhancement from this mode at large detunings (small $k_\parallel$). Near zero detuning, $|E|^2/|E_0|^2$ is greatest within the far-field transparency window. This counterintuitive behavior — near-field maximum at far-field minimum — arises from the interference nature of extinction, which allows for a partial cancelation of the far-field response even in the presence of relatively strong local fields. This possibility is at the heart of recent theoretical proposals for cloaking a sensor [135]. Such a cloaked sensor could see a near-field object without being seen by a distant observer [136]. Our measurements support the extension of these ideas to the domain of light emission, where near-field coupled emitters can profit from enhanced local fields in spectral regions of far-field induced transparency.

Next, we inspect in Fig. 3.4 the total electric field enhancement with respect to the incident field at the same values of large detuning [panels (a)-(c)] and near zero detuning [panels (d)-(e)] inspected in Figs. 3.3(c,d). Figures 3.4(a,d) correspond to the high energy extinction peak, Figs. 3.4(b,e) correspond to the extinction dip, and Figs. 3.4(c,f) correspond to the low energy extinction peak. At large detuning, Fig. 3.4(a) shows an enhanced field concentration in the YAG:Ce layer for the quasi-guided mode, whereas Fig. 3.4(c) shows enhanced fields near the metallic structure for the LSPR. Figure 3.4(a) shows that the quasi-guided mode resides primarily in the YAG:Ce waveguide, with only a small fraction of the total field enhancement in the Si_3N_4 layer. Near zero detuning, the field distributions in Figs. 3.4(d) and 3.4(f) are similar, because the split energy peaks correspond to hybrid states with approximately equal weights of the underlying bare states. A particularly interesting situation arises in Fig. 3.4(e), where strong local field enhancements are observed in the YAG:Ce layer at an energy and wave vector for which the structure is nearly transparent. Comparing Fig. 3.4(e) and Fig. 3.4(b) reveals the critical role of the eigenmode detuning for creating this effect. The field enhancement at the eigenfrequency of the guided mode is greatest when the detuning with the LSPR is zero [Fig. 3.4(e)] than when it is large [Fig. 3.4(b)].

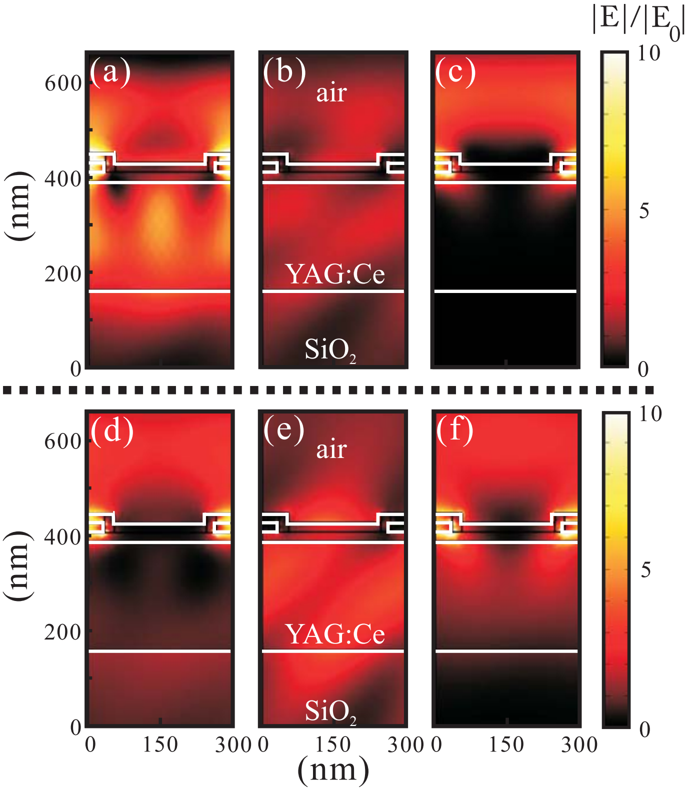

Figure 3.4: Field enhancement for large waveguide-plasmon detuning (a)-(c), i.e., at $k_{\|}$ = 2.1 rad/μm, and near zero detuning (d)-(f), i.e., at $k_{\|}$ = 5.5 rad/μm. (a) and (d) correspond to the high energy extinction peak, (b) and (e) correspond to the extinction dip, and (c) and (f) correspond to the low energy extinction peak, all referring to the spectra in Fig. 3.3. The metallic antennas, surrounded by 20 nm of Si_3N_4, are located at the interface between the YAG:Ce layer and air.

3.2.3 Coupled oscillator analog

The physics involved in the mode coupling discussed above is well captured by a coupled oscillator model introduced in Chapter 1.3.2. Classical analogs to EIT [109, 137], Fano resonances [31, 113], and strong coupling [138], have been presented with similar models. Here we use the model presented in Eq. 1.5 as follows. We define the eigenfrequency of the first oscillator as $\omega_1 = \omega_0$, and we detune the eigenfrequency of the second oscillator by an amount δ, i.e. $\omega_2 = \omega_0 - \delta$. In analogy to the extinction measurements, we drive the first oscillator directly by a harmonic force $F = F_0 e^{-i\omega_d t}$, and calculate its dissipated power given by $P_1 = \frac{1}{2}\Re[F^* \dot{x}_1]$ with $\dot{x}_1$ the velocity. We consider that only the first oscillator is driven directly by F because only the LSPR is driven directly by the incident electromagnetic field. Since the dispersion relation of the guided mode lies below the free-space light line, it can

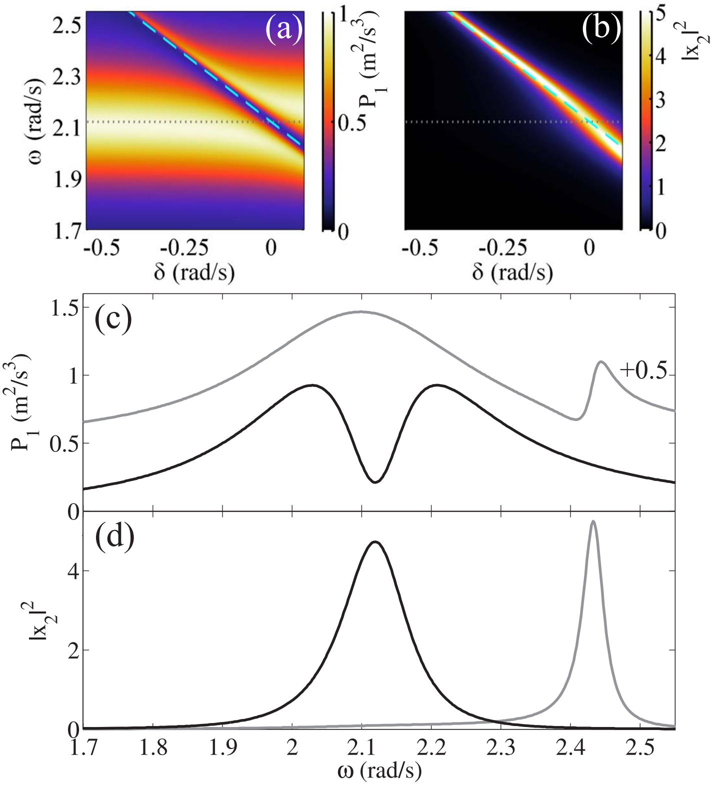

Figure 3.5: a)Power dissipated by the first oscillator, and (b) displacement squared response of the second oscillator. In (a) and (b), the dotted line indicates the eigenfrequency of the first oscillator, representing the LSPR, while the dashed line indicates the eigenfrequency of the second oscillator, representing the guided mode. (c) and (d) are cuts of (a) and (b), respectively, at $\delta = -0.3$ rad/s as gray lines and at $\delta = 0$ as black lines.

only be excited through the periodic nanoantenna array. This is the origin of the driving term on the right hand side of Eq. 1.5. Finally, we integrate the dissipated power over one period of oscillation and scan the driving frequency ω to obtain the spectrum, which we plot as a function of δ in Fig. 3.5(a). For the calculation, we set the eigenfrequency to $\omega_0 = 2.12$ rad/s, the damping rates to $\gamma_1 = 0.4$ rad/s, $\gamma_2 = 0.02$ rad/s, the coupling rate to $\Omega_{12} = 0.6$ rad/s, and the force per unit mass to $F_0 = 0.88$ m/s^2, all to match the power dissipated by the oscillator to the extinction measurements. For the first oscillator we have $Q_1 = \omega_0/\gamma_1 = 5$, which is typical for damped LSPRs as shown in Chapter 2. The lower damping of the second oscillator reflects the lower losses of the waveguide, for which absorption is nearly negligible and out-of-plane scattering represents a relatively weak loss mechanism.

To model the local field intensity enhancement $|E|^2/|E_0|^2$ in the waveguide, we calculate the displacement from equilibrium (squared) response of the associated oscillator, i.e., $|x_2|^2$. It was recently shown that the resonance in the displacement spectrum of a single harmonic oscillator can be associated with the near-field resonance of a metallic nanoparticle [139]. Moreover, the peak spectral shift in the displacement with respect to the velocity (dissipated power) accounts for the shift of the near-field with respect to the far-field [139]. The origin of this shift in the single oscillator spectrum was illustrated in Fig. 1.1, where we discussed how the oscillator's damping shifts the maximum in the velocity spectrum with respect to the displacement spectrum. Here, we investigate this phenomenon in a coupled system. In Fig. 3.5(b) we show the dependence of the near-field analogous quantity on the detuning parameter δ. In Figs. 3.5(c) and 3.5(d) we make cuts of both 3.5(a) and 3.5(b) at a large detuning of $\delta = -0.3$ rad/s as gray lines, and at zero detuning as black lines. The calculated spectra resemble the measured (Fig. 3.2) and simulated (Fig. 3.3) spectra. At large detuning, the dissipated power spectrum exhibits a Fano-like line shape near the eigenfrequency of the second oscillator. The peak in the displacement spectrum of the second oscillator near this feature resembles the large emission enhancements from the quasi-guided mode at large detunings. Thus, the oscillator analog confirms once more that the emission from the waveguide is enhanced according to the local field spectrum rather than the far-field spectrum. In the case of zero detuning, the model also shows that the coupled system displays a minimum in the dissipated power by the first oscillator (representing the driven electrons in the metal), while the displacement response of the second oscillator (representing the local electromagnetic field enhancement in the waveguide) is enhanced. Hence, in its simplicity, the coupled oscillator model captures the essential physics, and lends itself for a straightforward interpretation of the results.

3.2.4 Concluding remarks for this section

To summarize, we have presented a novel approach for achieving large emission enhancements from far-field transparent optical antenna arrays. The system studied comprises a periodic array of silver nanoantennas on top of a light-emitting slab waveguide. This system supports hybrid modes, namely waveguide-plasmon polaritons, with optical properties strongly dependent on the detuning of the bare LSPR and guided modes. At zero detuning, interference of these modes makes the nanoantennas transparent to far-field plane waves, at the same conditions for which electric fields are strongly enhanced in the waveguide. These results open a new avenue for investigating EIT-related phenomena, such as slow light, strong dispersion, and coupling-induced transparencies, in the context of light emission as well as extinction. In the next section, we investigate a broader range of structures to demonstrate how the same plasmonic system can transition from weak to strong coupling with a light-emitting waveguide.

3.3 From weak to strong coupling between LSPRs and guided modes

In this section we demonstrate how localized surface plasmons in the same nanoantenna array (different from the previous section) transition from weak to strong coupling with the fundamental guided mode in a luminescent dielectric slab. As discussed in Chapter 1, nanoantennas provide an interface between plane waves in the far-field and localized energy in the near-field, while dielectric waveguides can guide this energy to a desired position with low losses. Therefore, understanding the conditions enabling an efficient coupling between these two photonic building blocks is an important endeavour in optics. Indeed, several theoretical and experimental results (including those in the previous section) have demonstrated that light can be received, transferred, or emitted, in unconventional ways when metallic resonators are either strongly of weakly coupled to dielectric waveguides [58, 111, 112, 140, 141]. However, the transition from weak to strong coupling between the same two nanoantenna and waveguide modes has not been reported in the literature, to the best of our knowledge. Here we map this transition by varying the thickness of a polymer waveguide within which a metallic nanoantenna array is embedded. We demonstrate the impact of this transition on the variable angle light extinction and emission spectra of the system. The emission stems from luminescent molecules embedded in the waveguide. We find that an optimum waveguide thickness exists for increasing the ratio of the coupling rate to the loss rates, thereby providing a design principle for accessing the strong coupling regime. Finally, we discuss differences between the light emission and extinction spectra across the weak-to-strong coupling transition, and we explain their origin on the transmutation of coupled optical modes with varying degree of field confinement.

3.3.1 Extinction and emission experiments

Figure 3.6(a) illustrates the sample. An aluminum nanoantenna array with a total size of 2×2 mm^2 was fabricated by substrate conformal imprint lithography [100] and reactive ion etching of aluminium onto a fused silica substrate. Figure 3.6(b) shows an inclined view (43° off the normal) scanning electron micrograph of the array. The nanoantennas are approximately disks with a diameter of 130 ± 20 nm and a height of 150 ± 10 nm, arranged in a square lattice with a constant $a = 370 \pm 5$ nm. On top of the array we spin-coated a toluene solution with polystyrene and the organic dye Lumogen F305. Consequently, the toluene evaporated leaving a dye-doped polystyrene layer. The refractive index of this layer is higher than the underlying silica and overlying air, rendering the embedding of the array in a slab waveguide. We varied the thickness t of this waveguide by controlling the spin-rate of the deposition and the viscosity of the solution. The latter was controlled through the polystyrene-to-toluene ratio, while the dye-to-polystyrene ratio (determining the final molecular concentration in the waveguide) was held constant at 3 weight % . This relatively low molecular concentration allows us to exclude the influence of the molecules on the nanoantenna-waveguide coupling, but provides a significant emission intensity to probe the coupling effects in the nanoantenna enhanced near-fields.

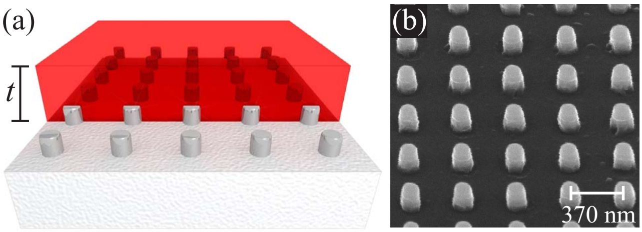

Figure 3.6: (a) 3D schematic representation of the sample. An aluminum nanoantenna array stands on a SiO_2 substrate, and is covered by a luminescent slab waveguide of thickness t. (b) Inclined-view (43° off the normal) scanning electron micrograph of the nanoantenna array prior to the deposition of the waveguide.

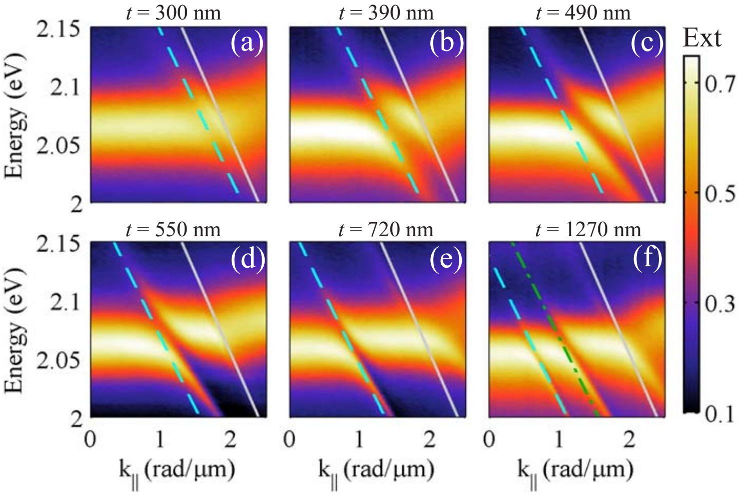

Figure 3.7: Extinction measurements of the structure in Fig. 3.6, for a waveguide thickness (a) t = 300 nm, (b) t = 390 nm, (c) t = 490 nm, (d) t = 550 nm, (e) t = 720 nm, and (f) t = 1270 nm. The gray solid line, identical for all plots, indicates the Rayleigh anomaly with a refractive index of 1.44 (the substrate). The cyan dashed line, shifting towards lower $k_{\|}$ for increasing t, indicates the TM_0 guided mode calculated as discussed in the text. The green dash-dotted line in (f) indicates TM_1 guided mode.

Figure 3.7 shows a series of extinction measurements of the same nanoantenna array embedded in waveguides of different thickness. The sample is illuminated by a collimated (angular spread < 0.1°) TM-polarized white light beam from a halogen lamp, while a fiber-coupled spectrometer collects the transmitted light in the far-field. The experimental setup is identical to the one in Figure 2.1(a). The extinction is defined as 1-T_0 with T_0 the zeroth-order transmittance. We plot the extinction in color — same scale for all plots — as a function of the incident photon energy and in-plane momentum $k_{\|}$. A computer-controlled stage was used to rotate the sample by an angle θ_{in}, thereby changing the in-plane component of the wave vector $\mathbf{k}_{\|} = k_0 \sin(\theta_{in})\mathbf{a}$. k_0 is the magnitude of the free space wave vector and **a** is a unit vector parallel to one of the two equivalent lattice vectors. We refer to the magnitude of $\mathbf{k}_\parallel$ as $k_\parallel$. The angular resolution of the measurements is 0.2°. We focus on TM polarization because excellent spectral overlap between the coupled resonances and the emission from the dye molecules aids to bring out the nanoantenna-waveguide hybridization effects in both emission and extinction of TM-polarized light. However, the onset of strong coupling is not particular for one polarization, as confirmed for instance by experiments with TE-polarized light in the previous section.

We now interpret the various features observed in the measurements in Fig. 3.7. For all t, the broad extinction peak near 2.07 eV with a flat angular dispersion at small $k_\parallel$ corresponds to the excitation of localized surface plasmon resonances (LSPRs). A plane wave that excites LSPRs can also be diffracted grazing to the surface of the array, leading to the so-called Rayleigh anomaly (RA) condition. The gray solid line overplotted on the measurements in Fig. 3.7 indicates the RA in glass, with a dispersion given by $E_{R\pm}(k_\parallel) = \frac{\hbar c}{n_g}|k_\parallel + mG|$. Here, $m = -1$ is the relevant order of diffraction, $G = \frac{2\pi}{a}$ is the magnitude of the reciprocal lattice vector, and $n_g = 1.44$ is the refractive index of the glass substrate. The periodic array may also enable the plane wave excitation of a guided mode in the polymer layer, which has a refractive index higher than its surroundings. The cyan dashed line, changing with t, indicates the dispersion relation of fundamental TM_0 guided mode calculated using the formalism described by Yariv and Yeh [57]. We solve for the bound modes in a dielectric slab with refractive index $n_p = 1.58$ (polystyrene), sandwiched between semi-infinite media with $n_a = 1.0$ (air) and $n_g = 1.44$ (glass). The thickness t of the slab is obtained from profilometry measurements of the dye-doped polystyrene layer in experiments.

Figure 3.7 shows several dispersive features in extinction crossing or anti-crossing with the LSPR depending on t. The feature near the RA condition remains as a small perturbation on the LSPR for all t, and we therefore not dwell on it further. We focus on the feature near the LSPR-TM_0-guided-mode crossing, which varies pronouncedly with t. For $t = 300$ nm, Fig. 3.7(a) shows a weak narrow feature crossing with the LSPR without significantly affecting it. This thin waveguide is close to cut-off, so the weakly confined TM_0 guided mode dispersion follows closely the RA dispersion. As t increases, the guided mode shifts away from the RA towards lower $k_\parallel$, and its signature in the spectra is clearly distinguished from the RA feature. In Fig. 3.7(b) we begin to see signatures of hybridization between the LSPR and TM_0 guided mode. For increased t [Figs. 3.7(c,d)], a mode splitting emerges near zero detuning, where the energies of the bare LSPR and TM_0 guided mode cross but the coupled modes anti-cross. As $k_\parallel$ transits across the zero detuning point, the coupled modes gradually exchange their resemblance to one or the other of the bare modes. This adiabatic mode exchange across the zero detuning point is, qualitatively speaking, the signature of strong coupling. Strong LSPR-guided mode coupling leads to hybrid modes known as waveguide-plasmon polaritons, as discussed in the previous section. For $t = 720$ nm [Fig. 3.7(e)], the energy splitting between the same two modes is reduced, and for $t = 1270$ nm [Fig. 3.7(f)] the splitting is much smaller than the linewidths (weak coupling). For $t = 1270$, the higher order TM_1 guided mode [green dash-dotted line in Fig. 3.7(f)] is also excited. However, we do not observe indications of strong coupling between the TM_1 guided mode and the LSPR for any t.

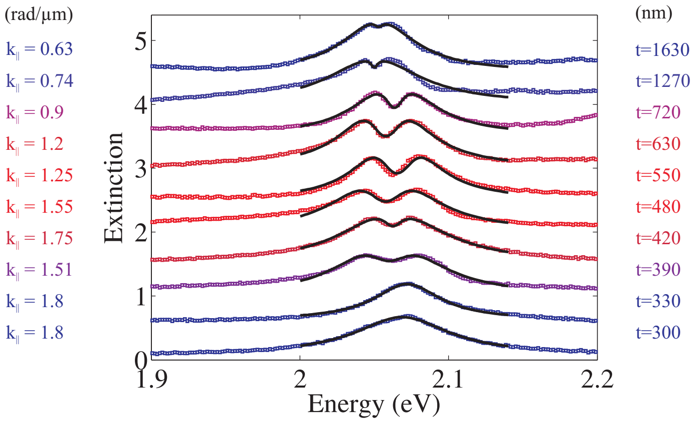

Figure 3.8: Extinction measurements at the value of $k_\parallel$ corresponding to zero detuning between the TM$_0$ mode and the localized surface plasmon resonance in arrays embedded in waveguides of different thickness t. For each cut, the value of $k_\parallel$ and t is indicated at the left and right of the figure, respectively, in the same color as the measurement. For successive increments in t, the extinction is increased by 0.5 for clarity. The black lines overplotted with the measurements are fits with a coupled oscillator model as described in the text.

An interesting observation in the dispersion diagrams in Fig. 3.7 is that the calculated TM$_0$ guided mode and the corresponding feature in extinction are in better agreement for thicker [Figs. 3.7(e,f)] than for the thinner [Figs. 3.7(a,b,c,d)] waveguides. We believe that this is due to the perturbation of the "bare" waveguide structure by the nanoantennas. For thinner waveguides a higher fraction of the dielectric slab is occupied by the nanoantennas. Therefore, the actual structure deviates more pronouncedly from the planar layer considered in the calculations. The most significant deviations between the calculated TM$_0$ guided mode and the corresponding feature in extinction are observed for the structures displaying the strongest splittings [Figs. 3.7(c,d)], likely because in these cases the perturbative particle has a greater overlap with the guided mode eigenfield.

Next, we analyze in Fig. 3.8 the extinction measurements for various t [more values than shown in Fig. 3.7(a)-(f)] at the value of $k_\parallel$ corresponding to zero LSPR and TM$_0$ guided mode detuning. This value of $k_\parallel$ (shown on the left of each plot) was established on the basis of a non-linear least squares fit of a model system — coupled harmonic oscillators — to the data, as we explain next. In matrix form, the equations of motion of the model system are,

$$\begin{pmatrix} \omega_L^2 - \omega^2 - i\gamma_L\omega & \Omega\omega \\ \Omega\omega & \omega_G^2(k_\parallel) - \omega^2 - i\gamma_G\omega \end{pmatrix} \begin{pmatrix} x_L \\ x_G \end{pmatrix} = \begin{pmatrix} \frac{F}{m} e^{-i\omega t} \\ 0 \end{pmatrix}, \tag{3.1}$$

where we have assumed time-harmonic solutions. ω_L and $\omega_G(k_\parallel)$ are the eigenfrequencies of the LSPR and TM$_0$ guided mode, γ_L and γ_G are their respective loss rates, while x_L and x_G are the oscillator displacements from equilibrium. $\Omega\omega$ represents the coupling strength between the two oscillators. On the right hand side of Eq. 3.1 appears the driving force per unit mass, $\frac{F}{m}e^{-i\omega t}$, which represents the incident optical field with frequency ω. This force drives directly the LSPR only because in the absence of scatterers, the guided mode is not directly driven by a plane wave incident from the far-field. The guided mode is excited indirectly through the array. Our model assumes frequency-independent dissipative and coupling terms, which is valid for restricted energy ranges only. While relaxing these constraints could lead to a better quantitative agreement with the experiments, we show that a good fit and a reasonable description emerge in the spectral region of interest despite these simplifications. Finally, we point out that under the assumption that all coupling ($\Omega\omega$) and loss ($\gamma_L\omega$ and $\gamma_G\omega$) terms scale linearly with the driving frequency ω, their values can be directly compared quantitatively for any ω.

To establish the zero-detuning point [values of $k_\parallel$ shown on the left of each lineshape in Fig. 3.8] , we first let ω_G and ω_L be independent fit parameters. We fit the total power dissipated by both oscillators to the extinction spectra, and zero-detuning is identified as the value of $k_\parallel$ for which the difference between ω_G and ω_L is minimized. Having established this value, we then fit the model to the selected measurements once more, but now with the strict equality $\omega_G = \omega_L$. The black lines in Fig. 3.8 are these fits. The model spectra capture the behavior in our measurements reasonably well. In Fig. 3.9 we plot the fitted coupling and loss rates as a function of the experimental waveguide thickness t. The error bars in energy represent a 2σ ($\approx 95\%$) confidence interval on the fits. The error bars in t are due to the uncertainty in the measurements of the waveguide thickness. The curves overlying the data points are guides to the eye.

Figure 3.9 shows that the ratio of the coupling rate Ω to the total loss rate $\gamma_L + \gamma_G$ is maximized at an optimum waveguide thickness $t = 550$ nm. For this value, $\Omega > \gamma_G$ and $\Omega \approx \gamma_L$ (within the error bar). We interpret this condition as the onset of strong coupling. For thinner or thicker waveguides, Ω is less than at least one of the loss rates (mostly γ_L). This corresponds to the weak coupling regime, where energy dissipation is faster than energy exchange between the oscillators. The finding that this system transitions from weak to strong coupling for a limited range of waveguide thickness is a central result of this section. We highlight that the system we investigate (periodic array of metallic nanoparticles coupled to a dielectric slab waveguide) has been actively studied for its ability to modify light propagation and emission in numerous ways [58, 59, 111, 112, 116, 141]. While several groups have presented evidence for strong or weak coupling between LSPRs and guided modes in various configurations, to the best of our knowledge this is the first time that the same plasmonic system is shown to transition between the two regimes.

Intuitively, the transition from weak to strong coupling can be explained in view of how the waveguide thickness modifies the field overlap between the TM_0 guided mode and the LSPR, which is localized near the base of the waveguide. In the thin waveguide limit, the guided mode is weakly confined and a significant fraction of its energy lies outside the slab. The coupling is therefore weak, because the field overlap with the nanoantennas is poor. In the thick waveguide limit, the fundamental guided mode is well confined. However, its electric field amplitude is greatest close to the center of the waveguide, far from the nanoantennas. Therefore, once again the coupling is weak because the field overlap with the nanoantennas is poor. An optimum coupling arises for an intermediate thickness,

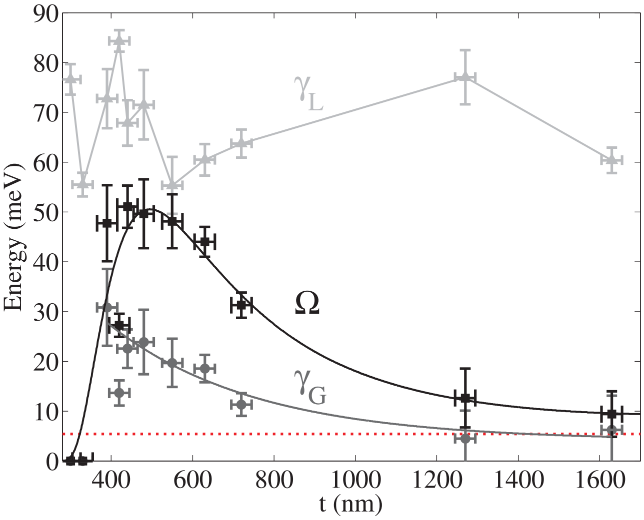

Figure 3.9: Rates extracted from the coupled oscillator model (Equation 3.1) fits to the extinction measurements as shown in Fig. 3.8. Black squares are coupling rates, dark gray circles are loss rates of the TM_0 guided mode, and light gray triangles are loss rates for the localized surface plasmon resonance. Error bars in energy represent a 2σ confidence interval on the fits. Error bars in thickness represent the uncertainty in the measurements of the waveguide thickness. The continuous lines overlplotted with the data points are guides to the eye. The horizontal red dotted line indicates the absorption rate of the molecules embedded in the waveguide at the average zero detuning energy.

where the field overlap is greatest.

We now comment on the dependence of the loss rates on t. γ_L is affected by the local density of optical states at the position of the nanoantennas. As shown by Buchler and co-workers, LSPR radiative losses are affected by a nearby dielectric interface [142]. Here, the proximity of the air-polystyrene interface to the nanoantennas (determined by t) leads to a modified LSPR linewidth. This effect is more clearly visible in the measurements for the thinnest waveguides in Fig. 3.8. Besides this effect, we suspect that slightly different optical qualities (e.g. roughness) of the waveguides could also exert a small influence on our measurements. Regarding γ_G, its non-zero value could be considered surprising based on the fact that a bare guided mode in an unstructured dielectric slab is a bound mode, which implies zero decay rate. As we explain next, γ_G includes both radiation losses due to the structuring of the waveguide, and absorption losses due to the molecules in the waveguide. Radiation losses are enhanced for small t because the actual dye-doped polystyrene waveguide — spatially modulated by the presence of the nanoantennas — deviates more pronouncedly from the flat layer supporting a strictly bound mode. Our data agrees with this intuition, since Fig. 3.9 shows that γ_G decreases as t increases. At large t, γ_G asymptotically approaches the absorption rate of the molecules in the waveguide (5.3 ± 2 meV), which is indicated by the red dotted line in Fig. 3.9. This absorption rate is derived from the complex refractive index of the dye-doped polystyrene layer, $n_p + ik_p$,

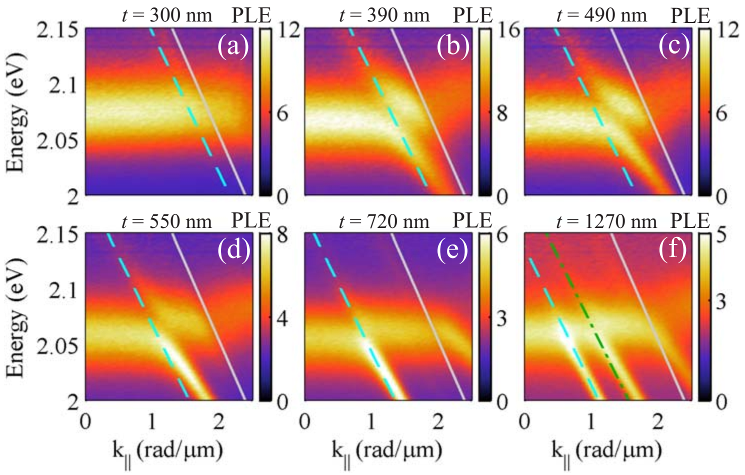

Figure 3.10: Photoluminescence enhancement (PLE) measurements of the structure in Fig. 3.6, for a waveguide thickness (a) t = 300 nm, (b) t = 390 nm, (c) t = 490 nm, (d) t = 550 nm, (e) t = 720 nm, and (f) t = 1270 nm. The gray solid line, identical for all plots, indicates the Rayleigh anomaly with a refractive index of 1.44 (the substrate). The cyan dashed line, shifting towards lower $k_{\|}$ for increasing t, indicates the TM$_0$ guided mode calculated as discussed in the text. The green dash-dotted line in (f) indicates TM$_1$ guided mode.

which we obtained from ellipsometric measurements. Since the ratio n_p/k_p gives the number of optical cycles after which the energy density of a wave decays, the absorption rate at frequency ω is $\gamma = k_p/n_p\omega$. For the calculation in Fig. 3.9, we set $\omega = \overline{\omega}_G$, where the overbar indicates an average for all measured t. The ±2 meV in the value quoted above represents slight variations of ω_G as a function of t, which change the value of k_p due to the frequency dispersion of the refractive index. It should be mentioned that a radiative contribution to γ_G implies, by reciprocity, the possibility of direct radiative excitation of this mode. Therefore, the assumption in our model (Eq. 3.1) that only the LSPR mode is driven directly by the harmonic force holds only approximately for small t, and more faithfully for large t.

Next we present photoluminescence measurements corresponding to the same samples discussed in Fig. 3.7 and Fig. 3.8. The experimental setup is identical to the one in Figure 2.1(b). The samples were pumped by a 2.8 eV continuous wave laser at a fixed angle of incidence 5°. The variable angle emission was collected by a fiber-coupled spectrometer rotating in the far-field, with an angular resolution of 0.2°. The pump irradiance (5 mW/mm^2) was far below the saturation threshold of the molecules. Figure 3.10 shows the photoluminescence enhancement (PLE) in color — varying scales — as a function of the emitted photon energy and $k_{\|}$. The PLE is defined as the ratio of the photoluminescence from the waveguide with and without the nanoantenna array.

The PLE displays an intricate dependence on t that does not directly correlate with that of extinction. For t = 300 nm [Fig. 3.10(a)], the PLE is dominated by the LSPR yielding a maximum 12-fold enhancement. For $t = 390$ nm [Fig. 3.10(b)], the LSPR shows weak signatures of hybridization with the TM_0 guided mode, while the maximum PLE increases to roughly 16-fold. For $t = 490$ nm [Fig. 3.10(c)], the PLE from the weakly hybridized LSPR and TM_0 guided mode are roughly equal, reaching a maximum 12-fold enhancement. For the three thickest waveguides [Figs. 3.10(d,e,f)] the LSPR enhancement is reduced and the PLE is dominated by the TM_0 guided mode. Notice that for the 4 measurements with $t >$ 390 nm [Figs. 3.10(c,d,e,f)], the maximum PLE monotonically decreases. We attribute this reduction in PLE to a higher fraction of dye molecules that are effectively uncoupled from the nanoantenna array. These are the molecules near the top of the waveguide, where the nanoantenna-enhanced fields have significantly decayed.

We now focus on the relative strength of the PLE features and their connection to the properties of the coupled modes. We previously established, based on our analysis of the extinction spectra, that for the thinnest and thickest waveguides the system lies well into the weak coupling regime. In this case, the relevant eigenmodes are the LSPR and the TM_0 guided mode — not their mixture. On either the small or large t weak coupling regime, the extinction displays comparable LSPR lineshapes only marginally affected by the TM_0 guided mode [Figs. 3.7(a,f)]. In contrast, the PLE differs remarkably in these two weak coupling regimes. For small t the greatest PLE contribution is due to the LSPR [Fig. 3.10(a)], while for large t it is due to the TM_0 guided mode [Fig. 3.10(f)]. We attribute this discrepancy between extinction and PLE to the following reason: Extinction is governed by phase differences between incident and scattered fields, while PLE is governed by local field enhancements at the positions of the emitters. Previously, discrepancies between extinction and emission have been attributed to the shift of the near-field with respect to the far-field [104–106, 143]. This effect bears an interesting analogy to the spectrum of a single harmonic oscillator, where the displacement peak (commonly associated with the near-field or emission) is always shifted down in frequency with respect to the dissipated power peak (commonly associated with the far-field or extinction) [139]. However, as shown in the previous section, in the presence of more than one resonance interference can lead to a more complex behavior of the near-field with respect to the far-field. In fact, the far-field extinction can be minimized at the same frequency, wave vector, and polarization, for which the near-field is enhanced [98, 119, 144]. While the relevance of this condition for enhancing light emission has been demonstrated, its relation to the weak-to-strong coupling transition has hitherto not been discussed. Here, by mapping this transition we demonstrate the different regimes in which waveguide-coupled light-emitting optical antenna arrays can operate. On one hand, the results at small t provide a design principle (optimum layer thickness) for generating angle-independent light emission enhancements. On the other hand, the results at large t provide a design principle for generating directional narrowband light emission enhancements, which follow the dispersion of guided mode. For intermediate t, we observe that the spectral window of far-field induced transparency at zero LSPR-guided mode detuning results in only a shallow dip in the PLE spectrum. Thus, it appears that in this region the near-field to far-field contrast is greatest.

We finalize the discussion around the PLE measurements by making a comparison with the measurements in the previous section, where a nanoantenna array stands *on*

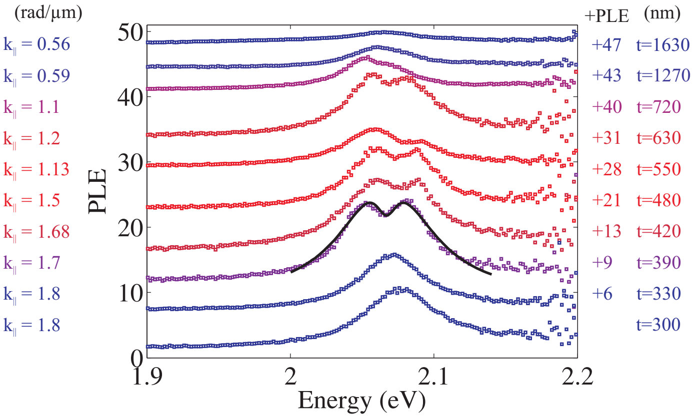

Figure 3.11: Photoluminescence enhancement (PLE) measurements at the values of $k_{\parallel}$ corresponding to zero detuning between the TM_0 mode and the localized surface plasmon resonance in arrays embedded in waveguides of different thickness. The value of $k_{\parallel}$ for each cut is shown at the left of the figure. At the right we indicate the amount by which the PLE data was offset (after the "+" sign) and the thickness t of the waveguide. The black line overplotted with the measurement for $t = 390$ nm is a fit with a coupled oscillator model as described in the text.

rather than *in* a light-emitting waveguide. The greater field overlap between the optical modes enabled by the present configuration allows us to observe enhanced (but still weak) hybridization effects in PLE in the vicinity of the strong coupling regime ($390\text{ nm} \lesssim t \lesssim 630$ nm). We stress the term "weak hybridization" because the dispersion and linewidths of the resonances are clearly modified [Fig. 3.10(b,c,d)], but their energy splitting never exceeds their linewidths. To illustrate this, we present in Fig. 3.11 cuts of the PLE measurements at the value of $k_{\parallel}$ corresponding to zero detuning. The black line in Fig. 3.11 is a fit to the PLE spectrum for a selected waveguide thickness (yielding the most pronounced splitting) with the same model used for the extinction spectra (Eq. 3.1). The fit yields $\Omega = 29 \pm 5$ meV, $\gamma_L = 75 \pm 5$ meV, and $\gamma_G = 17 \pm 7$ meV, which corresponds to weak coupling. We believe that the apparent contradiction in the values of the coupling and loss rates for the same system is due to the inadequacy of the model to describe the PLE data. In particular, in a PLE experiment the system is not subjected to a time-harmonic driving of only one mode, as assumed in Eq. 3.1. Instead, the PLE is associated with a local excitation by the molecules in the waveguide. We also note that the maximum splitting in PLE occurs for $t = 390$ nm rather than $t = 550$ nm, as in extinction. The dependence of the apparent mode splitting on the observable quantity has been highlighted in view of transmission, reflection, and absorption measurements [127, 145]. Here, we introduce a new quantity that needs consideration in emitting systems aimed to operate in the strong coupling regime: the PLE. While an unambiguous determination of the coupling strength is in principle only possible through an eigenmode analysis, experiments always retrieve observables in a driven system. It is therefore important to understand the dependence of these observables on the system's key paramters (e.g., t in our case). Furthermore, we point out that PLE and absorption measurements are not related through reciprocity. While Kirchoff's Law relates absorption and emission at any point in space, an absorptance measurement of our sample largely probes the local field enhancements at the position of the nanoantennas, while PLE measurements probe the local field enhancements at the position of the molecules. As we show next, these two quantities can differ pronouncedly depending on the coupling strength and frequency detuning.

3.3.2 Numerical simulations

In what follows, we study the transition from weak to strong coupling between the LSPR and the TM_0 guided mode using full wave numerical simulations. Firstly, we confirm the features observed in experiments. Secondly, we interpret these features in terms of near-field maps. We have used two distinct methods bench-marked against each other. These are the Fourier modal method (S^4) and finite-element method (COMSOL). The Fourier modal method [146] is a plane wave expansion method to calculate the transmission, reflection and diffraction of layered biperiodic discontinuous structures, i.e. stratified grating systems. We use the free implementation S^4 of Liu and Fan [147] . We find good convergence using just 289 plane waves provided we use parallellogramic truncation, and employ the proper factorization rules of Li [148] appropriate for high-index contrast crossed gratings. We take the same refractive index values used in the dispersion calculations ($n_a = 1.0$, $n_s = 1.58$, and $n_g = 1.44$), and model the aluminum nanoantennas as cylinders of height 150 nm and diameter of 118 nm. The aluminum dielectric constant we use is a polynomial parametrization of measured ellipsometry data.

To model the PLE and visualize the near-fields, we use COMSOL rather than S^4. The Fourier modal method is not optimized for high accuracy in fields according to a point-by-point local measure, while finite element simulations are optimal for real-space insight. As geometry we take the same parameters as in S^4. The computational domain in COMSOL spans the unit cell in the periodicity plane, and extends several wavelengths perpendicularly into to the substrate and superstrate. We apply Bloch-Floquet boundary conditions at the edges of the unit cell and periodic port conditions for the remaining domain walls. The zero-order port on the air side is set for angled plane wave excitation. We have benchmarked the COMSOL simulations against S^4 by comparing the calculated extinction for the $t = 300$ nm structure. We find percent-level agreement for wave vectors below the RA in glass, i.e., in the range of the experiment. However, just beyond the RA in glass COMSOL shows fringes in extinction, which we attribute to spurious reflections off the periodic port boundary condition that occur when a diffracted order is grazing along the port in the substrate or superstrate. These artifacts could be reduced by extending above 7 wavelengths the computational domain in the direction perpendicular to the layers. However, this comes at the expense of an increased computational time compared to S^4. Since we find excellent correspondence for extinction at all energy and momenta below the RA in glass, we conclude that the finite element simulation is fiducial for PLE and near-field maps in this spectral region.

Figures 3.12(a,b,c) show the extinction ($1\text{-}T_0$, for TM-polarized light, incident from air) simulated with S^4 for a set of three waveguide thicknesses: (a) $t = 300$ nm, (b) $t = 420$ nm,

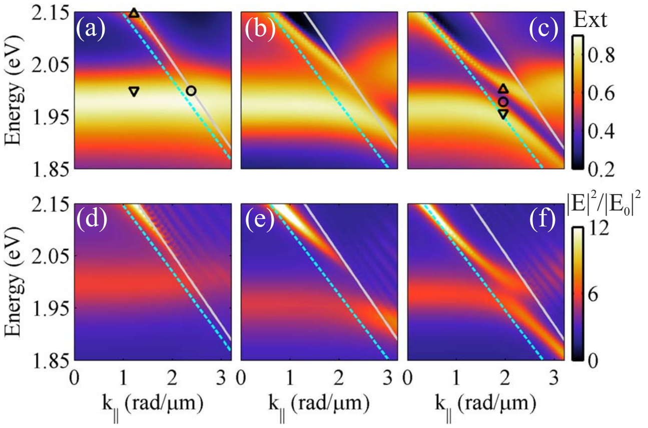

Figure 3.12: Numerical simulations of the light extinction (a,b,c) and electric field intensity enhancement averaged over the waveguide volume (d,e,f) of the structure shown in Fig.3.6 for different waveguide thickness t. For (a,d) t = 300 nm, for (b,e) t = 420 nm, and for (c,f) t = 550 nm. The gray solid line, identical for all plots, indicates the Rayleigh anomaly with a refractive index of 1.44 (the substrate). The cyan dashed line, shifting towards lower $k_{\|}$ for increasing t, indicates the TM$_0$ guided mode calculated as discussed in the text. The open symbols in (a) and (c) indicate the energy-$k_{\|}$ points inspected in 3.13.

and (c) t = 550 nm. The simulations capture the behavior in the measurements (Fig. 3.7) well, both displaying a gradual transition from weak to strong coupling as t increases. Figures 3.12(d,e,f) show the spectrally resolved electric field intensity enhancements for the same three waveguides, simulated with COMSOL. The enhancement is defined as $|E|^2/|E_0|^2$, with E and E_0 the total and incident electric field, respectively, both spatially averaged over the waveguide volume. $|E|^2/|E_0|^2$ is related to the PLE by reciprocity, which states that the local electric field enhancement in the waveguide upon far field plane wave illumination is equivalent to the plane wave strength in the far field due to a localized source. Since our experiment averages over emitter positions and orientations in the entire waveguide, we integrate the total electric field intensity enhancement over the entire unit cell and waveguide thickness (excluding the particle). The resultant quantity can be regarded as the radiative part of the fractional (angle-resolved) local density of optical states. Comparing Fig. 3.12(d) with Fig. 3.10(a) shows that for t = 300 nm, the dominant contribution to the field enhancement in the waveguide comes from the LSPR, and this results in a broadband PLE spectrum with a flat angular dispersion. For t = 550 nm, the $|E|^2/|E_0|^2$ and PLE spectra in Figs. 3.12 (f) and Fig. 3.10(d), respectively, display mixed features of the LSPR and guided mode with a weak anti-crossing between them. For intermediate values of t, the $|E|^2/|E_0|^2$ and PLE spectra show characteristics in between these two cases. Overall, the simulated quantity $|E|^2/|E_0|^2$ qualitatively reproduces the PLE measurements. The agreement is better at lower than at higher energies because absorption by the molecules (not taken into account in the simulations) limits the PLE at higher energies. Indeed, the imaginary part of the refractive index of the dye-doped polystyrene layer, k_p, is roughly a factor of four higher at 2.15 eV than at 2.06 eV (the average eigenfrequency of the TM$_0$ guided mode, ω_G, as obtained from the coupled harmonic oscillator fits). Hence, we expect re-absorption of the enhanced light emission to more seriously hamper the PLE at higher energies as the waveguide thickness increases. This expectation is in agreement with our measurements in Fig. 3.10, where the sharp feature in PLE associated with the guided mode gradually fades for energies above ~ 2.06 eV, and this effect becomes more pronounced as t increases.

We now inspect the near-fields of the structure at selected energies and $k_\parallel$ to illustrate the key differences between weak and strong coupling. In Fig. 3.13 we plot $|E|/|E_0|$ at a plane parallel to the incident electric field and intersecting the nanoantennas at their center. Figures 3.13(a,b,c) correspond to $t = 300$ nm, while Figs. 3.13(d,e,f) correspond to $t = 550$ nm. Figure 3.13(a) is close to zero detuning, as indicated by the open circle in Fig. 3.12(a). Figures 3.13(b,c) represent a large detuning, occurring at $k_\parallel = 1.123$ rad/μm. In Fig. 3.13(b) the photon energy is 2 eV, as indicated by the downwards triangle in Fig. 3.12(a); this corresponds to the approximately bare LSPR. In Fig. 3.13(c) the photon energy is 2.147 eV, as indicated by the upwards triangle in Fig. 3.12(a); this corresponds to the approximately bare TM$_0$ guided mode. The similarity of the fields in Fig. 3.13(a) and Fig. 3.13(b) is due to the weak coupling, which induces a negligible modification to the LSPR even at zero detuning with the guided mode. In contrast to both Figs. 3.13(a,b), the electric field enhancement in Fig. 3.13(c) is stronger and more delocalized. The weaker confinement of the field to the metal explains the narrower resonance linewidth at the conditions of Fig. 3.13(c).

Figures 3.13(d,e,f) illustrate the near-fields for three different energies all at $k_\parallel = 1.95$ rad/μm, which is close to zero detuning for $t = 550$ nm. Strong coupling leads to two new eigenstates, which we label as P$_-$ and P$_+$ in Fig. 3.13(d) and Fig. 3.13(f), respectively. The energy and $k_\parallel$ of P$_-$ and P$_+$ are indicated by the downwards and upwards triangles in Fig. 3.12(c), respectively. The field profiles of P$_-$ and P$_+$ are similar to each other because the strong coupling has hybridized the modes such that their individuality is lost. Here, waveguide-plasmon polaritons are a linear superposition of the bare LSPR and TM$_0$ guided modes with equal weights. If the detuning parameter is varied from $k_\parallel = 1.95$ rad/μm, the field solutions along the upper and lower polariton branches depart from this condition, gradually acquiring a resemblance to one or the other of the bare modes. Finally, an interesting situation occurs in Fig. 3.13(e), the energy and $k_\parallel$ of which is indicated by the circle in Fig. 3.12(c). Here the local fields in the waveguide are still significantly enhanced but the extinction is reduced. This spectral region is particularly attractive for light-emitting plasmonic systems, as it enables simultaneously enhanced local fields at the position of the emitters (and therefore large fluorescence enhancements) and suppressed absorption losses in the metal.

3.3.3 Concluding remarks for this section

In conclusion, we have investigated the dispersive properties in light extinction and emission of an aluminum nanoantenna array coupled to luminescent dielectric slab waveguides. By varying the waveguide thickness we demonstrated a transition from

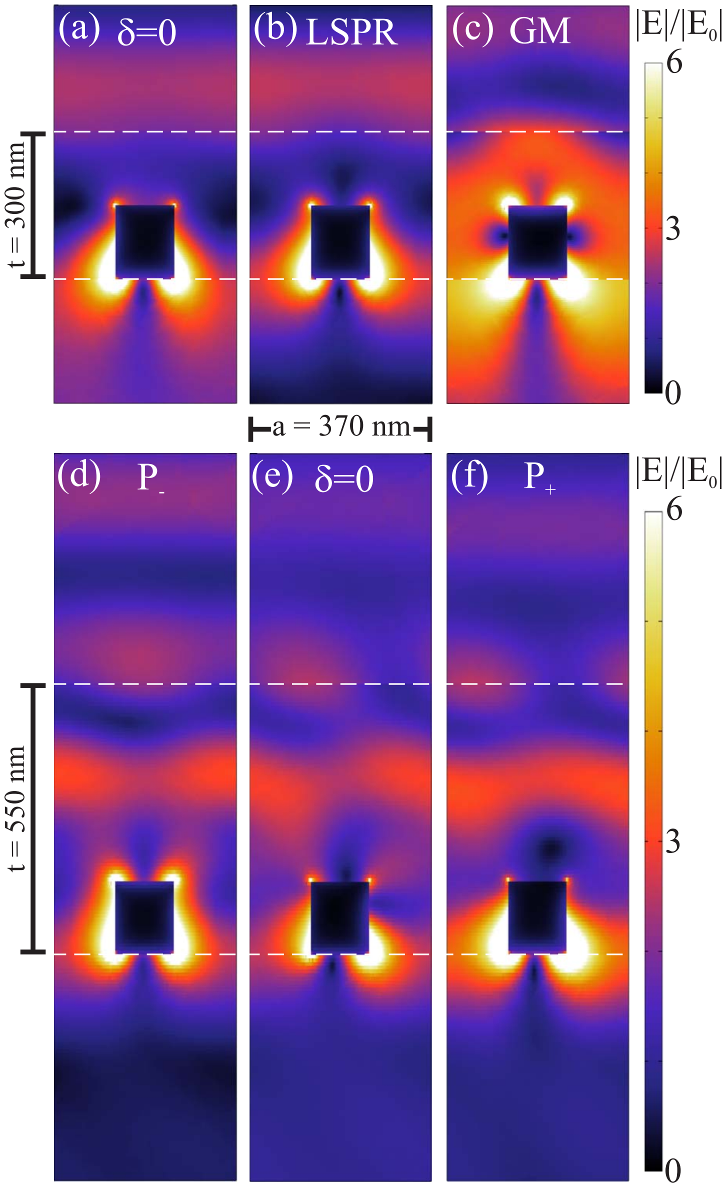

Figure 3.13: Electric field enhancements for the 300 nm waveguide in (a,b,c), and for the 550 nm waveguide in (d,e,f). The energy and $k_{\|}$ corresponding to panels (a,b,c) are indicated Fig. 3.12(a):(a) is at the circle, (b) is at the downwards triangle, and (c) is at the upwards triangle. The energy and $k_{\|}$ corresponding to panels (d,e,f) are indicated in Fig. 3.12(c): (d) is at the downwards triangle, (e) is at the circle, and (f) is at the upwards triangle.

weak to strong coupling between localized surface plasmon resonances (LSPRs) and the fundamental TM_0 guided mode in the slab. Our results provide a design principle for hybrid dielectric-metallic resonators aimed at improving the performance of solid-state light-emitting devices, and shed new light on the near-field to far-field contrast of optical antenna arrays. From a fundamental perspective, we envisage these results to stimulate a quest for a more comprehensive description of hybrid light-matter modes in strongly coupled systems, as we have here shown that their properties (e.g. dispersion relation) depend pronouncedly on the nature of the excitation source.

CHAPTER 4

SURFACE LATTICE RESONANCES COUPLED TO MOLECULAR EXCITONS

We investigate a periodic array of metallic nanorods covered by a polymer layer doped with an organic dye at room temperature. Surface lattice resonances of the array couple strongly to excitons in the dye, and bosonic quasi-particles which we call plasmon-exciton polaritons (PEPs) are formed. At low momenta, PEPs behave as free quasi-particles with an effective mass, lifetime, and composition tunable via the periodicity of the array. By increasing the PEP density through optical pumping, we observe thermalization and cooling of the strongly coupled PEP band in the light emission dispersion diagram. For increased pumping, we observe saturation of the strong coupling and emission in a new weakly coupled band, which again shows signatures of thermalization and cooling. These results are relevant for the design of plasmonic systems aimed at reaching the quantum degeneracy threshold, wherein a single quantum state becomes macroscopically populated.

4.1 Introduction

Surface plasmons are bosons, and by virtue of bosonic stimulation, transition rates into a quantum state are enhanced when the final state occupation exceeds unity. Bosonic stimulation underlies the laser through stimulated emission, and condensation through stimulated scattering. The former has allowed plasmonics to open a new era of nanoscopic coherent light sources [149–153]. In contrast, condensation of surface plasmons into a single quantum state appears to have never been considered. The reasons for this are likely manifold: One one hand, propagating surface plasmon polaritons (SPPs) do not have a cut-off energy — their ground state is at zero frequency, such that thermalization is not number-conserving and condensation does not occur. On the other hand, localized surface plasmon resonances (LSPRs) have a flat dispersion, implying infinite effective mass. Condensation is more easily achieved with low-mass quasi-particles, as it occurs when the mean thermal wavelength $\lambda_T = h/\sqrt{2\pi m k_B T}$ exceeds the interparticle spacing. Additionally, the requirement for the quasi-particles to thermalize poses a challenge for plasmonic systems with typical lifetimes $\lesssim 10$ fs.

We propose that a periodic array of metallic nanoparticles covered by organic molecules in solid-state may overcome the aforementioned limitations. As shown in Chapter 2, such arrays exhibit surface lattice resonances (SLRs) due to the radiative coupling between LSPRs and Rayleigh anomalies (RAs) [23, 74, 76–78, 86]. The narrow linewidth (few meVs [74]) and tunable dispersion of SLRs [80, 81] enables the excitation of low-mass polaritons with relatively long lifetimes. These properties are ideal to achieve strong coupling to excitons in organic molecules. In turn, the relatively fast rovibrational relaxations of organic molecules may provide a thermalizing pathway for the emergent polaritons, allowing them to cool, and eventually condense. While strong coupling between excitons and SPPs has been investigated for propagating modes in flat [123, 128, 154] and perforated [124, 125, 127] metallic layers, as well as for localized modes in nanostructures [126, 155, 156], the strong coupling of SLRs to excitons was only recently explored for the first time [129, 157, 158]. The strongly coupled SLR-exciton quasi-particles we hereby introduce can be considered as low-mass ($\sim 10^{-7}$ times the electron rest mass) analogues of exciton-polaritons in semiconductor microcavities, for which condensation has been observed in several groundbreaking experiments [159–161]. We therefore call them plasmon-exciton polaritons (PEPs).

In this Chapter, we discuss the suitability of PEPs in metallic nanoparticle arrays for quantum condensation. We show that they thermalize, with their effective temperature approaching the lattice temperature when their density is increased through optical pumping. In the present system, we observe a saturation of the strong SLR-exciton coupling before condensation sets in. This leads to a transition from strong to weak coupling, after which we observe thermalization and cooling of the weakly coupled SLR mode. While quantum condensation in a plasmonic system remains unreported at the time of writing, the results in this Chapter lay the foundations for tuning the PEP properties relevant for its possible realization.

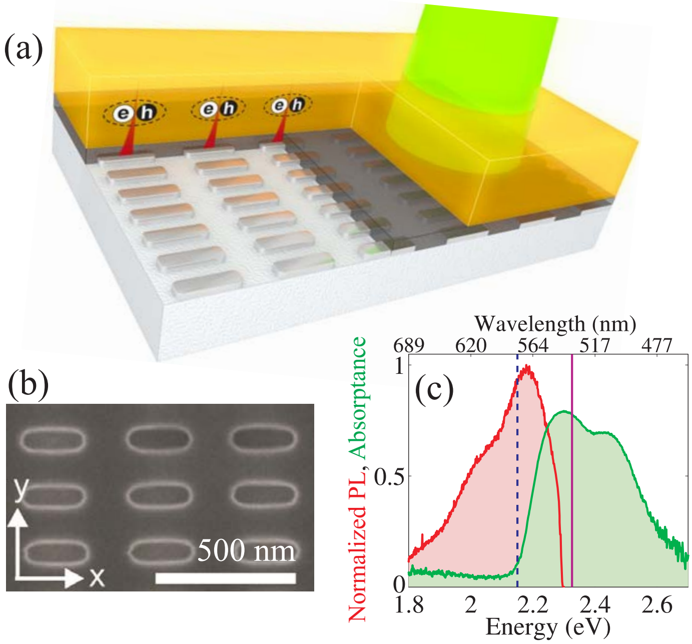

Figure 4.1: (a) A silver nanorod array on an SiO_2 substrate covered by a thin Si_3N_4 layer (gray) and a R6G/PVA layer (orange). An incident laser (green) pumps the R6G exciton reservoir. (b) Scanning electron microscope image of the imprinted resist layer used for the fabrication of the nanorod array. (c) Normalized photoluminescence (red) and absorptance (green) of the R6G layer without the nanorod array. The solid line indicates the pump energy, while the dashed line indicates the emission energy of the saturated ground state at the highest pump power.

4.2 Sample and experimental setup

Figure 4.1 illustrates the sample. A periodic array of silver nanorods was fabricated onto a fused silica substrate by substrate conformal imprint lithography [100]. A scanning electron micrograph of the imprinted resist layer used for the fabrication is shown in Fig. 4.1(b). The rod dimensions are $230 \times 70 \times 20$ nm^3, and the lattice constants are $a_x = 380$ nm and $a_y = 200$ nm. A 20 nm layer of Si_3N_4 on top of the array prevents the silver from oxidizing. A 300 nm layer of polyvinyl alcohol (PVA)—with Rhodamine 6G (R6G) dye molecules for the emission experiments—was spin-coated on top. Figure 4.1(c) shows the absorptance and the normalized emission of the R6G layer.

We measured the variable angle extinction and photoluminescence (PL) of the sample. The experimental setups used are the same as in Figs. 2.1(a,b). The measurements were done using computer-controlled rotation stages with an angular resolution of 0.25°. For the extinction, we measured the transmittance through the array of a collimated (angular spread $< 0.1°$) and linearly polarized light beam from a halogen lamp. The spot size was 500 μm. We define the extinction as $1 - T_0$, with T_0 the zeroth-order transmittance. For

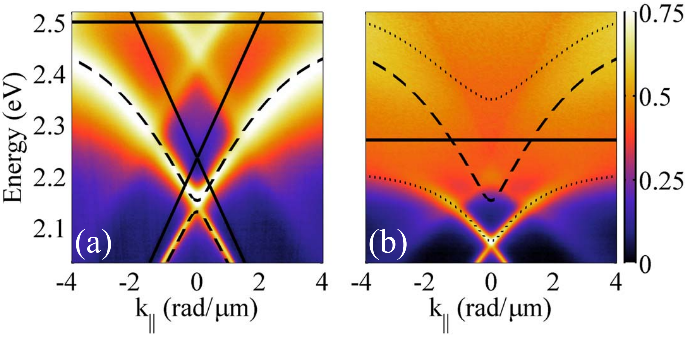

Figure 4.2: Extinction spectra of the nanorod array covered by a polymer layer (a) without and (b) with R6G molecules, both in the same color scale. In (a): the dispersive solid lines indicate the Rayleigh anomalies, while the horizontal solid line indicates the localized surface plasmon resonance. The dashed lines indicate the surface lattice resonances. In (b): The solid line indicates the R6G exciton energy, the dashed line is the upper SLR from (a), and the dotted lines indicate the mixed states (plasmon-exciton polaritons).

the PL measurements, the pump beam was generated by an optical parametric oscillator with peak energy 2.33 eV, ~200 fs pulses, and 80 MHz repetition rate. The pump beam was lightly focused (spot size of 130 μm) and impinged with $k_{\parallel} = 2.05$ rad/μm (10 degrees off the normal). The emitted light was collected by a fiber-coupled spectrometer preceded by a polarization analyzer. The pump power was varied with a neutral density filter, and measured in front of the sample. Both extinction and PL measurements shown in this Chapter correspond to s-polarized light (y-axis, parallel to the short axis of the nanorods) with in-plane momentum $k_{\parallel}\hat{x}$ (parallel to the long axis of the nanorods). All experiments are performed at room temperature (300 K).

4.3 Extinction spectra

Figure 4.2 shows two extinction measurements: In Fig. 4.2(a) the PVA layer has no R6G molecules, while in Fig. 4.2(b) R6G molecules were embedded at 23 weight % with respect to the PVA (R6G number density $\approx 3.6 \cdot 10^8\,\mu\text{m}^{-3}$). The dispersive extinction bands in Fig. 4.2(a) are SLRs associated with the $(\pm1,0)$ diffraction orders. These hybrid modes arise from the coupling between the LSPR (dispersionless solid line) and the $(\pm1,0)$ RAs (dispersive solid lines). We calculate the SLR energies (dashed lines) with the following 3×3 model Hamiltonian,

$$H_{SLR} = \begin{pmatrix} E_L - i\gamma_L & \Omega_{L+} & \Omega_{L-} \\ \Omega_{L+} & E_{R+} - i\gamma_{R+} & \Omega_{\pm} \\ \Omega_{L-} & \Omega_{\pm} & E_{R-} - i\gamma_{R-} \end{pmatrix}, \tag{4.1}$$

where the subscripts "L", "$R+$", and "$R-$" stand for LSPR, (+1,0) RA, and (-1,0) RA, respectively. We set $E_L - i\gamma_L = (2.5 - 0.12i)$ eV for the LSPR, and $\gamma_{R+} = \gamma_{R-} = 10$ meV for the RA losses. The RA dispersion follows from equation 1.7: $E_{R\pm}(k_\parallel) = \frac{\hbar c}{n_{\mathrm{op}}}|k_\parallel + mG_x|$, where m is the order of diffraction, $G_x = \frac{2\pi}{a_x}$ is the x-component of the reciprocal lattice vector, and $n_{\mathrm{op}} = 1.46$ is the refractive index. $E_{R\pm}(k_\parallel)$ are shown as solid dispersive lines in Fig. 4.2(a). Diagonalizing H_{SLR} yields the complex SLR energies, with real parts plotted as dashed lines in Fig. 4.2(a). The coupling constants $\Omega_{L+} = \Omega_{L-} = 184\,\mathrm{meV}$ and $\Omega_\pm = 105\,\mathrm{meV}$ are fitted to reproduce the experimentally observed dispersion. Notice in the measurements that as $|k_\parallel|$ decreases, the upper SLR extinction increases (it becomes bright) while the lower SLR extinction decreases (it becomes dark). This leads to a small gap in the spectrum, near 2.15 eV. The bright/dark character of SLRs is due to an even/odd parity of the electric field at the corresponding energy and momentum of the modes [80]. We refer to Chapter 2 for further details on the spectral and spatial properties of SLRs.

Figure 4.2(b) shows the extinction of the same array but with the R6G molecules embedded in the PVA. The solid line indicates the peak energy of the R6G exciton. The dashed curve is the upper SLR as shown in 4.2(a). The energies of the hybrid modes — plasmon-exciton polaritons (PEP)— are calculated in a similar manner as the SLR energies. The relevant states are now the upper SLR and the R6G exciton. We neglect the lower SLR and the highest state (~LSPR) in what follows because of they do not cross with the exciton resonance. With these assumptions, the Hamiltonian is

$$H_{PEP} = \begin{pmatrix} E_X - i\gamma_X & \Omega_{XS} \\ \Omega_{XS} & E_{SLR} - i\gamma_{SLR} \end{pmatrix}. \tag{4.2}$$

Diagonalizing H_{PEP} yields the PEP energies. For the calculation, we input the complex upper SLR energies obtained from diagonalizing H_{SLR}, we set $E_{\mathrm{X}} - i\gamma_{\mathrm{X}} = (2.27 - 0.1i)\,\mathrm{eV}$ for the exciton, and the mutual SLR-exciton coupling $\Omega_{\mathrm{XS}} = 0.127\,\mathrm{eV}$ is obtained by fitting to the experimental data. The eigenenergies of H_{PEP} (the upper and lower PEP bands) are indicated by the dotted curves in Fig. 4.2(b). At zero SLR-exciton detuning, the upper and lower PEPs are split by 250 meV, which is roughly $2\Omega_{\mathrm{XS}}$ as expected.

We have so far assumed Ω_{XS} to represent an effective coupling constant between the ensembles of molecules and SLRs. However, an inhomogeneously broadened distribution of coupling strengths could be expected based on the various projections of the inhomogeneous SLR fields (decaying out of the periodicity plane) on the different positions and orientations of the molecular dipole moments. Furthermore, the coupling strength is also expected to depend on the photon energy because the field overlap between the ensembles of emitters and SLR modes varies as a function of $k_\parallel$ (and therefore energy). Yet another source of inhomogeneity in the coupling arises from the rovibrational manifold of the molecules. These levels enter into the properties of the collective Dicke state that forms the excitonic part of the 2×2 Hamiltonian H_{PEP}. Despite all these complications, initial theoretical results showed that in the case where H_{PEP} is diagonal (PEPs are the eigenstates), the broadening does not affect the strength of the splitting and the split states are not, in general, inhomogeneously broadened [162][1]. In this case, the simple 2×2 Hamiltonian framework we employ is faithful to the physics and therefore well justified.

---

[1] Actually, Ref. [162] focused on exciton-polaritons in inorganic semiconductor microcavities. However, the form of the Hamiltonian is identical, so the fundamental result holds for PEPs as it holds to exciton-polaritons.

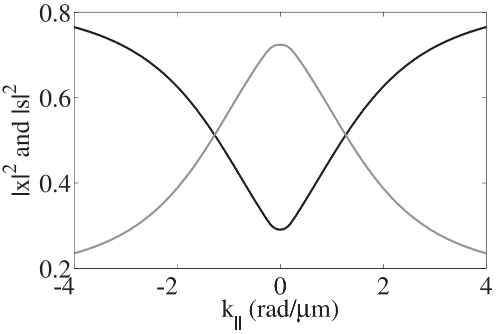

Figure 4.3: Eigenstate fractions for the lower plasmon-exciton polariton band in Fig. 4.2(b) as a function of the incident wave vector. The black line represents the exciton fraction $|x|^2$, and the grey line represents the SLR fraction $|s|^2$.

However, it is important to keep in mind the assumptions in place and ponder upon the limits of their validity. For example, recent theoretical work has shown that the coherence properties of polaritonic peaks depend crucially on the shape of the inhomogeneously broadend distribution (e.g. Gaussian or not), and not only on its width [163]. Such an analysis is beyond the scope of this thesis, and we refer to Refs.[128, 162, 163] for further theoretical considerations.

Focusing once more in the measurements in Fig. 4.2(b), we observe that the extinction of the upper PEP band is smeared out. This is likely due to the increased SLR linewidth at higher energies, which is due to the smaller detuning between the RA and the LSPR (the most lossy of all the eigenstates). Possibly, another mode [see near 2.4 eV at $k_\parallel = 0$ in Fig. 4.2(b)] also has an influence on this linewidth broadening. However, the properties of the upper PEP are mostly irrelevant for what follows. We focus on the lower PEP because the emission from the upper PEP is negligible.

In the low momentum regime, lower PEPs behave as free quasi-particles with a parabolic-like dispersion [158]. Their effective mass is therefore $m_p^* \approx \hbar^2/(\partial^2 E/\partial k_\parallel^2)$. From the measurements in Fig. 4.2(b), we find $m_p^* \approx 2.0 \cdot 10^{-37}$ kg, which makes PEPs $10^{10} - 10^{12}$ times lighter than atoms [164, 165], and ~ 100 times lighter than exciton-polaritons [166]. Our system operates at room temperature (~ 300 k), and the effective polariton temperatures (shown ahead) are on the order of 1000 K. Compared to atomic BECs these temperatures are about $10^8 - 10^{11}$ times higher [164, 165], while compared to GaAs and CdTe exciton-polariton systems they are 100 times higher [166]. Therefore, the mass-to-temperature ratio is similar for all these systems.

The PEP effective mass is determined by the relative weights of the bare states in the admixture. The PEP eigenstates can be expressed as $|\wp(k_\parallel)\rangle = x(k_\parallel)\,|X\rangle + s(k_\parallel)\,|S\rangle$, where $|X\rangle$ and $|S\rangle$ are the exciton and SLR components of the PEPs, respectively. The coefficients in the expansion of light-matter quasi-particles are known as the Hopfield coefficients [166], honoring J.J. Hopfield, who: i) showed that excitons are approximate bosons (a key element enabling Bose condensates in excitonic systems), and ii) introduced the term “polariton” to describe the exciton-photon admixture [167]. Here, the Hopfield coefficients are the components of the eigenvector associated with the PEP’s eigenenergy. The magnitude squared of the Hopfield coefficients yields the eigenstate fractions of the admixture. These fractions depend on $k_\parallel$ because the exciton-SLR detuning depends on $k_\parallel$. At zero SLR-exciton detuning, PEPs are half-SLR half-exciton quasi-particles. For variable $k_\parallel$, Figure 4.3 shows the eigenstate fractions corresponding to the lower PEP in Fig. 4.2(b). The black line is the exciton fraction $|x(k_\parallel)|^2$, while the gray line is the SLR fraction $|s(k_\parallel)|^2$. Conversely, for the upper PEP the black line is $|s(k_\parallel)|^2$ and the gray line is $|x(k_\parallel)|^2$. For the lower PEP at $k_\parallel = 0$, we find $|x(0)|^2 \approx 0.3$ and $|s(0)|^2 \approx 0.7$. Thus, despite the large SLR-exciton detuning (-118 meV), the ground-state exciton fraction is not negligible.

The properties of the PEP ground state, e.g. effective mass and lifetime, can be controlled via the detuning of the bare SLR-exciton states. In Ref. [158] we demonstrated this control by varying the lattice constant a_x of the nanorod array. We measured the extinction spectra of nanorod arrays with $a_x = 350$ nm, $a_x = 360$ nm, and $a_x = 370$ nm, and otherwise identical dimensions to those in Fig. 4.1. For these three additional measurements, the concentration of R6G molecules was increased to 30 weight % with respect to PVA in order to increase the lower PEP ground-state exciton fraction. This is expected to increased the thermalization strength because both vibrational relaxation and inelastic PEP-PEP scattering are expected to increase for increased molecular concentration and/or exciton fraction. Furthermore, since the Rabi frequency scales with the square root of the concentration of molecules, the increased molecular concentration resulted in a larger splittings (180 – 190 meV for the three arrays) and a flatter dispersion. The angular resolution of these measurements was increased to 0.1 degrees to better resolve the dispersive features.

In Fig. 4.4 we analyze the dispersion and linewidth of the lower PEP bands observed in the three samples with increased concentration as discussed above. The lower PEP lineshape measured at each wave-vector was approximated as a Lorentzian resonance, which we fit by a nonlinear least-squares method to the measurements. Figure 4.4(a) shows an example of such fitting at $k_\parallel = 0$ to the lower PEP resonance of the three arrays. The data points are the measurements, and the solid lines are the Lorentzian fits. The fits cover a limited energy range only (same range for all $k_\parallel$, different for each array) to exclude the influence of other resonances at $k_\parallel \neq 0$. We extract the central energy and full width at half maximum (FWHM $= 2\gamma$ with γ the damping) of the fitted Lorentzians as a function of $k_\parallel$, and we plot these in Fig. 4.4(b) and Fig. 4.4(c), respectively. In Figs. 4.4(a)-(c), the blue squares correspond to the $a_x = 350$ nm array, the gray circles to the $a_x = 360$ nm array, and the red triangles to the $a_x = 370$ nm array. The error bars in the central energy and FWHM represent a 2σ (95%) confidence interval in the fits.

The PEP effective masses are retrieved from the dispersion relations in the low momentum regime, as shown in Fig. 4.4(b). The black lines are fits of a quadratic function to the PEP dispersion. The good agreement between the fits and experimental data for the 3 arrays confirms that PEPs behave as free quasi-particles, with an effective mass $m^* = \hbar^2(\partial^2 E/\partial k_\parallel^2)^{-1}$. This yields $m^* = 5.4 \pm 0.3 \times 10^{-37}$ kg for $a_x = 350$ nm, $m^* = 3.1 \pm 0.1 \times 10^{-37}$ kg for $a_x = 360$ nm, and $m^* = 2.6 \pm 0.1 \times 10^{-37}$ kg for $a_x = 370$ nm. The uncertainty in the mass represents a 2σ (95%) confidence interval in the quadratic fits to the dispersion relation in the plotted range. We attribute the observed changes in effective mass to the

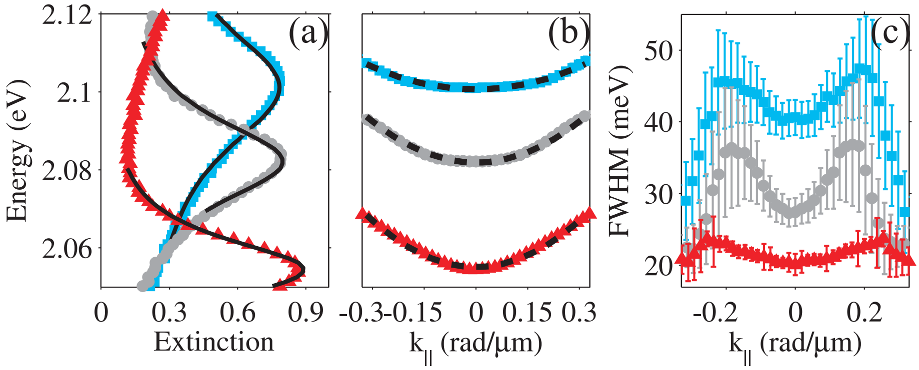

Figure 4.4: (a) Extinction spectra at $k_\parallel = 0$, (b) dispersion relations, and (c) full width at half maximum (FWHM), of the lower plasmon-exciton polariton in nanorod arrays with varying lattice constant a_x. The blue squares, grey circles, and red triangles in all figures correspond to the arrays with $a_x = 350$ nm, $a_x = 360$ nm, and $a_x = 370$ nm, respectively. The error bars in (b) and (c) [smaller than the data points in (b)] represent a 2σ confidence interval in fitting the measured resonance with a Lorentzian lineshape at each $k_\parallel$. An example of such fitting procedure is shown in (a), where the fitted Lorentzians are shown as solid black lines. The dashed black lines in (b) are quadratic fits used to retrieve the plasmon-exciton polariton effective mass.

variable composition of PEPs. As the bare SLR ground state is increasingly detuned from the bare exciton state, the lower PEP effective mass is reduced. Indeed, in Fig. 4.4(b) it is shown that for increasing a_x the curvature of the lower PEP band increases, implying a reduced effective mass. In Ref. [158] it is shown that in parallel to this trend, the lower PEP ground-state exciton fraction decreases from $|x(0)| = 0.47$ for $a_x = 350$ nm to $|x(0)| = 0.37$ for $a_x = 370$ nm.

Next, we analyze in in Fig. 4.4(c) the FWHM of the PEPs. It is clear that both a_x and $k_\parallel$ affect the FWHM. The dependence of the PEP FWHM on a_x can be traced to the dependence of the SLR FWHM on the LSPR-RA detuning, as discussed in Chapter 2. For increasing a_x and otherwise fixed dimensions, the LSPR-RA detuning at $k_\parallel = 0$ increases. Within the framework of the Hamiltonian model employed in this section (i.e. H_{SLR}), this means that the LSPR fraction at $k_\parallel = 0$ is reduced. Since the LSPR is the most lossy amongst the underlying SLR constituents, a reduced LSPR fraction implies a reduced SLR FWHM. In turn, a reduced SLR FWHM grants the PEP it composes a reduced FWHM. The PEP FWHM has a secondary dependence on $k_\parallel$, which is also based on the properties of the underlying SLR. For small $k_\parallel$, the mutual coupling between upper and lower SLRs modifies their linewidth and dispersion [80]. Standing waves are formed in the upper SLR band, and the balance between radiative and non-radiative losses varies pronouncedly in a narrow $k_\parallel$ range [96]. This is origin of the $k_\parallel$ -dependent FWHM of PEPs observed in Fig. 4.4(c). While Ohmic losses set a lower limit on the FWHM, we envisage that by fine tuning the geometry of the nanorods and the periodicity of the array, radiative losses can be minimized even further to yield PEPs with narrower linewidths and non-vanishing excitonic content.

The results in this section demonstrate the opportunities and challenges that plasmon-exciton polaritons may face in their way towards quantum condensation. For increasingly negative SLR-exciton detuning (larger lattice constant in the configuration here used), the effective PEP mass is reduced and this is beneficial for increasing the critical temperature required for condensation. However, it should be noted that the ground-state of such an admixture has a reduced plasmonic and excitonic content. Another important parameter is the FWHM of the resonance, which also decreases for increasingly negative SLR-exciton detuning as shown in Fig. 4.4(c). The lifetime of the excitations (the inverse of the FWHM if inhomogeneous broadening is neglected) is a key element to consider in the pursuit of a quantum condensate, as it will influence the dynamics (e.g. equilibrium vs non-equilibrium) of the system. In summary, we reckon the simultaneous decrease in linewidth and plasmonic content as a manifestation of the well-known trade-off between localization and losses in plasmonic systems.

We finalize this section with a few words of caution regarding the theoretical models we have used to interpret our data. Many of our observations have been qualitatively explained through simple Hamiltonian models. For example, the linewidth and dispersion of the mixed states (PEPs) are roughly the average of the bare states (SLR and exciton) weighted by the factors $|x(k_\parallel)|^2$ and $|s(k_\parallel)|^2$. However, our interpretation of these quantities as eigenstate fractions relies on a closure relation ($|x|^2+|s|^2=1$), which does not hold in general for a non-Hermitian Hamiltonian. We have departed from Hermiticity by incorporating complex energies (lossy states), such that $|x|^2+|s|^2\neq 1$. Thus, strictly speaking, the meaning of $|x|^2$ and $|s|^2$ as eigenstate fractions is lost due to the incompleteness of the spectrum. Nevertheless, when the real parts of the eigenenergies are much greater than the corresponding imaginary parts, $|x|^2+|s|^2\approx 1$ and a qualitative interpretation still holds. This can be verified in Figure 4.3, and Ref. [158], where non-Hermitian Hamiltonians were used and $|x|^2+|s|^2\approx 1$. For a more rigorous description of these effects — including generalized closure relations and the phenomenon of self-orthogonality in non-Hermitian Hamiltonians —,we refer to Moiseyev [168].

4.4 Emission spectra

In Fig. 4.5(a) we present a series of emission measurements obtained by increasingly pumping the sample (as described in section 4.2) from the measurements in Fig. 4.2(b). Figure 4.5(a) shows the forward ($k_\parallel=0$) emission spectrum as a function of the pump irradiance. The peak at ~2.08 eV, which dominates the spectrum below a critical irradiance of $P_c\approx 60\,\mathrm{W/cm}^2$, is the emission from the lower PEP. The shoulder at 2.065 eV is attributed to the lower SLR, which is dark at $k_\parallel=0$ but appears in the spectrum due to the finite angular resolution of the experiment. As pumping increases, the lower PEP peak blue-shifts and broadens. Above P_c a new peak emerges at ~ 2.15 eV, and at ~ $2P_c$ its emission exceeds the lower PEP emission. As we explain next, we attribute the shift of the coupled states towards the uncoupled states to saturation of the exciton-SLR coupling with increasing density of excitations. Saturation phenomena have been observed in different plasmonic-excitonic systems as a diminished normal mode splitting in the frequency-domain, and as a reduced Rabi frequency in the time-domain [169, 170].

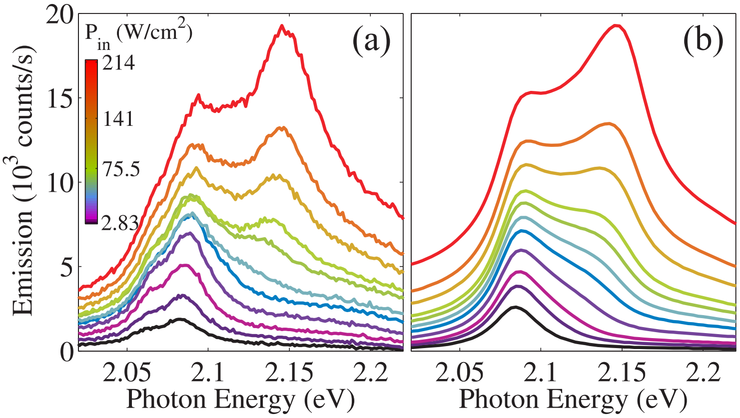

Figure 4.5: Light emission of the sample in Fig. 4.1 collected at $k_{\parallel} = 0$, (a) for different experimental input power densities encoded in color, and (b) predictions by a model based on local saturation of the SLR-exciton coupling strength (see text for details).

Saturation of the exciton-SLR coupling alone leads to a smooth blue-shift of the emission peak from the PEP energy towards the bare SLR energy. Instead, we observe the coexistence of two emission bands with relative amplitudes depending on the pump power. In the following, we explain this phenomenon through a phenomenological model describing how the spatiotemporal profile of the excitation density influences the eigenstates of the Hamiltonian. We focus on the emission from the lower eigenstate of the 2×2 Hamiltonian H_{PEP} (equation 4.2), from which the PEP dispersion in Fig. 4.2(b) was calculated.

We start by departing from the assumption that the exciton-SLR coupling Ω_{XS} is a constant. Instead, based on earlier works on exciton-polariton [171, 172], we consider that Ω_{XS} saturates as a function of the excitation density n as follows:

$$\Omega_{\mathrm{XS}}(n) = \frac{\Omega_{\mathrm{XS},0}}{\sqrt{1 + n/n_{\mathrm{sat}}}}. \tag{4.3}$$

Here, $\Omega_{\mathrm{XS},0}$ is the unsaturated coupling strength, and n_{sat} is the saturation density. Furthermore, we consider that the density of excitations, n, varies spatially and temporally. Since the excitation spot ($\sim 130\mu$) is much greater than the propagation length of the PEPs (on the order of 10μm [79, 85]), the spatial variation of the excitation density follows the profile of the pump beam, which is gaussian. In time, the excitations decay much faster than the repetition rate of the laser, which gives a pulse every 12.5 ns. Therefore, the spatiotemporal profile of the excitations is

$$n(r,t) \propto P_{\max} e^{-r^2/r_0^2 - t/t_0}, \tag{4.4}$$

where $r = \sqrt{x^2 + y^2}$ is the distance from the beam center in the plane of the array, and r_0 and t_0 are the spot size and excitation lifetime. Here we have assumed a constant density of excitations along the optical axis. Then, since the PEP lineshape is approximately Lorentzian (see previous section), we model the emission spectrum from each point in space with a Lorentzian function centered around the local PEP energy. Furthermore, based on the input power dependence of the total emission spectrum (Fig. 4.6), we deduced the emission intensity is proportional to $n(r,t)+\alpha\sqrt{n(r,t)}$, where the sublinear square-root term is likely due to bimolecular quenching [173]. Therefore, the output power is

$$P_{\text{out}}(E,r,t)\propto\frac{\big(n(r,t)+\alpha\sqrt{n(r,t)}\big)\gamma}{(E-E_{PEP}[n(r,t)])^2+\gamma^2},\tag{4.5}$$

where γ is the emission linewidth, which in principle could also depend on the local density of PEPs. As the change of γ when going from the fully coupled PEP to the bare SLR is expected to be small, it is chosen constant here for simplicity. This constant value is obtained from the experiments at low pumping. The total emission spectrum is then given by the integral of Eq. 4.5 over space and time:

$$I_{\text{out}}(E)\propto 2\pi\int_0^\infty\int_0^\infty rP_{\text{out}}(E,r,t)\,\mathrm{d}t\,\mathrm{d}r\,,\tag{4.6}$$

where we have exploited the radial symmetry of the integrand. Note that the final result does not depend on r_0 or t_0 apart from a global scaling. In the following, we do not fix the proportionality factor between input power and $n(r,t)$, but instead set n_{sat} and α in units where $n(r,t)$ is given in W/cm^2, and set P_{max} to the total input irradiance. Finally, we add the contribution from the molecules which are a priori uncoupled to the SLR mode. The uncoupled molecules decay directly into free-space photons, and their spectrum therefore follows the bare R6G emission lineshape.

The results from the above model are presented in Fig. 4.5(b). The parameter values used for the calculations are $\gamma = 16\,\text{meV}$, $n_{\text{sat}} = 5\,\text{W/cm}^2$, $\alpha = 25\,(\text{W/cm}^2)^{1/2}$, $E_{SLR} = 2.162\,\text{eV}$, and $\Omega_{\text{XS},0} = 0.123\,\text{eV}$. A good agreement between experiments and theory is observed. We note that E_{SLR} and Ω_{XS} are slightly different from the values used to reproduce the extinction measurements, due to the differences between emission and extinction described in earlier chapters.

At zero detuning, strong coupling occurs when the energy exchange rate Ω_{XS} is larger than the decay rates γ_X and γ_S of the exciton and SLR, respectively. Although a formal distinction is less clear for non-zero detuning, as in the present case, the two extreme cases can be readily identified: Small n leads to strong coupling ($\Omega_{XS}\gg\gamma_X,\gamma_S$), while $n\gg n_{\text{sat}}$ leads to weak coupling ($\Omega_{XS}\ll\gamma_X,\gamma_S$). From the model, it follows that the low-energy emission peak stems from regions with low density where the emission from the strongly coupled PEPs dominates. For increased pumping the lower PEP emission saturates, and a new peak emerges at higher energies. The high-energy peak stems from regions with high density where the emission from the weakly coupled SLR dominates. Notice that both peaks blue-shift towards the bare SLR state, and the high-energy peak closely approaches it. The intermediate spatial regions form a continuum of populations with different coupling strengths that are not resolved as isolated peaks. This continuum effectively broadens the peaks associated with the two extrema.

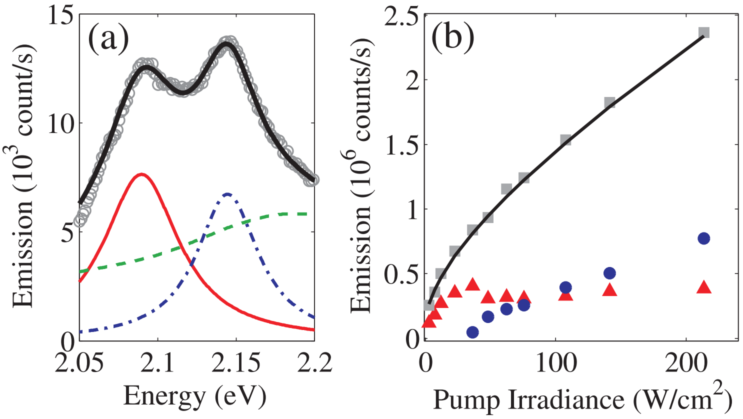

Figure 4.6: (a) The grey circles are the measured light emission intensity of the sample in Fig. 4.1 at $k_\parallel = 0$ for $P = 141$ W/cm^2. This is fitted (black solid line) with the sum of two Lorentzians (red solid line and blue dash-dotted line) and the background R6G emission (green dashed line). (b) Emission for the different states as a function of the pump irradiance. The red triangles correspond to the lower plasmon-exciton polariton which saturates. The blue circles correspond to the upper band approaching the bare SLR state. The grey squares are the total output power obtained by combining the previous two and the background R6G emission. The black line is a fit to the experimental data, with linear and square root terms as described in the text.

Next, we quantify the relative contributions from the strongly coupled PEPs and weakly coupled SLRs at $k_\parallel = 0$ for different pump powers. The emission spectrum at $k_\parallel = 0$ can be well fitted with the sum of two Lorentzians and the background R6G emission. The two Lorentzian peaks correspond to the strongly and weakly coupled extrema discussed above. Their lineshapes are thus not expected to be purely Lorentzian, but include inhomogeneous broadening. For simplicity, we use Lorentzian lineshapes in the following. The background R6G emission stems from the fraction of excited molecules that decay directly into free-space photons. In other words, the β factor (as known in the laser literature), which quantifies the spontaneous emission fraction into the cavity mode, is less than unity. Figure 4.6(a) shows one such fit for the case $P = 141$ W/cm^2. Therein, the grey circles are the measured intensity, while the black solid line is obtained by summing the two Lorentzians (red solid line and blue dash-dotted line) and the background R6G emission (green dashed line). The good agreement between the data and the fit partially validates the choice of pure Lorentzians. Similar fits were performed for the different pump powers. From the area under the fitted Lorentzians, we calculated the emitted power by each of the bands as a function of the pump irradiance. This is shown in Fig. 4.6(b), where the blue circles correspond to the high-energy (SLR-like) peak, the red triangles correspond to the low-energy (PEP-like) peak, and the grey squares are the total emitted power. The black solid line is a fit of the total emitted intensity I_{out} to a function of the form $I_{out} \propto I_{in} + \alpha\sqrt{I_{in}}$, with I_{in} the pump irradiance and α a fit parameter. The good agreement between the fit and the data validates the form of the Lorentzian pre-factor used in equation 4.5 to

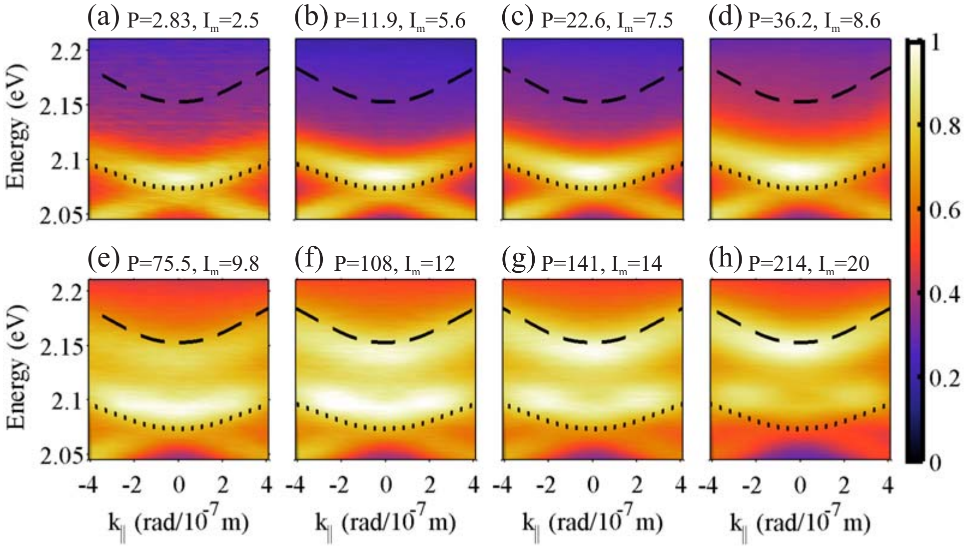

Figure 4.7: (a-h) Variable angle light emission of the sample in Fig. 4.1 for increasing pump irradiance P (in units of W/cm^2). The colorbar pertains to all spectra, with the maximum intensity I_{m} indicated in 10^3 counts/s. The dashed and dotted lines are the SLR and PEP energies.

model the intensity-dependent density of excitations n, i.e. $n(r,t) + \alpha\sqrt{n(r,t)}$. The weakly coupled SLR peak (blue triangles in Fig. 4.6) displays a clear threshold as function of the pump power. According to our model, this threshold corresponds to the emergence of a saturated population from the background emission. The emergence of this peak is not only dictated by the pump irradiance and the saturation density n_{sat}, but also by the β factor of the mode. The latter is embedded in our model via the relative amplitude of the background R6G emission with respect to the two Lorentzian peaks.

We now study the dispersion of the observed bands through their angle-dependent emission intensity, shown in Figures 4.7(a)-(h) for several pump powers. These are the same measurements as in Fig. 4.5, but now for variable angles. Even for the lowest pumping, we find that the lower PEP band is slightly blue-shifted compared to the extinction measurements. It is also flatter, corresponding to a slightly higher effective mass of $\approx 2.6 \cdot 10^{-37}$kg (extracted from the curvature of the band at $k_\parallel = 0$). We attribute these differences between extinction and emission spectra to the shift of the near-field with respect to the far-field. Extinction stems from the interference between direct and scattered radiation, while emission does not contain a direct part. This leads to a shift of the peak emission energy, which can also affect the extracted effective mass if it is angle-dependent.

Next, we discuss the thermalization behavior. Condensation as a thermodynamic phase transition requires the system to approach thermal equilibrium, which constrains the ratio of thermalization to decay time. For inorganic exciton-polaritons, both of these times can be $1-10$ ps, and consequently both equilibrium and non-equlibrium condensation have been observed [160, 161, 166, 174–178]. For the present system, we estimate a PEP lifetime of at least $\sim 17\,\text{fs}$ from the inverse linewidth of the associated emission peak. However, the lifetime could be much longer if the linewidth is broadened inhomogeneously. Vibrational relaxation of R6G, and thus PEP-phonon scattering, occurs on a scale of $\sim 100\,\text{fs}$ [179], while PEP-PEP scattering rates are currently unknown. Therefore, equilibrium dynamics seem unlikely in our case. As we show next, we nevertheless observe thermalization and cooling for increased pumping, possibly due to more efficient PEP-PEP scattering, increased phonon emission at high density, or a longer polariton lifetime. The latter possibility appears particularly relevant in light of recent results by Schwartz *et. al.* [180], who have shown that the lower polariton is intrinsically long-lived. The system studied in Ref. [180] comprises organic molecules at room-temperature strongly coupled to a photonic mode between two metal mirrors, thereby making it much closer conceptually to our system than the low-temperature inorganic systems traditionally used in exciton-polariton research.

Figures 4.7(a)-(d) display a greater emission from the strongly coupled band at low pumping, while Figs. 4.7(e)-(h) display a greater emission from the weakly coupled band at high pumping. We study this in detail by analyzing the occupation n_{oc} as a function of the emitted photon energy, shown in Fig. 4.8(a) for the strongly coupled band and in Fig. 4.8(c) for the weakly coupled band. The occupation is extracted from the emission intensity $I(k_\parallel)$ along the corresponding band, integrated over a fixed bandwidth of 40 meV. We take into account that PEPs are composite quasi-particles and only their photonic component leaks out of the open system. Thus, as in exciton-polariton systems [172, 181], we correct for the SLR fraction $|s(k_\parallel)|^2$, giving $n_{oc} \propto I(k_\parallel)/|s(k_\parallel)|^2$. Here we have assumed that SLRs mainly decay radiatively due to their large Rayleigh anomaly fraction and the predominantly radiative decay of LSPRs. The gray lines in Fig. 4.8(a) and Fig. 4.8(c) are fits of the occupation to a Maxwell-Boltzmann distribution $n_{oc} \propto \exp[(-E-E_0)/k_B \mathrm{T_{eff}}]$, from which we extract the effective temperature $\mathrm{T_{eff}}$. This is shown as a function of the pump irradiance in Fig. 4.8(b) and Fig. 4.8(d) for the strongly and weakly coupled band, respectively. The error bars represent a 2σ ($\approx 95\%$) confidence interval, and stem mostly from a small asymmetry of n_{oc} for positive and negative $k_\parallel$. This asymmetry is possibly due to angle-dependent variations in collection efficiency and intensity fluctuations during the measurements.

The effective temperature of the lower PEPs displays an initial decrease, but remains warmer than the lattice. This observation, which is similar to early works on exciton-polariton condensates [159, 161], indicates that the system approaches but does not fully reach thermal equilibrium with the heat bath (the molecule phonons). In addition, we observe in Fig. 4.8(b) that for increased pumping the ground state (E_0) occupation increases slightly above the Maxwell-Boltzmann fit. This could be an indication that the bosonic statistics of the PEPs are becoming relevant, implying that condensation is being approached, although not reached. Consequently, the ground state occupation remains lower than in exciton-polariton condensates [160, 161]. As the power increases and saturation is approached, $\mathrm{T_{eff}}$ increases again, although the experimental uncertainty from the fits also increases. This increased uncertainty implies a stronger deviation of the n_{oc} from a thermal distribution near the strong-to-weak coupling transition. Therefore, while

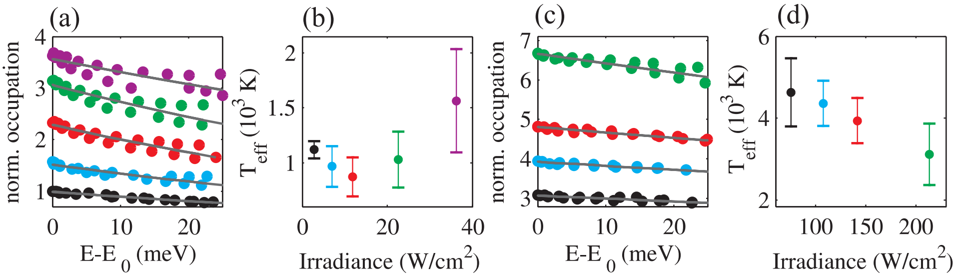

Figure 4.8: Normalized occupation of the (a) lower (PEP) band below saturation and (b) upper (SLR) band above saturation. Data points of different colors correspond to measurements at different pump powers. The two groups of points for each power correspond to the occupation for $\pm k_{\parallel}$, i.e. the data is slightly asymmetric. The solid gray lines are Maxwell-Boltzmann fits. The color corresponding to each pump power can be inferred from (b) and (d), which show effective temperatures retrieved from the fits in (a) and (c), respectively.

cooling of PEPs is observed, saturation of the SLR-exciton coupling sets in before condensation is reached, and the new band with weaker coupling emerges and blue-shifts towards the bare SLR state. The effective temperatures in this new band [Fig. 4.8(d)] are higher than in the PEP band. Nevertheless, T_{eff} decreases monotonically as pumping increases. This cooling implies that condensation of bare SLRs could be within reach, analogous to the condensation of cavity photons observed by Klaers *et al.* in a dye-filled optical microcavity [182]. In our samples, further pumping was not possible because the molecules bleached.

4.5 Experimental details

In this section we provide further experimental details that may not be necessary to understand the physics, but may have technical value for others wishing to reproduce our results.

4.5.1 Excited molecule density

Here we estimate the fraction of excited R6G molecules by each laser pulse. The pump laser has a photon energy $E_{\text{pump}} \approx 2.33\,\text{eV}$ and a repetition rate $f = 80\,\text{MHz}$, corresponding to a pulse every 12.5 ns. As the longest lifetime of any excitation in the system (in the ps range) is orders of magnitude shorter than the repetition rate, all excitations decay before the next pulse arrives. For the highest average pump irradiance, $P_{\max} = 214\,\text{W/cm}^2$, the 2D photon density per pump pulse is $\rho_{\text{pump}} = P_{\max}/(f E_{\text{pump}}) \approx 7.25 \cdot 10^4\,\mu\text{m}^{-2}$.

The R6G molecules are embedded in the PVA layer at 23 weight %, corresponding to a density of $0.29\,\text{g/cm}^3$, and a number density of $n_{\text{R6G}} \approx 3.6 \cdot 10^8\,\mu\text{m}^{-3}$. The thickness of the layer is $t_{\text{PVA}} = 300\,\text{nm}$, giving a 2D density of $n_{\text{R6G}} t_{\text{PVA}} \approx 1.1 \cdot 10^8\,\mu\text{m}^{-2}$. The absorption cross section of R6G at E_{pump} and at high concentration is on the order of

$\sigma \approx 2 \cdot 10^{-8}\,\mu\text{m}^2$ [183]. This gives an optical density of $OD = \sigma n_{\text{R6G}} t_{\text{PVA}} \approx 2.2$, and a corresponding absorptance of $A = 1 - \exp(-OD) \approx 0.89$. This agrees reasonably well with the measured absorptance of the bare layer [Figure 4.1(c)]. Thus, almost all photons of the incoming pulse are absorbed. The 2D excitation density is then $A\rho_{\text{pump}} \approx 6.5 \cdot 10^4\,\mu\text{m}^{-2}$, which means that the fraction of excited molecules is about $5.9 \cdot 10^{-4}$.

4.5.2 Time scales and experimental limitations

An important experimental parameter in the PL measurements is the time duration of the pump pulse (~ 200 fs). The pulse duration was roughly a factor of 2 higher than the expected vibrational relaxation time scale of the organic molecules, which poses a challenge for an equilibrium state to be established. The unlikelihood of an equilibrium state with a true temperature in the usual sense is already manifest in the high effective temperatures reported in Fig 4.8. The fact that these effective temperatures are much higher than the lattice temperature indicates that while plasmon-exciton polaritons may achieve local self-equilibrium amongst themselves through inelastic scattering, they remain out of equilibrium with their surroundings. However, the relatively short pulse duration was chosen for a reason: A shorter pulse yields higher peak powers compared to continuous-wave or long-pulse lasers with equal average power. The high peak power leads to a high density of excitations, while the removal of the pump power shortly after (at the end of the pulse) assists in heat dissipation. Thus, greater “instantaneous” densities — which are essential for the main results of this Chapter— can be created before reaching the damage threshold of the molecules. In fact, this damage threshold (an irreversible photobleaching) prevented us from using higher pump powers in the PL experiments. As the system dynamics depend sensitively on the excitation source, we expect future experiments using different sources to reveal novel phenomena, and to further clarify the influence of the pulse duration on the thermalization dynamics.

4.6 Conclusions

In conclusion, we have presented experimental indications of thermalization and cooling of quasi-particles in an array of silver nanoparticles covered by organic molecules. This array supports surface lattice resonances, which form plasmon-exciton polaritons (PEPs) through strong coupling to molecular excitons. In view of the low PEP mass, which is furthermore tunable via the surface lattice resonance dispersion, we believe that plasmonics holds great promise for solid-state studies of macroscopic quantum many-body physics at and above room-temperature. While the short lifetimes typically characterizing surface plasmons make thermodynamic equilibrium challenging, we envisage these results to open a new avenue for studying non-equilibrium quantum dynamics. We also point out that while the results in this Chapter were under review, SLR lasing was demonstrated by Zhou and co-workers [91], and shortly after, organic polariton condensates in dielectric microcavities were demonstrated [184, 185].

CHAPTER 5

LOCALIZED SURFACE PLASMONS COUPLED TO DIFFRACTED ORDERS IN MAGNETOELECTRIC NANOPYRAMID ARRAYS: FORWARD-BACKWARD LIGHT EMISSION SYMMETRY BREAKING

We propose aluminum nanopyramids (ANPs) as magnetoelectric optical antennas to tailor the forward versus backward luminescence spectrum. We present light extinction and emission experiments for an ANP array wherein magnetoelectric localized resonances couple to in-plane diffracted orders. This coupling leads to spectrally sharp collective resonances. Luminescent molecules drive both localized and collective resonances, and we experimentally demonstrate an unconventional forward versus backward light emission spectrum. Full-wave simulations show that localized and delocalized magnetic surface waves, with an excitation strength depending on the plane wave direction, direct the forward versus backward emitted intensity.

5.1 Introduction

In a celebrated paper, Pendry and co-workers laid the theoretical foundations for enhancing magnetism at optical frequencies with metals [186]. When subwavelength features are imprinted on metals, magnetism emerges from the coupled capacitive and inductive response to the incident radiation. This principle has guided great advances in the field of metamaterials: artificial structures possessing properties absent in natural materials. Initial interest in metamaterials focused on their effective medium properties (homogenization) [187], aimed at the realization of non-trivial phenomena such as negative refraction [188–190], subwavelength resolution [191–193], and cloaking [135, 194, 195]. Recently, interest has extended towards understanding the electric, magnetic, and magnetoelectric response of the constituent resonators [196–202]. Such understanding has important connections to the field of optical antennas, where the constituent metamaterial (leaky) resonators are employed to interface plane waves with near-field sources [38]. Thus, for metamaterials as for optical antennas, nanostructured resonators with an enhanced magnetic response are pivotal for achieving full control of electromagnetic waves. Among the many possibilities enabled by this control, an effect that has attracted increasing interest is the modification of forward and backward scattering in anomalous ways. This occurs for dielectric nanoparticles when their electric and magnetic moments are comparable in magnitude, at the so-called Kerker condition [60, 203–206]. Unbalanced forward and backward scattering from passive structures has inspired several studies revisiting fundamental concepts in electromagnetism (e.g. the optical theorem [207]), and predicting intriguing effects such as cloaked sensors [135] and nanoscale control of electromagnetic hotspots [117]. However, the possibility to unbalance the forward to backward emission ratio from planar near-field sources (e.g. thin luminescent layers) remains unexplored. Interestingly, since planar structures are nearly always designed to emit into the “forward” rather than backward direction (the latter resulting in losses), controlling this directional emission represents an important functionality that magnetoelectric optical antennas may address.

In this Chapter we demonstrate strong spectral modifications in the forward versus backward emission from a thin polymer layer doped with luminescent molecules coupled to magnetoelectric metallic nanostructures. We investigate aluminum nanopyramids (ANPs) sustaining localized and collective resonances in spectral overlap with the luminescent molecules. Collective resonances arise in periodic arrays of metallic nanoparticles when Rayleigh anomalies (RAs) couple to localized surface plasmons. This coupling leads to hybrid plasmonic-photonic resonances known as surface lattice resonances, the physics of which we discussed in Chapter 2. Previously, we showed that SLRs (Chapter 2) and waveguide-plasmon polaritons (Chapter 3) in arrays of shallow antennas with a dominant electric dipole moment are sufficient for achieving light emission directivity gains within a certain half-space of the array. In contrast, unbalancing the emitted intensity into the two half-spaces surrounding the array requires a structural asymmetry and/or the interference of multiple electromagnetic moments. Here we present experiments for a lattice of asymmetric resonators with enhanced magnetic, magnetoelectric, and quadrupolar response, demonstrating an unconventional forward versus backward luminescence enhancement. Through full-wave simulations we link these effects to the directional excitation strength of localized and delocalized magnetic surface waves in the array. While in this chapter we investigate a structure within a stratified medium (the array is covered by a thin luminescent layer), supporting calculations in Appendix A confirm that the physics we discuss remains even when the bare resonators are embedded in free space. Thus, unbalanced forward-backward light-emitting optical antennas could be integrated with a broad class of photonic building blocks in various environments. A clear application of the physics we discuss relates to light-emitting devices (LEDs), whose external quantum efficiency is typically degraded by absorption of the backwards emission into the device. As we will see, magnetoelectric nanoantennas can minimize this backwards emission. In turn, this effect may pave the way for a new generation of high-efficiency nanoantenna-enhanced LEDs free from lossy secondary optics used to partially recover the backwards emitted light.

5.2 Experiments

For the experiments, we fabricated an aluminum nanopyramid (ANP) array onto a fused silica substrate by substrate conformal imprint lithography [100]. We choose aluminum to operate in the visible spectrum. Its relatively high plasma frequency with respect to gold and silver renders blue-shifted resonances in structures with equal dimensions. The fabrication began by ultra- and mega-sonically cleaning the silica substrates with ozonated water, and drying with a nitrogen flow. Next, 150 nm of aluminum was sputtered on the silica substrate. A UV assisted curable silica sol-gel layer was spin-coated next in order to structure the aluminum layer. A pattern of pillars was then imprinted on this layer using a X-PDMS/soft-PDMS/thin glass stamp by means of the substrate conformal imprint lithography technology [100]. After curing the sol-gel for 5 minutes, the stamp was removed and a silica pattern of pillars remained. A residual layer of silicon oxide sol-gel was removed by a CF_4/N_2 reactive ion etching to expose the aluminum between the sol-gel pillars. Subsequently and without breaking vacuum, chlorine based etching with passivation from nitrogen and methane was used to etch the aluminum. The etching leads to aluminum structures tapered at a rate controlled by the ratio of chlorine to nitrogen and methane. Finally, samples were cleaned with an oxygen plasma to remove reactive species from the surface. The aluminum nanopyramids (ANPs) studied here have a height $h = 150 \pm 10$ nm, base length $b = 150 \pm 10$ nm, and top length $t = 70 \pm 10$ nm. The lattice is squared with a constant $a = 400$ nm. The inset in Fig. 5.1(a) displays an inclined-view scanning electron micrograph of the array. On top of the array we spin-coated a 250 nm layer of polystyrene doped with the organic dye Lumogen F305 at 1 weight % concentration, in order to probe the emission enhancement from this array.

Figure 5.1(a) shows the zeroth-order extinction spectrum, given by $1 - T_0$ with T_0 the zeroth-order transmittance. A collimated beam from a halogen lamp impinges at normal incidence, and the detector is a fiber-coupled spectrometer in the far-field. The incident polarization is parallel to either of the two equivalent orthogonal lattice vectors. As expected based on Lorentz reciprocity, and demonstrated by the overlapping black and gray

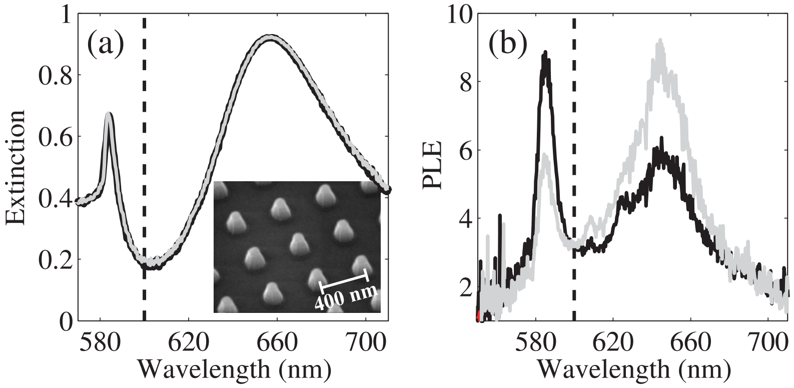

Figure 5.1: (a) Measured extinction, and (b) photoluminescence enhancement (PLE) towards the top (black line) and bottom (gray line) of the pyramids. The inset in (a) displays a scanning electron micrograph of the fabricated structures prior to the deposition of the luminescent layer. The dashed lines in (a) and (b) indicate the Rayleigh anomaly.

lines in Fig. 5.1(a), the extinction is identical when the sample is illuminated from the top (black line) or from the base of the ANPs (gray line). The broad peak near 650 nm in Fig. 5.1(a) is a localized surface plasmon resonance (LSPR) in the individual ANPs. The dip near 600 nm is attributed to the degenerate $(\pm1,0)$ and $(0,\pm1)$ RAs. The dashed black line indicates the RA condition, calculated for a refractive index of $n = 1.5$, intermediate to the index of the substrate ($n = 1.45$) and of the polystyrene layer ($n = 1.58$). The diffracted wave acquires an intermediate effective refractive index because its energy is divided between two media [86]. The narrow extinction peak at 584 nm is a SLR associated with the LSPR-RA coupling. The dye-doped polystyrene layer is sufficiently thin to only support one resonance near the diffraction edge, because the fundamental guided mode is close to cut-off. The association of the resonance peak in Fig. 5.1(a) with a SLR is confirmed by complementary measurements (not shown) indicating that for even thinner layers, where the fundamental guided mode is definitely cut-off, this resonance remains in the spectrum. For thicker layers a new resonance emerges due to the fundamental guided mode.

Next, we optically pump the sample and measure the emission towards the top and bottom of the ANPs. The pump is a 442 nm laser with a power far below saturation, impinging from above at $\theta_{in} = 5°$ from the normal. The detector is a fiber coupled spectrometer with $\mathrm{NA} = 4\times10^{-3}$. In correspondence to extinction measurements, we set a polarization analyzer in the collection path to only detect light polarized along one of the two equivalent lattice vectors, and approximately parallel (with a 5° offset) to the polarization axis of the pump laser. In Fig. 5.1(b) we plot the photoluminescence enhancement (PLE), given by the ratio of the emission from the dye layer with and without the ANPs. In both directions the PLE peaks at the LSPR and SLR wavelengths, but the magnitudes of these peaks are different. This unbalanced forward-backward light emission can be

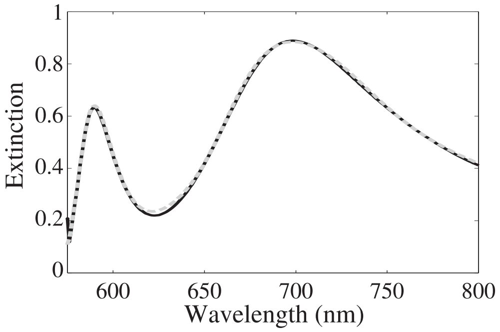

Figure 5.2: Extinction spectra obtained from full-wave simulations when the aluminum nanopyramid array is illuminated from the top (solid black line) and from the bottom (dashed gray line).

regarded as an emission counterpart of the Kerker condition in arrays of ANPs. Our findings demonstrate the potential of magnetoelectric nanostructures to spectrally modify the emission from planar sources otherwise emitting with equal intensities towards opposite directions. In what follows, we explain this effect by considering the local electromagnetic field enhancements at the LSPR and SLR wavelengths for opposite plane wave directions. For the LSPR, the greater PLE towards the bottom can be explained in terms of the radiative local density of optical states (LDOS) enhancement by the ANP. In Appendix A, we show that dipoles above the ANPs in a homogeneous medium preferentially radiate towards the bottom, as observed in experiments. It could be expected that, in the absence of any scatterer, the stratified medium favors emission into the substrate. However, measurements of the bare dye layer emission (shown in Ref. [208]) confirm that this effect is marginal. We stress that the PLE for each direction is referenced to the emission of the bare dye layer into the same direction. Furthermore, as demonstrated in Appendix A, the magnetoelectric LSPR alone imposes a large forward-backward emission asymmetry, in agreement with our measurements. An interesting effect in the measurements in Fig. 5.1(b) is that the SLR-enhanced emission is greater towards the top of the ANPs, opposite to the LSPR enhancement. Next, we explain this effect by means of numerical simulations.

5.3 Numerical simulations

In this section we present 3D finite element method (COMSOL) simulations to explain the nanoantenna enhanced anisotropic emission. First, by interchanging the positions of source and detector, we calculated the extinction spectrum for opposite plane wave directions. Figure 5.2 shows the extinction spectrum as a solid black line when a plane wave impinges from the top, and as dashed gray line when a plane wave impinges from the bottom. As expected based on reciprocity, the two extinction spectra are equal. The simulations display LSPR and SLR features in qualitative agreement with the experiments shown in Fig. 5.1(a). The LSPR peak wavelength in the simulations is somewhat red-shifted with respect to the experiments, possibly due to the experimental uncertainty in the dimensions of the fabricated structures and differences in the permittivity of aluminum (we used data from Palik [95].)

To connect experiments with simulations we use reciprocity: plane waves emitted by near-field sources correspond to near-fields illuminated by plane wave sources. While reciprocity establishes this relation [38, 209], it does not require the *local* fields to be identical for opposite illumination directions. Indeed, in previous Chapters we have addressed the shift of the near field with respect to the far field (see e.g. Chapter 3). Here, we illustrate the different local electromagnetic fields for the two different plane wave directions yielding the two spectra in Figure 5.2. We present the electric (**E**) and magnetic (**H**) field profiles at different planes of the structure, for the LSPR in Fig. 5.3 and for the SLR in Fig. 5.4. Panels (a-e) in both figures correspond to top-illumination, while panels (f-j) correspond to bottom-illumination. The color scale indicates the field intensity enhancement with respect to the incident wave, and the arrows represent the scattered field. In panels (a-d,f-i), in both Fig. 5.3 and Fig. 5.4, both enhancement and scattering pertain to the same field, either **E** or **H** as indicated on the top right corner of each figure. Panels (e,j) in both Fig. 5.3 and Fig. 5.4 show magnetic field enhancement in color and electric scattered field as arrows to visualize the magnetoelectric response, i.e. the excitation of magnetic moments by electric driving fields and viceversa. Next we interpret the results.

Figures 5.3(a,c) show two opposed electric dipoles at 140 nm and 10 nm from the base of the ANPs, respectively. In light of Faraday's law, from the curl of these two vector fields we expect an orthogonal magnetic dipole at an intermediate plane. Figure 5.3(b) shows **H** at such plane (50 nm above the base of the ANPs), where a magnetic near-field pattern is observed. Figures 5.3(d,e) show magnetic field enhancements localized near the lower half of the ANP. Notice in Fig. 5.3(d) that the magnetic scattered field circulates the ANP without significantly coupling to adjacent ANPs. Hence, the mode is localized. Figures 5.3(f-j) display similar field profiles for the LSPR excited from the bottom, but the field enhancements above the ANPs [Figs. 5.3(f,g,i,j)] are greater than for top-illumination. By reciprocity, this implies an enhanced emission towards the bottom, in agreement with our experiments. An important property of these localized electromagnetic resonances is that the electric and magnetic dipole moments are parallel to incident electric and magnetic fields, respectively. This contrasts with shallow planar structures (e.g. dolmens [202] and split rings [201]) where the magnetic dipole moment is orthogonal to magnetic driving field. Therefore, ANPs are ideally suited to realize the generalized near-field Kerker condition [210] and modify the forward-backward scattering or emission. Furthermore, as shown in Appendix A, the magnetoelectric response [magnetic (electric) dipole moment induced by electric (magnetic) field] saturates for ANPs higher that those used here. Hence, unnecessarily high structures should be avoided in order to minimize Ohmic losses.

In Fig. 5.4 we present a similar analysis for the SLR. Electric and magnetic dipole-like excitations are observed at the same planes as for the LSPR. However, the SLR field enhancements are greater and the modes are collective rather than localized. SLR fields with similar pattern but greater intensity than the associated LSPR fields also arise in structures with a dominant electric polarizability [76, 85, 86, 211]. The LSPR-RA hybridization

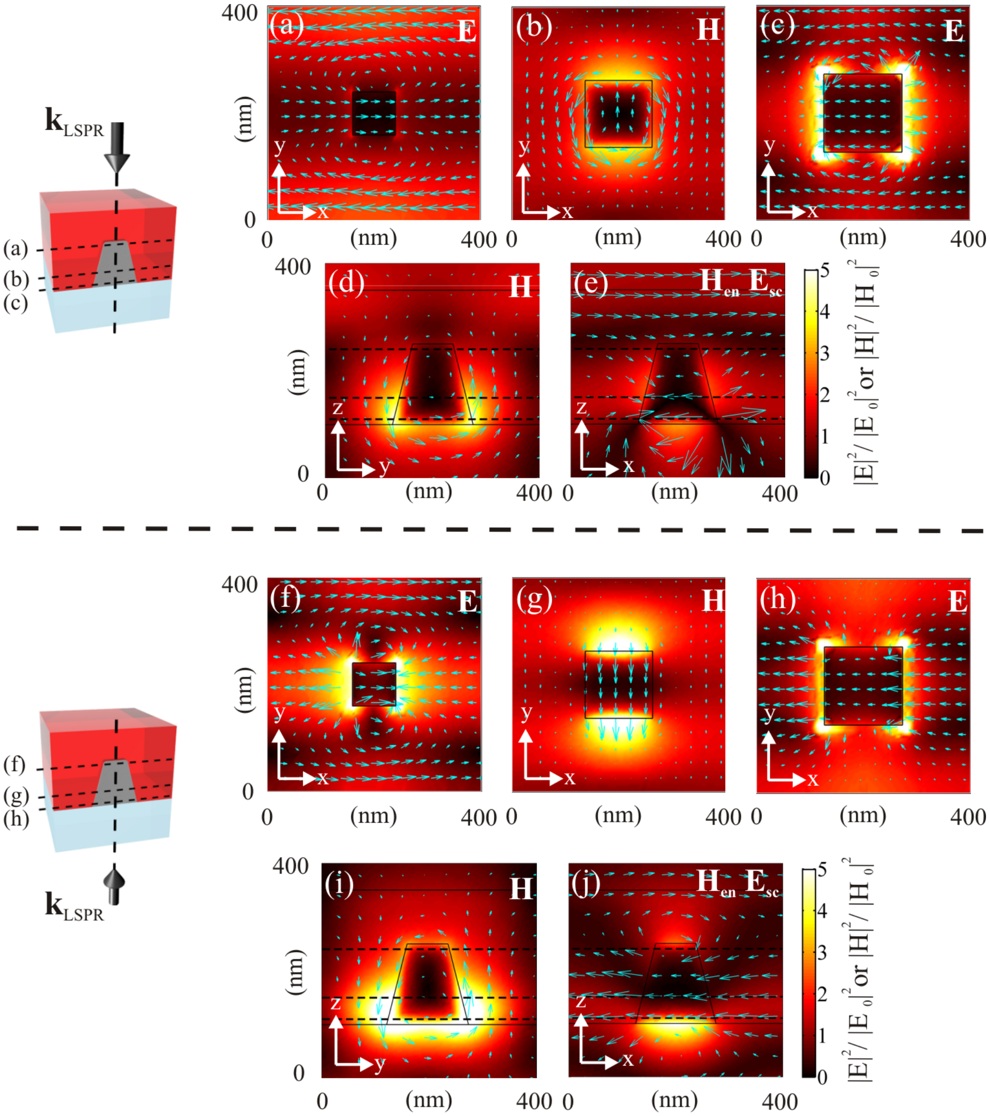

Figure 5.3: Electric (**E**) and magnetic (**H**) fields at the wavelength of the localized surface plasmon resonance. The color scale — equal for all plots in Fig. 5.3 and Fig. 5.4 — indicates the local field intensity enhancement with respect to the incident field indicated at the top right corner of each panel. The blue arrows represent the scattered field. Both color and arrows pertain to the same field, except in (e) and (j) where we show the **H**-field intensity enhancement and scattered **E**-field. Panels [(a)-(e)] correspond to top-illumination, while panels [(f)-(j)] correspond to bottom-illumination. The 3 horizontal dashed lines in figures (d,e,i,j) indicate, from top to bottom, the planes at which figures (a,b,c) are evaluated for top-illumination, and (f,g,h) for bottom-illumination.

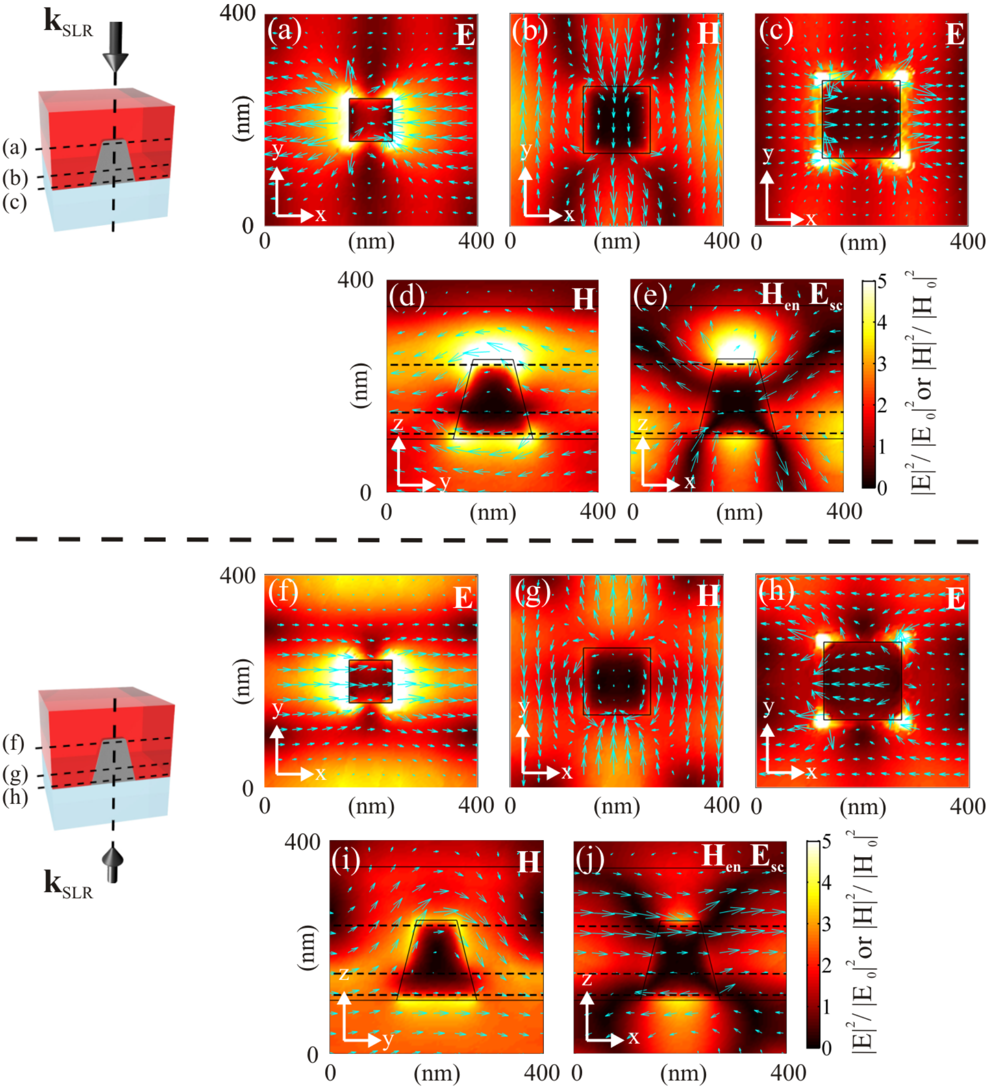

Figure 5.4: Electric (**E**) and magnetic (**H**) fields at the wavelength of the surface lattice resonance. The color scale — equal for all plots in Fig. 5.3 and Fig. 5.4 — indicates the local field intensity enhancement with respect to the incident field indicated at the top right corner of each panel. The blue arrows represent the scattered field. Both color and arrows pertain to the same field, except in (e) and (j) where we show the **H**-field intensity enhancement and scattered **E**-field. Panels [(a)-(e)] correspond to top-illumination, while panels [(f)-(j)] correspond to bottom-illumination. The 3 horizontal dashed lines in figures (d,e,i,j) indicate, from top to bottom, the planes at which figures (a,b,c) are evaluated for top-illumination, and (f,g,h) for bottom-illumination.

is responsible for the similar field patterns, while the large detuning makes the coupled resonances resemble the bare ones. In particular, the localized field enhancements of the hybridized LSPR resemble those of individual particles, while the SLR has delocalized field enhancements characteristic of long-range photonic modes. The long-range coupling at the SLR wavelength is more clearly visible in the out-of-plane magnetic [Figs. 5.4(d,i)] and magnetoelectric fields [Figs. 5.4(e,j)]. In contrast to the LSPR, the SLR fields in the luminescent layer are greater for top-illumination, in agreement with PLE measurements. This is likely due to a different phase relationship between the electric and magnetic dipole moment. The LSPR favors a fixed phase relationship, as in a split ring where these two dipole moments are dephased by $\pi/2$ [198]. At the SLR, lattice interactions renormalize the polarizability [200], such that the phase relation may reverse, and thereby the directionality. Finally, note that the opposing in-plane electric dipoles for the LSPR [Figs. 5.3(a,c)] and SLR [Figs. 5.4(a,c)] imply the existence of out-of-plane electric quadrupoles besides magnetic dipoles. While comparing the strength of these moments from simulations is difficult, calculations of α^S as shown in Appendix A can be insightful.

As a final remark, we note that the opposite in-plane electric dipoles for the LSPR and SLR, in Figs. 5.3(a,c) and Figs. 5.4(a,c) respectively, imply the existence of out-of-plane electric quadrupoles besides the aforementioned magnetic dipoles. While distinguishing the relative strength of magnetic dipoles and electric quadrupoles from numerical simulations can be difficult, analytical calculations of the the superpolarizability tensor can be insightful [202]. These calculations are presented in Appendix A for the bare aluminum nanopyramids in free space — in the absence of any stratified medium, as in the experiments. Therein, it is shown that the ANP tapering and height enhances these otherwise weak magnetoelectric and quadrupolar moments, and that this enhancement aids in breaking the light emission directional symmetry out of the periodicity plane.

5.4 Conclusions

In conclusion, we have demonstrated an unconventional forward versus backward luminescence enhancement from aluminum nanopyramid arrays. Underlying this effect is an enhancement of the magnetic, magnetoelectric, and quadrupolar response of the nanopyramids due to their tapering and height. Diffractive coupling of localized resonances in individual nanopyramids leads to collective resonances with full electromagnetic character, which constitute an unprecedented method for controlling light emission. The physics here explored provides a design principle for unidirectional light-emitting devices, and by reciprocity, for boosting light absorption in thin-film solar cells that are unidirectionally illuminated. From a fundamental perspective, we believe that the advent of magnetic surface lattice resonances holds great promise for the creation of novel light-matter states through strong coupling to quantum emitters. For instance, by increasing the concentration of molecules covering the nanopyramid array, we envisage the emergence of plasmon-exciton polaritons as discussed in Chapter 4, but with magnetic degrees of freedom.

CHAPTER 6

ACTIVE CONTROL OF NANOANTENNA ENHANCED LIGHT EMISSION WITH LIQUID CRYSTALS

We demonstrate active spectral and directional control of narrowband (~ 6 nm) light emission enhancements by a nanoantenna array. The system we study comprises an aluminum nanoantenna array on top of a light-emitting quantum dot waveguide and covered by a thremotropic liquid crystal (LC). The orientation of the LC molecules (and thus the effective refractive index of the layer they compose) depends on the local temperature, and this allows us to modify the light extinction and emission due to hybrid plasmonic-photonic resonances.

6.1 Introduction

In Chapters 2, 3, 4, 5 we have shown how metallic nanoparticle arrays can provide light emission directivity gain, polarization control, intensity enhancements, and spectral shaping. A long-standing goal in nanophotonics is to actively control these coupling-enhanced emission properties by means of an external tuning parameter. This can be achieved by incorporating materials with a refractive index or geometry that depend on an applied voltage, heat, strain, or illumination profile [212–216]. Liquid crystals (LCs) are interesting materials for this purpose, because their tunable orientation can modify the resonance conditions of nearby optical resonators. Indeed, LCs have enabled active control of resonances in diverse metallic structures, including metallic nanoantennas supporting localized surface plasmon resonances (LSPRs), and continuous metallic films supporting propagating surface plasmon polaritons [217–226]. While powerful, these approaches suffer from inherent drawbacks in the context of light emission. On one hand, the influence of LSPRs is spatially restricted to emitters located within their characteristic decay lengths (typically < 40 nm) [4]. On the other hand, the large amount of non-radiative decay channels in continuous metallic films can lead to emission quenching [101]. An interesting approach to overcome these limitations consists of coupling LSPRs in individual nanoantennas to long-range photonic modes in dielectric structures, e.g. diffracted or guided modes. This coupling leads to hybrid plasmonic-photonic modes such as surface lattice resonances (Chapters 2 and 4) or waveguide-plasmon polaritons (Chapter 3). The dispersion, linewidth, and field confinement of these hybrid modes can be flexibly designed via the geometry and dimensions of the structures (Chapter 2), or of the emitting layer (Chapter 3). Moreover, their fields can be constructed to spatially overlap with nearby emitters extended over large areas in a polarization, frequency, and angle-dependent manner. The long-range character of these hybrid modes is well suited to modify the emission from spatially extended sources in the periodicity plane, while preserving sub-wavelength confinement out of the same plane. Thus, we envisage that active control of these hybrid modes holds great promise for applications in solid state lighting, lasers, and on-chip photon sources.

In this Chapter we demonstrate active LC tuning of a spectrally narrow photoluminescence enhancement (PLE) by a periodic array of plasmonic antennas coupled to a waveguide. The structure we investigate consists of an aluminum nanodisk array fabricated on top of an emitting layer (acting as a waveguide) of colloidal quantum dots (QDs), and coated with a thermotropic LC. Colloidal QDs are convenient emitters for this purpose as they offer sharp and tunable emission properties, even at ambient or higher temperatures, in combination with a versatile processability [227]. The active tuning is achieved by changing the temperature of the sample. Above a critical temperature T_c, the orientation of the LC becomes randomized and the effective refractive index switches from birefringent to isotropic. Through variable angle extinction and photoluminescence measurements at temperatures well below and above T_c, we evidence the impact of this transition on the optical resonances of this system. Numerical simulations utilizing the finite element method are used to elucidate the tuning mechanism. As we show, from the interplay between coupling, detuning, and radiative losses of this system, emerges a pow-

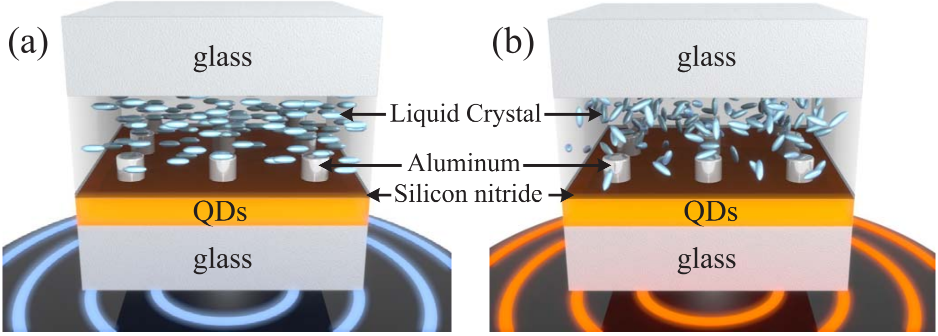

Figure 6.1: Schematic representation of the sample. (a) At room-temperature (~ 23°C) the liquid crystal is ordered, making the medium overlying the plasmonic antennas birefringent. (b) At higher temperatures (> 58°C) the liquid crystal is disordered, yielding an isotropic refractive index in the same medium.

erful approach to actively control the emission spectrum and directionality of extended sources.

6.2 Sample fabrication

Figure 6.1 shows a sketch of the sample investigated in this Chapter. First, CdSe/CdS/ZnS core-shell QDs were synthesized starting from CdSe seeds with a zinc blende structure [228] through a successive ion layer adsorption and reaction procedure [229]. The resulting QDs had an average diameter of 6.5 nm and a peak emission at 585 nm. The QDs, dispersed in toluene, were spin-coated on a glass substrate. This resulted in a 120 nm thick QD layer as determined by atomic force microscopy. A protective silicon nitride layer of 15 nm was deposited on top of the QD layer by plasma-enhanced chemical vapor deposition in order to planarize the surface. A relatively low temperature (120°C) was used in the deposition to avoid degradation of the QDs. Aluminum nanodisk arrays were fabricated on top of the silicon nitride layer by substrate conformal imprint lithography [100]. The nanodisks have a nominal height of 150±20 nm, diameter of 120±20 nm, and are arranged in a square lattice with a periodicity of 390 ± 10 nm. To control the LC orientation, we placed a thin layer of nylon alignment material over the array (not shown in Figure 6.1). This material is mechanically rubbed to force the LC to orient in a planar direction along one of the lattice vectors. Finally, UV curable glue containing spacer balls with a diameter of 6 μm (not shown in Figure 6.1) is placed at the edge of the substrate, away from the array, to attach a glass plate to the sample. The space between the array and the top glass plate is filled with LC E7 (Merck) which has a critical temperature $T_c = 58°C$ [230].

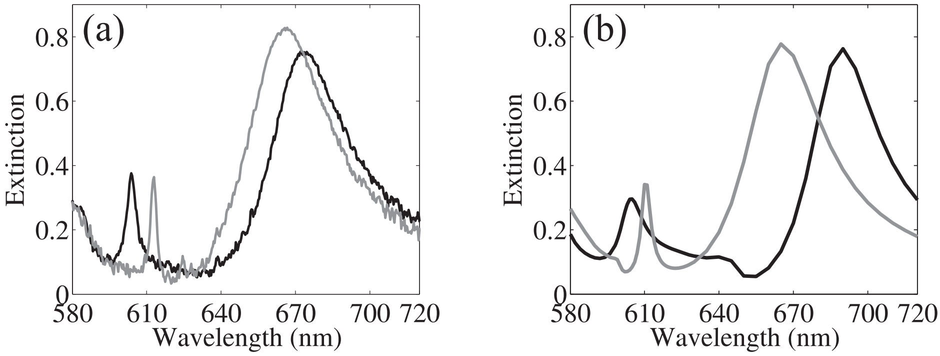

Figure 6.2: (a) Measured normal incidence extinction spectra at 23°C (black line) and 75°C (gray line), which are below and above the liquid crystal critical temperature, respectively. (b) Simulated extinction spectra for birefringent (black line) and isotropic (gray line) liquid crystal conditions, in correspondence to experiments at 23°C and 75°C, respectively.

6.3 Normal incidence extinction and forward emission

We measured the normal incidence extinction spectrum of the sample at room temperature (23°C) and above T_c (75°C). A collimated beam (angular spread $< 0.1°$) from a halogen lamp illuminates the sample with a linear polarization along the extraordinary index direction of the LC, which is aligned with one of the lattice vectors of the array. A fiber-coupled spectrometer measures the zeroth order transmittance T_0 in the far-field. The extinction follows as $1 - T_0$.

Figure 6.2(a) shows the extinction spectra at 23°C as a black line, and at 75°C as a gray line. At both temperatures, the two peaks in extinction correspond to hybridized plasmonic-photonic resonances. These resonances arise from the coupling between localized surface plasmons in the nanodisks and the fundamental Transverse Magnetic (TM_0) guided mode in the QD layer. The properties of the bare TM_0 guided mode are discussed further below, in view of numerical simulations results. In Chapter 3 it was shown that strong coupling between localized surface plasmons and guided modes leads to hybrid waveguide-plasmon polaritons. When the bare LSPR and guided mode frequency detuning is zero, the emergent waveguide-plasmon-polaritons are half plasmon-like and half guided mode-like. In contrast, the LSPR and TM_0 guided mode in this Chapter are coupled but largely detuned, i.e., their peak wavelengths are significantly apart. The large detuning makes the coupled modes resemble one or the other of the bare modes. In Fig. 6.2(a) particularly, the broad resonance at long wavelengths is reminiscent of the LSPR, while the sharper resonance at short wavelengths is reminiscent of a quasi-guided mode. The coupled mode is quasi-guided because its radiative coupling to the antennas makes it leaky. In view of these effects, we shall hereafter refer to the broad resonance as the hybridized LSPR and to the narrow resonance as the quasi-guided mode. We reserve the term waveguide-plasmon polariton for the case where these hybrid modes are tuned in resonance, as shown in Chapter 3.

Notice in Fig. 6.2(a) that, upon increasing the temperature of the sample, the hybridized LSPR and quasi-guided mode shift. The shift is due to a transition of the LC from an ordered [Fig. 6.1(a)] to a disordered [Fig. 6.1(b)] state. This transition removes the birefringence characterizing the LC effective medium at room temperature, and an isotropic refractive index sets in at high temperature. The observed spectral shifts were experimentally verified to be reversible upon successive heating and cooling of the sample. An interesting aspect in Fig. 6.2(a) is the fact that the two extinction peaks shift in opposite direction: the hybridized LSPR blue-shifts, while the quasi-guided mode red-shifts. The LC phase transition affects the optical modes differently, indicating that in the birefringent state (at room temperature) each mode mainly samples a different refractive index.

To understand the temperature dependence of the optical resonances, we simulated the response of the system using a finite element method (COMSOL). In the simulations, plane waves impinge from the LC layer, which is assumed to have infinite thickness above the array. Below the critical temperature, we assume that the LC layer is perfectly ordered and aligned along the rubbing direction. Consequently, the LC constitutes a homogeneous anisotropic material with a weakly dispersive ordinary ($n_o \approx 1.52$) and extraordinary ($n_e \approx 1.73$) refractive index. Above $\mathrm{T_c}$, the LC layer is assumed to be completely isotropic, with a refractive index n_c approximately given by the weighted average of the ordinary and extraordinary refractive indices: $n_c \approx \frac{(2n_o+n_e)}{3} \approx 1.59$. The frequency-dependent LC refractive index is taken from literature [230, 231], while for the glass, QD layer, and aluminum we have obtained them from ellipsometric measurements.

Figure 6.2(b) shows the $1 - T_{\mathrm{Total}}$ spectra where T_{Total} is the total transmittance obtained from the simulations. The simulated spectrum displays resonance wavelengths and shift directions in good agreement with the experiments. To achieve this good agreement, the dimensions were slightly changed in the simulations with respect to the nominal values of the fabricated structures. Specifically, the simulated particle height and diameter both are 100 nm, while the lattice constant is 378 nm. We attribute these deviations to uncertainties in the fabrication, which could have rendered structures with dimensions differing from the nominal ones. In addition, small discrepancies between the simulated and experimental refractive indices could also exert an influence on our results.

The connection between the sharp resonance at shorter wavelengths in our measurements with the $\mathrm{TM_0}$ guided mode in the QD layer was established through eigenmode simulations using COMSOL. We calculated the dispersion of the $\mathrm{TM_0}$ guided mode in the same multi-layer structure discussed above, but without the nanodisk array. Both anisotropic and isotropic LC conditions were considered. The simulations indicate that the multi-layer structure supports an eigenmode — the $\mathrm{TM_0}$ guided mode in the QD layer — with a dispersion relation closely following the dispersion relation of the sharp feature in our measurements. The dispersion of this mode is shown below, in Figure 6.5, in connection to angle-resolved data. While such a guided mode is bound to the high refractive index layer in absence of the nanodisk array, the periodic array can couple a normal incident plane wave into (or out of) this mode at wavelengths close to the diffraction edge. This is the origin of the sharp resonance in the measurements of Figure 6.2(a), which is related to the plane wave excitation of a guided mode via the first diffraction order.

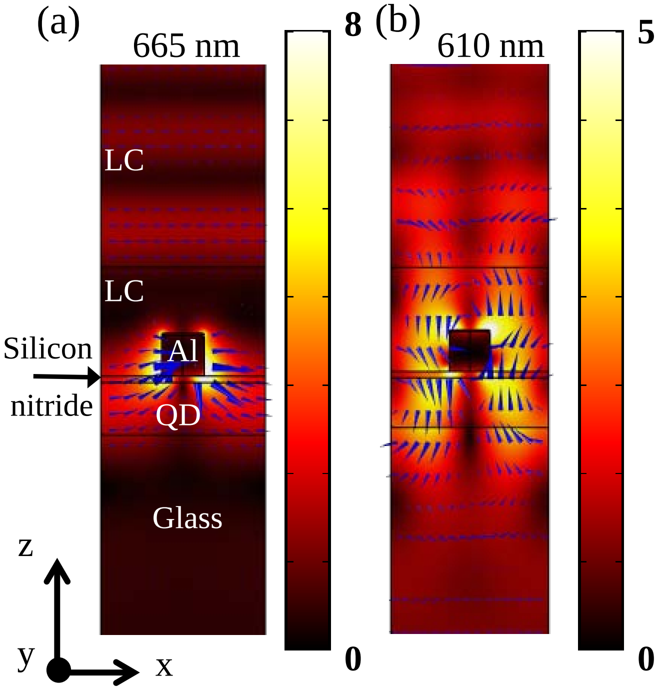

Figure 6.3: Total field enhancement for isotropic LC (above T_c) at a wavelength of (a) 665 nm (hybridized LSPR) and (b) 610 nm (quasi-guided mode). The incoming field is polarized along x. For all graphs, the blue arrows show the E field at a certain phase.

We verified (details in Ref. [232]) through full field simulations that when the QD layer thickness is increased, the short wavelength resonance red-shifts. This is in agreement with the expected behavior of the fundamental TM_0 guided mode in the QD layer.

To examine the coupled nature of the modes in more detail, we plot the field enhancement $|\mathbf{E}|/|\mathbf{E}_{\text{input}}|$ at an xz-plane intersecting the nanodisks at their center. We do this for the broad resonance at 665 nm in Figure 6.3(a), and for the narrow resonance at 610 nm in 6.3(b), both above T_c. The field profiles are very similar below T_c. In Figure 6.3(a) we observe that the electric field enhancement is mostly localized near the metallic nanostructure, resembling the characteristics of bare LSPRs. In contrast, Figure 6.3(b) shows a delocalized field enhancement, characteristic of a guided mode close to cut-off (as it may be expected due to the small waveguide thickness and the asymmetry of the refractive index of the upper and lower media). Note, however, that this delocalized field enhancement is relatively strong in the vicinity of the nanodisks, indicating once more that waveguide-LSPR coupling is present.

An interesting observation in Figure 6.3 concerns the dominant field components of each mode. In fact, this is the reason behind the different shift directions upon temperature increase. The hybridized LSPR has a dominant electric field component parallel to the input plane wave polarization [x direction, along the blue arrows in Figure 6.3(a)]. Therefore, this mode mainly samples the extraordinary refractive index n_e of the LC layer in the birefringent state. In contrast, the quasi-guided mode has a dominant electric field component along the z-direction [blue arrows in Figure 6.3(b)], because the guided mode is TM polarized. Therefore, this mode mainly samples the ordinary refractive index n_o of the LC layer in the birefringent state. Note that the relation between the LC refractive indices is $n_o < n_c < n_e$. Hence, in the transition to the isotropic state, the quasi-guided mode experiences an increase of effective index (and therefore a red-shift) while the opposite occurs for the hybridized LSPR (it blue-shifts).

Next we discuss the light emission enhancement rendered by the quasi-guided mode, which is in spectral overlap with the QD emission. For this purpose, we measured the photoluminescence enhancement (PLE) of the sample at 23°C and 75°C. The QDs were pumped with a 450 nm laser beam at a fixed angle of incidence (5°) from the normal. The emitted light at different directions was collected by the same fiber-coupled spectrometer used for the extinction measurements. The PLE is defined as I_{in}/I_{out}, with I_{in} the emitted intensity from the QDs in the presence of the nanodisk array, and I_{out} without the array. Figure 6.4(a) shows the PLE spectra in the direction normal to the periodicity plane. The inset of Fig. 6.4(a) shows the raw spectra of the bare QD layer without the nanoantennas as a black line, with the nanoantennas and the LC layer at 23°C as a dark gray line, and with the nanoantennas and the LC layer at 75°C as a light gray line. Up to six-fold directional light emission enhancement by the quasi-guided mode is observed in the PLE measurements above T_c. As in extinction, the PLE feature due to this mode red-shifts, and its linewidth becomes narrower when the temperature is increased. Furthermore, the PLE is greater at higher temperatures. By fitting the PLE peak at 75°C with the Fano formula (Eq. 1.6), we retrieve a linewidth of 6 nm. This narrow PLE linewidth demonstrates the strength of hybrid plasmonic-photonic modes for emission enhancement purposes by providing nanoscale spectral selectivity and low loss. We highlight that maximizing the PLE factor is not the subject of this Chapter, as this has been done in previous works [90]. Instead, we demonstrate the possibility to actively control the PLE by means of an external tuning parameter (the temperature change in this case).

To elucidate the PLE measurements, we simulate the spectral dependence of the field enhancement in the QD layer. We define the electric field intensity enhancement in the QD layer by the nanodisk array as $I_E = |E|^2/|E_0|^2$, with E and E_0 the total and incident electric field spatially integrated over the QD layer. While in the simulations I_E is a measure of the excitation strength of an optical mode, by reciprocity it also represents a decay strength of the same mode to outgoing plane waves with the same direction. Thus, I_E correlates with the PLE in the measurements.

Figure 6.4b shows I_E for a plane wave at normal incidence. The calculated peak in I_E due to the quasi-guided mode reproduces the temperature dependence observed in our PLE experiments. This peak experiences a red-shift and linewidth narrowing. Furthermore, the enhancement also increases. Inspection of the field profiles reveals that the linewidth narrowing is associated with a weaker confinement of the mode to the metallic structure in the isotropic state. The weaker confinement is due to a lower index contrast between the QD layer and the isotropic LC layer, and results in lower Ohmic losses.

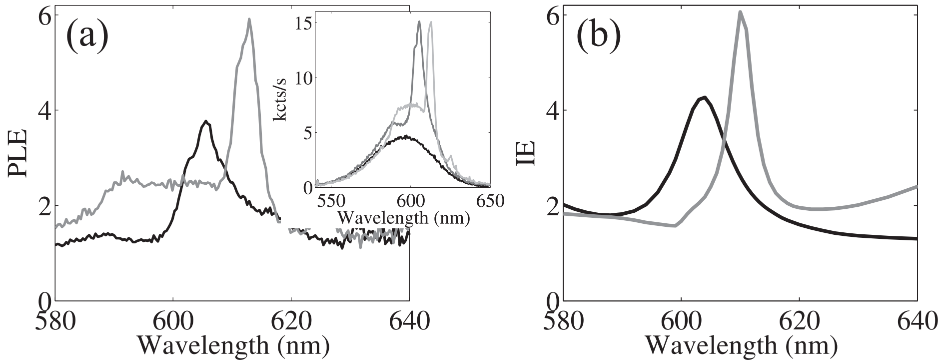

Figure 6.4: (a) Measured photoluminescence enhancement in the direction normal to the sample at 23°C and at 75°C. The red dotted curve is a fit of a Fano function to the PLE peak at 75°C. The inset in (a) shows the QD emission with (gray line) and without (black line) the array, both at 23°C, all for the same pump intensity. (b) Calculated integrated intensity enhancement in the QD layer I_E for perfect anisotropic and isotropic LC conditions.

6.4 Variable angle extinction and emission

We now analyze the variable angle extinction and PLE spectra, measured with the experimental setups shown in Figs. 2.1(a,b). Figure 6.5(a,b) shows the measured extinction at 23°C and 75°C respectively, while Fig. 6.5(c,d) displays the PLE, for the same two temperatures. In all plots the bands of enhanced extinction or PLE correspond to the excitation of quasi-guided modes. The variable angle data shows a similar shift of this resonance in both extinction and PLE over the entire band when the LC layer transitions from birefringent to isotropic, as observed at normal incidence [Figures 6.2a and 6.4(a)]. Consequently, the directionality of the emission enhancement provided by the quasi-guided mode is actively tuned by the LC transition.

Comparing Figs. 6.5(a) with 6.5(c), and 6.5(b) with 6.5(d), one sees that the dispersion of the quasi-guided mode in PLE closely resembles that in extinction. Furthermore, in all dispersion diagrams the quasi-guided mode closely follows the calculated dispersion of the TM_0 guided mode for the structure without the nanodisk array, indicated by the white dashed lines in all panels of Fig. 6.5. The proximity in wavelength of the quasi-guided mode to the bare guided mode suggests once more that the hybrid mode resembles the bare mode, and that the coupling to the LSPR has a small influence due to the large detuning between the modes. This is, however, not a detriment for our purpose of actively tuning the PLE due to the quasi-guided mode via the LC phase transition. In fact, the large out of plane fields of the bare TM_0 guided mode (and also of the coupled mode resembling the bare one) make it more sensitive to refractive index changes in the LC layer. Clearly, this allows for a greater degree of tunability given the fixed contrast between the ordinary and extraordinary refractive indices of the LC layer.

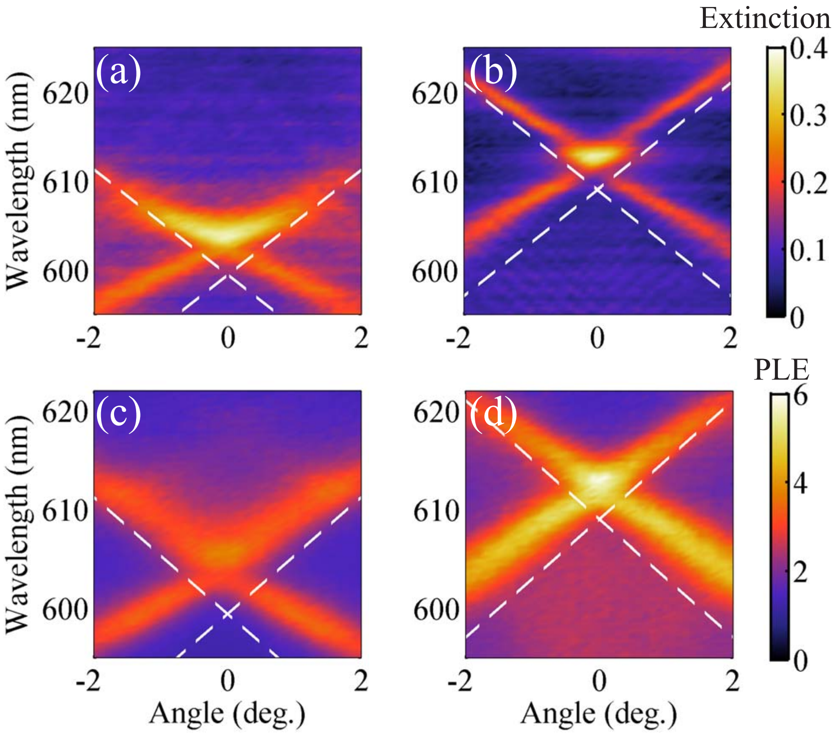

Figure 6.5: Measured extinction dispersion spectra at (a) 23°C and (b) 75°C. Measured photoluminescence enhancement dispersion spectra at (c) 23°C and (d) 75°C. The white dashed lines in all the plots represent the dispersion of the TM_0 guided mode in the same multi-layer structure but without the nanoantenna array.

6.5 Conclusions

In conclusion, we have demonstrated active spectral and directional tuning of the enhanced light emission of quantum dots coupled to optical antennas. For this purpose, we employed a spectrally sharp (~ 6 nm) hybrid plasmonic-photonic mode emerging from the radiative coupling between localized surface plasmons and a guided mode in a quantum dot emitter layer. The tunability was achieved by covering the array with a thermotropic liquid crystal (LC), which changes from a birefringent to an isotropic state above a critical temperature. In turn, this modifies the resonance conditions of the coupled system. Supporting our experiments with numerical simulations, we have shown that the tuning mechanism depends on the field profile, and more specifically on the orientation of the dominant mode polarization in the LC layer with respect to the LC axis. Having established the suitability of these hybrid modes for active control of light emission enhancements from optical antennas, we envisage future works to boost the enhancement factors by optimizing the field overlap between the optical mode and the emitters. For even greater field overlaps (coupling strengths), this system could enter into the strong coupling regime, where the coupling rate exceeds the loss rates. In this case, active control of strong coupling appears as a fundamentally interesting possibility [127]. From an applied perspective, we believe that these results hold great promise for smart lighting applications profiting from active beaming and color tuning. Active light emission tuning is especially attractive in the wavelength range explored in this Chapter, because in this range the human eye translates small wavelength variations to significant color differences.

Appendices

APPENDIX A

SUPPORTING CALCULATIONS FOR CHAPTER 5

A.1 Superpolarizability tensor calculations of bare aluminum nanostructures

In Chapter 5 we argued that even the bare aluminum nanopyramids (ANPs) in free space — in the absence of a stratified medium, as in the experiments — sustain an enhanced magnetoelectric and quadrupolar response due to the tapering and height of the nanostructures. In this section, we support this claim through analytical calculations of the ANP's electromagnetic response separate from lattice and interface effects. The calculations in this appendix were performed by Felipe Bernal Arango, working in the group of Femius Koenderink at AMOLF, and in close collaboration with our group.

We present calculations of the 11×11 super polarizability tensor α^S [202, 233, 234] of ANPs in free space ($n = 1$). α^S quantifies the electric, magnetic, and magnetoelectric dipole moments, as well as the quadrupole moments of an arbitrary structure. The upper left 6×6 elements of α^S describe the excitation of dipolar electric **p** and magnetic **m** moments by electric **E** and magnetic **H** driving fields. In this block, the diagonal 3×3 blocks represent purely electric and magnetic polarizability ($\mathbf{p} = \alpha_E \mathbf{E}$, and $\mathbf{m} = \alpha_H \mathbf{H}$) dipoles, whereas the off-diagonal magnetoelectric coupling terms represent 'bi-anisotropy', i.e. the excitation of electric (magnetic) dipoles by magnetic (electric) fields. The bottom 5 rows of α^S describe the quadrupolar moments **Q** driven by **E** and **H**. The rightmost 5 columns represent the induced dipole moments **p** and **m** due to symmetric gradients of the field $\lozenge\mathbf{E}$, with the symmetric gradient operator $\lozenge$ defined as $\lozenge\mathbf{E} = (1/2)\{(\partial_x E_y + \partial_y E_x), (\partial_x E_z + \partial_z E_x), (\partial_y E_z + \partial_z E_y), 2\partial_x E_x, 2\partial_y E_y\}$ when acting over a 3-vector **E**. The 5×5 lowest diagonal block is the quadrupolarizability tensor [235], representing the quadrupolar moments excited by $\lozenge\mathbf{E}$. The superpolarizability is obtained by full-wave calculations for 11 linearly

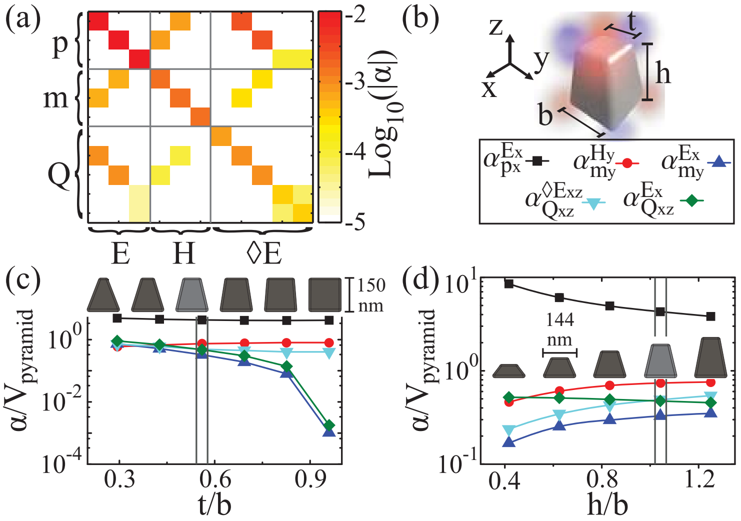

Figure A.1: (a) Superpolarizability tensor α^S of an aluminum pyramid with t=84 nm, h=150 nm and b=144 nm, at the electric dipolar resonance wavelength. (b) Schematic of the structure, and legend of Figs. (c,d). (c) and (d) display the most significant elements of α^S as function of the tapering and height of the pyramids, respectively.

independent incident conditions of the object scattering response, that we project onto vector spherical harmonics [234].

Figure A.1(a) shows a graphical representation of α^S for ANPs with top size $t = 84$ nm, height $h = 150$ nm, and base $b = 144$ nm, in reference to Fig. A.1(b). The excitation wavelength is 660 nm. In the system of units we use (see Units section A.3), all elements of α^S can be compared quantitatively, i.e., as yielding identical scattering power at identical value. The ANPs in Fig. A.1(a) posses a strong magnetoelectric cross-coupling polarizability α_C (tensor elements [4,2],[2,4],[5,1] and [1,5]). Comparing this to the electric polarizability, we find $|\alpha_E|/|\alpha_C|$=13. This resembles split ring resonators — the archetypical metamaterial building blocks due to their enhanced magnetic and magnetoelectric response — operating at infrared frequencies [234, 236], but now operating at visible frequencies. Figure A.1(a) further shows that x or y polarized plane waves, without a strong gradient, directly induce quadrupoles in the xz and yz planes. The magnetic dipoles along x and y and the quadrupoles in the yz and xz planes, respectively, are intimately related through the rotational symmetry of the structure.

We now analyze how α^S depends on the ANP dimensions. To fairly compare different structures, we divide α^S by the volume of the corresponding structure. The exact geometries and volumes of the calculated structures are provided in next section, i.e. A.2. We consider x-polarized illumination, for which the most significant elements of α^S are indicated by the legend in Fig. A.1(b). α^S is evaluated at the electric dipolar resonance wavelength for each structure, which varies from 660 nm due to the different dimensions. Firstly, we fix $b = 144$ nm, $h = 150$ nm, and we vary t as shown in the top part of Fig. A.1(c).

Figure A.1(c) shows that the magnetoelectric (α_{my}^{Ex}) and quadrupolar (α_{Qxz}^{Ex}) response are weak without tapering, but increase monotonically by 3 orders of magnitude for increased tapering. Secondly, in Fig. A.1(d) we fix $t = 84$ nm, $b = 144$ nm, and vary h. The magnetic (α_{my}^{Hy}), magnetoelectric (α_{my}^{Ex}), and quadrupolar (α_{Qxz}^{Ex}) response increase monotonically while the electric dipole (α_{px}^{Ex}) response decreases. Thus, the results in Figs. A.1(c,d) convey a geometrical design strategy for α^S, enabling to increase the magnetoelectric and quadrupolar response via the ANP's tapering and height. This enables us to approach the generalized near-field Kerker condition as described in Ref. [210], without modifying the magnetic permeability μ. In turn, radiation patterns with a pronounced forward to backward asymmetry are expected. Note that the magnetoelectric enhancement saturates for increased h. Therefore, unnecessarily high structures must be avoided to minimize Ohmic losses without degrading the magnetoelectric response. In this spirit, we indicate by vertical lines in Figs. A.1(c,d) the ANP in our experiments in Chapter 5, for which α^S is shown in Fig. A.1(a).

A.2 Geometries and Volumes of the Structures in Figure A.1

Here we provide further details on the structures for which the super polarizability tensor, α^S, is calculated in Fig. A.1(a). The top row in Fig. A.2 displays a variation in the top size t, yielding the results in Fig. A.1(c). From right to left, the volumes of these structures are: $3.03 \times 10^{-3} \mu\text{m}^3$, $2.64 \times 10^{-3} \mu\text{m}^3$, $2.29 \times 10^{-3} \mu\text{m}^3$, $1.97 \times 10^{-3} \mu\text{m}^3$, $1.7 \times 10^{-3} \mu\text{m}^3$, $1.47 \times 10^{-3} \mu\text{m}^3$. The bottom row displays a variation in the height h. From right to left, the volumes of these structures are: $2.37 \times 10^{-3} \mu\text{m}^3$, $1.97 \times 10^{-3} \mu\text{m}^3$, $1.58 \times 10^{-3} \mu\text{m}^3$, $1.19 \times 10^{-3} \mu\text{m}^3$, $0.793 \times 10^{-3} \mu\text{m}^3$. The lightest gray pyramid in the top and bottom rows in Fig. A.2 (these two are identical) is the one used for the experiments in Chapter 5, which is also the one for which α^S is shown in Fig. A.1(a).

The elements of α^S shown in Fig. A.1(c,d) are evaluated at the electric dipolar resonance wavelength of each pyramid. For the structures in the top row of Fig. A.2, from left to right these wavelengths are: 600 nm, 620 nm, 660 nm 680 nm, 720 nm and 740 nm. For the structures in the bottom row of Fig. A.2, from left to right these wavelengths are: 560 nm, 580 nm, 620 nm, 660 nm and 700 nm.

A.3 Units

In order to make a fair quantitative comparison between the different elements of α^S for different structures, we employ a system of units in which elements with identical strength radiate equal power into the far-field. Thus, we use a non-SI scaling of the elements similar to the CGS unit system. Here we give the conversion from this units system to the SI units system.

We begin by scaling the fields, so that the electric field, magnetic field, and the symmetrical gradients of the field share as common unit volts per meter [V/m]. In this way, a

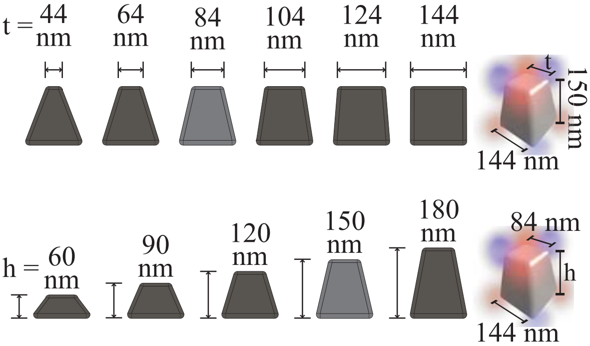

Figure A.2: Geometries of the pyramids used for the calculations in the manuscript. The top line shows the array of pyramids with variations in their top size. The bottom line shows the array of pyramids with variations in their height.

simple plane wave represents unit strength for all its nonzero components. The conversion between the new units and SI units is:

$$\mathbf{E} = \mathbf{E}_{\mathrm{SI}}, \quad \mathbf{H} = Z_0 \mathbf{H}_{\mathrm{SI}} \quad \text{and} \quad \Diamond\mathbf{E} = k\Diamond\mathbf{E}_{\mathrm{SI}}. \tag{A.1}$$

Here, Z_0 is the free space impedance and $k = 2\pi/\lambda$ is the magnitude of the wave vector. Subsequently, we scale the induced moments from their definition in SI units in order to obtain $[\mathrm{C}\cdot\mathrm{m}]$ (Coulomb meter) as a common unit, such that any dipolar or quadrupolar moment of unit strength radiates equal power into the far-field. The conversion between the new units and SI units is:

$$\mathbf{p} = \mathbf{p}_{\mathrm{SI}}, \quad \mathbf{m} = (1/c)\mathbf{m}_{\mathrm{SI}} \quad \text{and} \quad \mathbf{Q} = \frac{k}{\sqrt{60}}\mathbf{Q}_{\mathrm{SI}}. \tag{A.2}$$

The factor $k/\sqrt{60}$ follows from the formula $P = c^2 Z_0 k^6/(1440\pi)\sum_{\alpha,\beta}|Q_{\mathrm{SI},\alpha,\beta}|^2$, which is the equivalent of Larmor's formula and gives the power radiated into the far-field by a quadrupole. For a dipole, Larmor's formula states that $P = c^2 Z_0 k^4/(12\pi)|\mathbf{p}_{\mathrm{SI}}|^2$ is the power radiated into the far-field by a dipole. Finally, we note that in this system of units, α^S has units of $\epsilon_0\mathrm{m}^3$ for all entries, with equal entries contributing equally to the scattered power. For convenience, here we show the conversion for all elements. The block diagonals are converted in the following way,

$$\alpha_{\mathbf{p}}^{\mathbf{E}} = {\alpha_{\mathrm{SI}}}_{\mathbf{p}}^{\mathbf{E}}, \quad \alpha_{\mathbf{m}}^{\mathbf{H}} = \frac{1}{Z_0 c}{\alpha_{\mathrm{SI}}}_{\mathbf{m}}^{\mathbf{H}}, \quad \text{and} \quad \alpha_{\mathbf{Q}}^{\Diamond\mathbf{E}} = \frac{k^2}{\sqrt{60}}{\alpha_{\mathrm{SI}}}_{\mathbf{Q}}^{\Diamond\mathbf{E}}, \tag{A.3}$$

while the off-diagonal blocks are converted as follows

$$\begin{gathered}\alpha_{\mathbf{m}}^{\mathbf{E}} = \frac{1}{c}{\alpha_{\mathrm{SI}}}_{\mathbf{m}}^{\mathbf{E}}, \quad \alpha_{\mathbf{p}}^{\mathbf{H}} = \frac{1}{Z_0}{\alpha_{\mathrm{SI}}}_{\mathbf{p}}^{\mathbf{H}}, \quad \alpha_{\mathbf{Q}}^{\mathbf{E}} = \frac{k}{\sqrt{60}}{\alpha_{\mathrm{SI}}}_{\mathbf{Q}}^{\mathbf{E}}, \\ \alpha_{\mathbf{Q}}^{\mathbf{H}} = \frac{k}{Z_0\sqrt{60}}{\alpha_{\mathrm{SI}}}_{\mathbf{Q}}^{\mathbf{H}}, \quad \alpha_{\mathbf{p}}^{\Diamond\mathbf{E}} = k{\alpha_{\mathrm{SI}}}_{\mathbf{p}}^{\Diamond\mathbf{E}}, \quad \alpha_{\mathbf{m}}^{\Diamond\mathbf{E}} = \frac{k}{c}{\alpha_{\mathrm{SI}}}_{\mathbf{p}}^{\Diamond\mathbf{E}}.\end{gathered} \tag{A.4}$$

Also, due to our definition of the quadrupolar moment vector (instead of $\overline{Q}$ tensor) $\mathbf{Q} = 2Q_{xy}, 2Q_{xz}, 2Q_{yz}, Q_{xx}, Q_{yy}$, the rows 7, 8 and 9 in α^S are divided by 2. Finally, we factor out ϵ_0 so that the plotted quantity has units of volume and can be directly compared for various particle volumes.

A.4 Far-Field radiated power by a single pyramid

Here we provide further calculations to prove that the unbalanced top-bottom emission directivity can be achieved by a single pyramid in free space, without coupling to a symmetry-breaking half-plane substrate or high index surroundings. In Fig. A.3(a) we plot the far-field scattering pattern of our pyramidal antenna (light gray structure in Fig. A.2) for different excitations. The source is a single dipole positioned in the vicinity of the pyramid. For the red curves, the dipole is positioned 25 nm above the top surface of the pyramid. For the black curves, it is positioned 25 nm below the bottom surface of the pyramid. The left panel corresponds to an in-plane dipole, while the right panel corresponds to a vertically aligned dipole, as shown in the corresponding insets. In both cases, the driving dipole has a wavelength of 660 nm. The radiated power is evaluated in the far-field, at 100 μm from the center of the antenna ($\sim$ 200 wavelengths away). The unbalanced emission in both cases indicates that selectively positioning emitters, as it was done in the experiment, yields an unbalanced top-bottom emission directivity.

In Fig. A.3(b) we analyze the modification of the radiative local density of optical states (LDOS) due to the pyramid. For this purpose, we integrate the radiated power into the top half sphere ρ_t, or the bottom half sphere ρ_b only, while considering for both cases the three different cartesian orientations of dipoles positioned around the pyramid. Dividing by ρ_0 — the free space radiative LDOS — we get the LDOS modification. These calculations where done with a home-written surface integral method based on the algorithm developed by A. Kern and O. Martin [237]. In Fig. A.3(c,d,e) we plot the top-bottom difference in LDOS enhancement, $(\rho_t - \rho_b)/\rho_0$, with respect to the free-space LDOS ρ_0. Therein, we observe that for both in-plane and out-of-plane dipoles radiation is enhanced towards the bottom. Not surprisingly, the effect is the same when all dipoles are considered, as shown in Fig. A.3(e). This behavior is in agreement with the greater emission enhancement towards the bottom at the LSPR wavelength in our experiments. The presence of these effects for a single pyramid in the homogenous medium excludes the stratified medium as being at the origin of the pronounced top-bottom emission asymmetry at the LSPR wavelength. However, spectral modifications and different intensities could indeed be expected in the presence of interfaces.

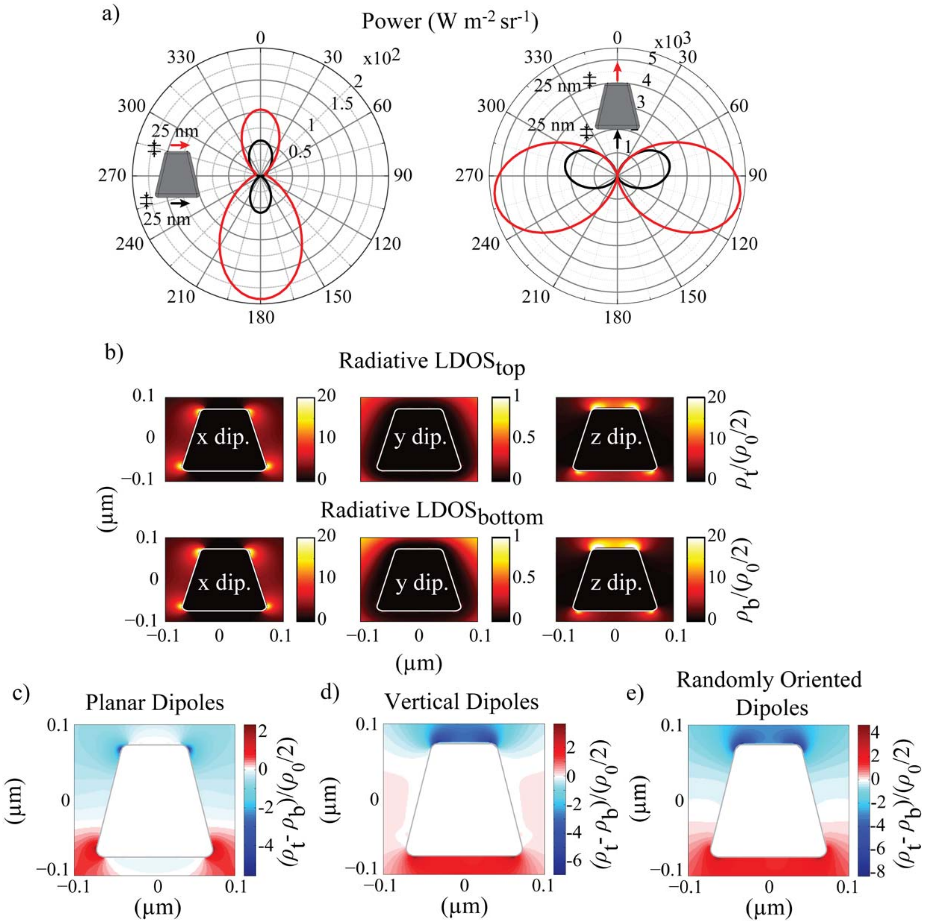

Figure A.3: (a) Radiation pattern for an electric dipole positioned above (red line) or below (black line) the pyramid, and oriented parallel (left panel) or perpendicular (right panel) to the top and bottom facets of the pyramid. The dipoles are located 25 nm from the top and bottom facets of the pyramid, as shown in the insets. (b) Top and bottom directed radiative local density of optical states (LDOS), ρ_t and ρ_b respectively, for x, y and z oriented dipoles near the pyramid, normalized to the free-space LDOS ρ_0. The top-bottom difference in LDOS enhancement, $(\rho_t - \rho_b)/\rho_0$, with respect to the free-space LDOS ρ_0, is shown for planar dipoles in (c). This graph shows that a horizontal dipole radiates more efficiently towards the bottom if positioned on top of the pyramid, or towards the top if positioned under the pyramid. (d) and (e) show a similar analysis for vertical and randomly oriented dipoles, respectively.

APPENDIX B

TIME-RESOLVED EMISSION OF QUANTUM DOTS ON A METALLIC NANOPARTICLE ARRAY

Throughout this thesis we showed that hybrid plasmonic-photonic modes in metallic nanoparticle arrays can modify the emission spectrum, directionality, and polarization of luminescent layers. An important question concerns whether the array also modifies the spontaneous emission rate, i.e. the probability per unit time that an excited state spontaneously relaxes to the ground state via the emission of a photon. In this appendix, we present measurements indicating that the answer to this question is negative. The experimental results in this appendix hold for a single resonant system, but the discussion is of a general character. We begin by reviewing the fundamentals, and we proceed to highlight a series of relevant points to consider in time-resolved photoluminescence studies involving ensembles of emitters coupled to extended modes in resonant structures. Finally, we present our experimental findings and compare these to a recent paper where a similar system was studied.

B.1 Background

Consider a two-level system with initial and final states labeled as i and f, respectively. When the coupling between the emitter and the radiation field is weak, Fermi's Golden rule gives the spontaneous emission rate:

$$\Gamma = \frac{2\pi}{\hbar} \sum_{f} \left| \langle f | \hat{H}_I | i \rangle \right|^2 \delta(\omega_i - \omega_f). \tag{B.1}$$

$\hat{H}_I$ is the interaction Hamiltonian, which in the dipole approximation is $\hat{H}_I = -\hat{\boldsymbol{\mu}} \cdot \hat{\mathbf{E}}$ with $\hat{\boldsymbol{\mu}}$ the dipole moment operator and $\hat{\mathbf{E}}$ the electric field operator. The δ-function selects the emitted photon energy on the basis of energy conservation: the difference in energy between the initial and final state of the emitter equals the photon energy.

Now consider a continuum of final states, each one having the same energy difference with the initial state but different wave vector **k**. In this case, it can be shown that the spontaneous emission rate is given by [238]

$$\Gamma = \frac{\pi\omega}{3\hbar\epsilon_0}|\boldsymbol{\mu}|^2 \rho_\mu(\mathbf{r},\omega), \tag{B.2}$$

where we have introduced the quantity ρ_μ known as the local density of optical states (LDOS) [239]. The LDOS counts the number of states to which an emitter at position **r** and with dipole moment $\boldsymbol{\mu}$ can decay via the emission of a photon with frequency ω.

It was Purcell who first noted that the spontaneous emission rate is not an inherent property of the emitter [7], but rather depends on the environment. In particular, Purcell realized that by coupling an emitter to a resonator, the spontaneous emission rate can be enhanced with respect to emission rate in free-space. The enhancement factor, known as the Purcell factor, is given by

$$F_p = \frac{3}{4\pi^2}\frac{Q}{V}\lambda^3, \tag{B.3}$$

where Q is the quality factor of the resonator, V is the mode's volume, and λ is the radiation wavelength. [1]

Present day nanophotonics research devotes significant efforts to the design of structures with high Q/V, which are expected to increase the Purcell factor [240]. Although an increase in Q usually comes with an increase in V (implying a trade-off for enhancing the Purcell effect), recent proposals have shown that certain systems may overcome this limitation [241–243]. Examples in this thesis of the general relation between Q and V are LSPRs which have low Q and low V, and diffracted or guided modes which have high Q and high V. As a word of caution, Koenderink noted that the Purcell factor may be inadequate as a quantitative figure of merit for the spontaneous emission rate of an emitter coupled to a plasmonic antenna [244]. This inadequacy stems from the strong dissipative character of plasmonic antennas, and the presence of more than one mode in the spectral region under consideration.

For experiments aimed at the observation of a modified spontaneous emission rate, the spectral properties of the emitters also need to be considered. In particular, the mechanism by which their spectral linewidths are broadened is a decisive factor for observing frequency-dependent lifetime changes in time-resolved photoluminescence experiments [245]. Organic dye molecules, such as those used in Chapters 3.3 and 4, typically

---

[1] The Purcell effect modifies the spontaneous emission rate via the LDOS term, ρ_μ, in Eq. B.2. In general, the dipole moment $\boldsymbol{\mu}$ does not need to be modified by the coupling to the resonator. This is due to the different length scales over which the dipole moment and the LDOS vary. The dipole moment is influenced within the length scale of the emitter's wave function, which is typically 1 Å - 1 nm, depending on the emitter. In contrast, the LDOS is typically influenced within length scales comparable to the effective wavelength. For visible light in free-space this is roughly 400 – 700 nm, but for resonant systems with deep sub-wavelength excitations [e.g. localized surface plasmon resonances (LSPRs) in metallic nanoparticles] the LDOS can vary over much shorter scales, e.g. ~ 10 nm.

have a homogeneously broadened spectrum. By homogeneous broadening we mean that all of the molecules in a statistical ensemble can emit radiation of any frequency within the fluorescence bandwidth. In the organic molecules, this bandwidth is due to the manifold of vibrational states comprising their electronic structure. As a consequence of this homogeneous broadening, the spontaneous emission rate of fluorescent molecules typically displays a negligible dependence on the emission frequency. In contrast, inorganic colloidal quantum dots as used in Chapters 2 and 6 have an inhomogeneously broadened spectrum. Each quantum dot in an ensemble displays a spectrally sharp excitonic transition giving a narrow emission linewidth. However, the variation in size of the quantum dots comprising the colloid leads to a spectral linewidth for the ensemble that is much broader than the linewidth of the individual quantum dots. As a consequence, the quantum dot ensemble emission typically displays a frequency variation in the spontaneous emission rate that follows the LDOS.

The significance of the linewidth broadening mechanism for observing changes in the spontaneous emission rate is determined by the spectral sharpness of the resonance to which the emitter couples. LSPRs have linewidths on the order of 100 nm, which are comparable to the linewidths of organic molecules. It is likely that for this reason, a good spectral and spatial overlap between LSPRs in metallic nanoparticles and molecular excitations in organic dyes has resulted in strong modifications of the spontaneous emission rate [48]. In contrast, surface lattice resonances (Chapter 2 and 5) and waveguide-plasmon polaritons (Chapter 3) can have much narrower spectral linewidths (1-10 nm). The influence of such narrow resonances on the spontaneous emission rate of organic dye molecules is likely to be “washed out”, because only a small fraction of the molecular manifold will be affected by the coupling to the resonator. For this reason, in this section we study the spontaneous emission of colloidal quantum dots which are well known to display spectrally narrow homogeneous emission linewidths (much narrower than the optical resonance linewidths of the array).

In relation to the theory, we should bear in mind that Fermi’s golden rule describes the time evolution of a single emitter. In contrast, we will present statistical measurements for an ensemble of emitters. These two scenarios can be equated by assuming ergodicity. Light emitters are good examples of ergodic systems [246], where time averages equal ensemble averages. An important point to consider in ensemble measurements is that the position $\mathbf{r}$ and the orientation of the dipole moment $\boldsymbol{\mu}$ of the emitters vary randomly throughout the excited volume. Therefore, position and orientation averaging of the LDOS in this volume is expected.

B.2 Experiments

In what follows, we present a time-resolved study of spontaneous emission under the influence of the standard resonant system studied in this thesis. We investigate a periodic array of aluminum nanodisks covered by a 420 ± 20 nm layer of polystyrene doped with CdSe/CdS core/shell quantum dots. The ensemble quantum dot emission peaks at wavelength of 590 nm, has a full width at half maximum of 25 nm, and was embedded at a low

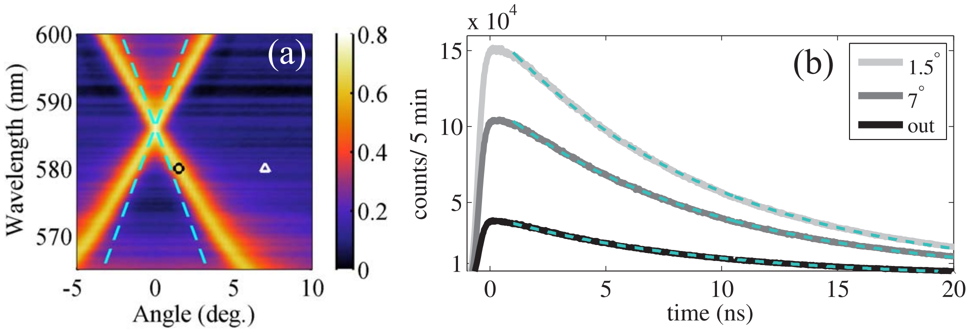

Figure B.1: (a) Measured extinction spectra of an aluminum nanoparticle array covered by a 420 nm layer of polystyrene doped with CdSe/CdS quantum dots. The blue dashed lines indicated the dispersion of the fundamental TM_0 guided mode in the polystyrene layer. (b) Time-resolved photoluminescence measurements at 580 ± 5 nm of the emitting layer in (a). The light and dark gray lines are the emission of the quantum dots in the presence of the metallic nanoparticle array, with the detector located at 1.5° [black circle in (a)] and at 7° [white triangle in (a)], respectively. The black line is the emission of the quantum dots out of the influence of the metallic nanoparticle array. The dashed cyan lines overplotted with the measurements are monoexponential fits.

concentration of 1 μM with the polystyrene[2]. The quantum efficiency of the quantum dot colloid in toluene was measured to be 50%. The aluminum nanodisks have a height of 150 ± 10 nm, a diameter of 130 ± 20 nm, and are arranged in a square lattice with constant $a = 390$ nm. The array is similar to the one investigated in Chapter 3.3, the only difference being a slightly larger lattice constant here (by 20 nm).

Figure B.1(a) shows variable angle light extinction measurements of the sample discussed above. We measured the transmittance through the array of a collimated (angular spread $< 0.1°$) and TM-polarized light beam from a halogen lamp. The angle of incidence was varied using a computer-controlled rotation stage with an angular resolution of 0.2°. We define the extinction as $1 - T_0$, with T_0 the zeroth-order transmittance. In Fig. B.1(a), the extinction is shown in color as a function of the incident angle and wavelength. The dashed lines overplotted with the measurements are calculations of the fundamental TM_0 guided mode dispersion coupled via the first diffracted orders. As in Chapter 3, these are calculated using the formalism described by Yariv and Yeh [57], considering a dielectric slab with refractive index $n_p = 1.58$ (polystyrene), sandwiched between semi-infinite media with $n_a = 1.0$ (air) and $n_g = 1.44$ (glass). The thickness of the slab, 420 ± 20 nm, was determined by profilometry measurements. We attribute the dispersive peaks in extinction close to the dispersion of the TM_0 guided mode to quasi-guided modes. These resonances arise from the coupling of the TM_0 guided mode to the LSPRs in the aluminum nanodisks.

Time-resolved measurements of the quantum dot photoluminescence with and without the array were done with a time-correlated single photon counting setup (Picoquant Gmbh). The quantum dots were excited by a pulsed laser with a central wavelength of

---

[2] This low concentration was selected to reduce inasmuch as possible energy transfer between the quantum dots.

450 nm, a time duration of 200 ps, and an intensity of 0.1 W/cm^2 at the sample. The photoluminescence was collected by a fiber mounted on a rotating arm, and was spectrally filtered by a bandpass filter at 580 ± 5 nm. Only TM-polarized light was selected by a polarization analyzer in the collection path. Figure B.1(b) shows the time-resolved emission for the sample discussed above, collected at two different angles. For the light gray line, the detector was placed at 1.5°, which is in resonance with the quasi-guided mode. For the dark gray line, the detector was placed at 7°, which is out of any resonance of the system. These detected wavelength-angle points — determined by the spectral filter and the collection angle — are indicated by the circle and triangle in Fig. B.1(a). The black line in Fig. B.1(b) is a measurement of the same quantum dot layer but in the absence of the metallic nanoparticle array.

We analyze the data by fitting the measured intensity with a monoexponential function of the form $I(t) = Ae^{-t/\tau}$. The dashed cyan lines in Fig. B.1(b) are the fits, from which we retrieve the emission lifetime τ and the constant A. Inside the array, detecting in resonance at 1.5° we find $\tau_{res} = 9.39 \pm 0.02$, and out of resonance at 7° we find $\tau_{nores} = 9.47 \pm 0.02$. Outside the array we find $\tau_{out} = 9.02 \pm 0.03$. The uncertainties represent 2σ confidence intervals on the fits. The fitted values indicate that the emission lifetime does not significantly depend on the collection angle, and there is only a small difference with respect to the value outside the array. We believe that the increased emission lifetime inside the array (of roughly 0.4 ns) is within the edge of the total experimental uncertainty, including the intrument's precision and spatial variations of both the quantum dot layer and the metallic nanoparticles. Therefore, we consider that the emission lifetime is essentially unmodified by the array or the detection angle.

From the fits we also retrieve the constant A, which represents the intensity at $t = 0$, i.e. $I(0)$. The fitted value of $I(0)$ is not exactly equal to the measured intensity at $t = 0$ because the fit starts slightly after (at $t = 1$ ns). Between $t = 0$ and $t = 1$ ns the decay rate is actually slightly slower for an unknown reason, [3] and we therefore ignore this time span. Inside the array, collecting on-resonance at 1.5° we find $A_{res} = 1.66 \cdot 10^5$, and out-of-resonance at 7° we find $A_{nores} = 1.15 \cdot 10^5$. Outside the array we find $A_{out} = 0.41 \cdot 10^5$. All errors (not quoted) are in the third digit after the decimal or beyond. We attribute variations in A to a combination of processes at both the excitation and emission wavelengths. Comparing the dark gray line to the black line in Fig. B.1(b), we observe that even in the absence of any resonance at the collected emission wavelength and angle, A is enhanced by the presence of the metallic nanoparticle array. We attribute this to an enhanced excitation of the quantum dots due to scattering of the pump light by the metallic nanoparticles. Comparing the light and dark gray lines shows that A is further enhanced when the collection angle matches a resonance at the emitted wavelength.

The above results suggest that the metallic nanoparticle array enhances the quantum dot emission intensity at certain wavelengths and angles, but the decay rate [4] remains mostly unchanged. This finding can be regarded from two different viewpoints: On the

---

[3] This is possibly an experimental artifact due to the time resolution of the instrument, which is on the order of a few hundred picoseconds.

[4] Time-resolved photoluminescence measurements are sensitive to the total decay rate, which includes both radiative and non-radiative relaxation.

one hand, the results in Fig. B.1(b) give little hope of modifying the spontaneous emission rate with surface lattice resonances, quasi-guided modes, or waveguide-plasmon polaritons. On the other hand, the unmodified decay rate indicates that the average internal quantum efficiency (QE) of the ensemble of emitters remains unaltered by the presence of the array. This finding has important consequences for applications in solid-state lighting, where it is desired to have a mechanism by which light of different colors is beamed into different directions without introducing losses. In this case, a negligible modification of the total decay rate implies that the introduction of the metallic nanoparticle arrays does not quench the total emitted intensity, as it could be expected due to the presence of non-radiative decay channels into the metal [9]. We emphasize that this conclusion pertains only to the internal QE, and not to the external QE. The internal QE considers the fraction of emitted photons per excited emitters. The external QE considers the fraction of emitted photons per incident photons. These two quantities can mutually differ because the metallic nanoparticles can absorb, and not only scatter, the pump light. Such a process will degrade the external QE, but the internal QE [to which the results in Fig. B.1(b) relate] would remain intact.

The interpretation so far should be taken with some caveats, because the spontaneous emission rate only reflects LDOS enhancements for high QE emitters [247]. In general, emitters can be classified as being constant power or constant amplitude sources [248]. For organic dyes, this classification has a connection with the QE: low QE molecules are constant amplitude sources (CAS), while high QE molecules are constant power sources (CPS). For a CPS, the spontaneous emission rate is indicative of the LDOS, and the total radiated power scales with the pump rate. In contrast, for a CAS the emission power is sensitive to the LDOS, but the total decay rate is not because it is dominated by non-radiative relaxation. Unfortunately for the present discussion, the extension of this classification to colloidal quantum dots is non-trivial. Input-output power measurements of a quantum dot ensemble, as performed here and in many other works in the literature, measure an ensemble average. These measurements are affected by variations in the quantum dots constituting the excited ensemble, some of which may be bright and others dark. To assess whether a certain source is best classified as CPS or CAS one needs the internal quantum efficiency instead. As an outlook for the future, this could be measured, for example, by the technique introduced by Lunneman and co-workers [249], which is in the spirit of the seminal experiment by Drexhage [11].

To finalize this appendix, let us now elaborate on the significance of performing time-resolved measurements at different collection angles. The authors of Ref. [49] claim that the radiative relaxation rate of a quantum dot ensemble deposited on a metallic nanoparticle array is greater when detected at a wavelength, angle, and polarization that corresponds to a maximum in extinction measurements. Figure B.2 is a reproduction of the key figure in Ref. [49]. It shows that when the detector is placed at 50° off the normal, and collects p-polarization but not s-polarization, the PL dynamics displays an initial acceleration. This acceleration is attributed to a surface plasmon mode in the array, which overlaps with the quantum dot emission only at at 50° and for p-polarization.

It is known from the work of Drexhage that the spontaneous emission rate depends on the projection of the emitter's dipole moment with the electric field (polarization) at the

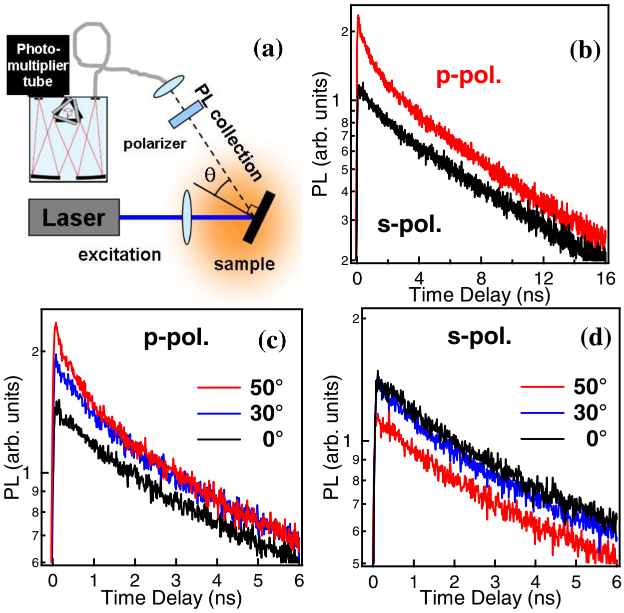

Figure B.2: Reprinted with permission from Yikuan Wang, Tianyu Yang, Mark T. Tuominen, and Marc Achermann, Physical Review Letters, 102, 163001 (2009). Copyright 2009 by the American Physical Society. `http://link.aps.org/doi/10.1103/PhysRevLett.102.163001`. Readers may view, browse, and/or download material for temporary copying purposes only, provided these uses are for noncommercial personal purposes. Except as provided by law, this material may not be further reproduced, distributed, transmitted, modified, adapted, performed, displayed, published, or sold in whole or part, without prior written permission from the American Physical Society.

transition frequency [11]. The novel element in the above claim is that the spontaneous emission rate depends on the collection angle. At first glance, an angular dependent emission rate seems incompatible with Fermi's Golden rule because the LDOS is a wave vector (and therefore angle) integrated quantity. Therefore, the spontaneous emission rate is a measure of the total power radiated by the emitter into any direction. This element of the theory seems to have been ignored in Ref. [49], where the total emission rate was argued to be proportional to the electric field enhancement at the position of the emitters due to a *single* resonant plane wave (no integration over all wave vectors). There is, however, an important point raised by the authors of Ref. [49] which could explain the observed angular dependence of the decay rate: At each angle the detector receives light from different emitters. This is due to the extended nature of the source, which includes a multitude of quantum dots each having a dipole moment with a different projection onto the surface plasmon modes at different wavelengths, angles, and polarization. We interpret this condition not as a dependence of *the* spontaneous emission rate on the angle. Instead, at different angles the detector receives light from spatially separated emitters

[$\rho = \rho(\mathbf{r})$] which have different decay rates.

In view of the above results we embarked upon trying to measure any possible angular dependence of the detected quantum dot decay rate. As the measurements in Fig. B.1(b) show, no clear angular dependence was found here. Our findings are perhaps surprising when compared to those in Ref. [49], since here we employ much higher quality factors Q, have a higher signal to noise ratio, and we have a more dilute quantum dot layer allowing us to more safely exclude interactions amongst the quantum dots themselves. In contrast, our quantum dot layer is much thicker (400 nm instead of a quantum dot monolayer), and this is certainly an important factor which may give rise to differences. Therefore, we do not regard our results to be in contradiction with those in Ref. [49] because there are important differences between the two experiments. However, from these results we learn that time-resolved studies involving ensembles of emitters contain a multitude of parameters that need to be well controlled and accounted for in order to make quantitative conclusions about how metallic nanoparticle arrays modify the spontaneous emission rates.

B.3 Conclusions

To conclude, we believe that the dependence of the detected decay rate on the collection angle is potentially an intriguing effect which deserves further attention. So far, we are unaware of demonstrations by other groups (besides the one in Ref. [49]) showing resonance-induced angular dependent decay rates. Our finding of a marginally modified quantum dot decay rate is nevertheless not a discouraging one. In particular, solid-state lighting applications may profit from the directional color beaming rendered by metallic nanoparticle arrays which do not degrade the quantum efficiency of the emitters.

REFERENCES

[1] J. S. Toll, *Causality and the Dispersion Relation: Logical Foundations,* Phys. Rev. **104**, 1760 (1956).

[2] H. A. Lorentz, *The theory of electrons and its applications to the phenomena of light and radiant heat,* Leipzig : B.G. Teubner, New York : G.E. Stechert, 1916.

[3] L. Allen and J. H. Eberly, *Optical Resonance and Two-Level Atoms,* Dover Pub, New York, 1987.

[4] S. A. Maier, *Plasmonics: Fundamentals and Applications,* Springer, New York, USA, 2007.

[5] G. Mie, *Beiträge zur Optik trüber Medien, speziell kolloidaler Metallösungen,* Annalen der Physik **330**, 377 (1908).

[6] C. F. Bohren and D. Huffman, *Absorption and scattering of light by small particles,* Wiley, 1983.

[7] *Proceedings of the American Physical Society,* Phys. Rev. **69**, 674 (1946).

[8] J. Gersten and A. Nitzan, *Electromagnetic theory of enhanced Raman scattering by molecules adsorbed on rough surfaces,* J. Chem. Phys. **73** (1980).

[9] D. A. Weitz, S. Garoff, J. I. Gersten, and A. Nitzan, *The enhancement of Raman scattering, resonance Raman scattering, and fluorescence from molecules adsorbed on a rough silver surface,* J. Chem. Phys. **78**, 5324 (1983).

[10] P. Aravind, A. Nitzan, and H. Metiu, *The interaction between electromagnetic resonances and its role in spectroscopic studies of molecules adsorbed on colloidal particles or metal spheres,* Surf. Sci. **110**, 189 (1981).

[11] K. Drexhage, *Influence of a dielectric interface on fluorescence decay time,* J. Lumin. **1**, 693 (1970).

[12] W. L. Barnes, *Fluorescence near interfaces: The role of photonic mode density,* J. Mod. Opt. **45**, 661 (1998).

[13] W. L. Barnes, A. Dereux, and T. W. Ebbesen, *Surface plasmon subwavelength optics,* Nature (London) **424**, 824 (2003).

[14] W. H. Weber and C. F. Eagen, *Energy transfer from an excited dye molecule to the surface plasmons of an adjacent metal,* Opt. Lett. **4**, 236 (1979).

[15] I. Pockrand, A. Brillante, and D. Möbius, *Nonradiative decay of excited molecules near a metal surface,* Chem. Phys. Lett. **69**, 499 (1980).

[16] H. Knobloch, H. Brunner, A. Leitner, F. Aussenegg, and W. Knoll, *Probing the evanescent field of propagating plasmon surface polaritons by fluorescence and Raman spectroscopies,* J. Chem. Phys. **98** (1993).

[17] R. M. Amos and W. L. Barnes, *Modification of the spontaneous emission rate of ions close to a thin metal mirror,* Phys. Rev. B **55**, 7249 (1997).

[18] T. W. Ebbesen, H. J. Lezec, H. F. Ghaemi, Thio, and P. A. Wolff, *Extraordinary optical transmission through sub-wavelength hole arrays,* Nature (London) **391**, 667 (1998).

[19] H. A. Bethe, *Theory of Diffraction by Small Holes,* Phys. Rev. **66**, 163 (1944).

[20] L. Martín-Moreno, F. J. García-Vidal, H. J. Lezec, K. M. Pellerin, T. Thio, J. B. Pendry, and T. W. Ebbesen, *Theory of Extraordinary Optical Transmission through Subwavelength Hole Arrays,* Phys. Rev. Lett. **86**, 1114 (2001).

[21] K. J. K. Koerkamp, S. Enoch, F. B. Segerink, N. F. van Hulst, and L. Kuipers, *Strong Influence of Hole Shape on Extraordinary Transmission through Periodic Arrays of Subwavelength Holes,* Phys. Rev. Lett. **92**, 183901 (2004).

[22] J. Bravo-Abad, A. Degiron, F. Przybilla, C. Genet, F. Garcia-Vidal, L. Martin-Moreno, and T. Ebbesen, *How light emerges from an illuminated array of subwavelength holes,* Nature Phys. **2**, 120 (2006).

[23] F. J. García de Abajo, *Colloquium: Light scattering by particle and hole arrays,* Rev. Mod. Phys. **79**, 1267 (2007).

[24] F. J. Garcia-Vidal, L. Martin-Moreno, T. W. Ebbesen, and L. Kuipers, *Light passing through subwavelength apertures,* Rev. Mod. Phys. **82**, 729 (2010).

[25] F. J. García de Abajo, R. Gómez-Medina, and J. J. Sáenz, *Full transmission through perfect-conductor subwavelength hole arrays,* Phys. Rev. E **72**, 016608 (2005).

[26] M. Born and E. Wolf, *Principles of Optics: Electromagnetic Theory of Propagation, Interference and Diffraction of Light,* Cambridge University Press, 1999.

[27] M. Sarrazin, J.-P. Vigneron, and J.-M. Vigoureux, *Role of Wood anomalies in optical properties of thin metallic films with a bidimensional array of subwavelength holes,* Phys. Rev. B **67**, 085415 (2003).

[28] C. Genet, M. van Exter, and J. Woerdman, *Fano-type interpretation of red shifts and red tails in hole array transmission spectra,* Opt. Commun. **225**, 331 (2003).

[29] U. Fano, *Effects of Configuration Interaction on Intensities and Phase Shifts,* Phys. Rev. **124**, 1866 (1961).

[30] B. Luk'yanchuk, N. I. Zheludev, S. A. Maier, N. J. Halas, P. Nordlander, H. Giessen, and C. T. Chong, *The Fano resonance in plasmonic nanostructures and metamaterials,* Nature Mater. **9**, 707 (2010).

[31] A. E. Miroshnichenko, S. Flach, and Y. S. Kivshar, *Fano resonances in nanoscale structures,* Rev. Mod. Phys. **82**, 2257 (2010).

[32] V. Giannini, Y. Francescato, H. Amrania, C. C. Phillips, and S. A. Maier, *Fano Resonances in Nanoscale Plasmonic Systems: A Parameter-Free Modeling Approach,* Nano Lett. **11**, 2835 (2011).

[33] P. Mühlschlegel, H.-J. Eisler, O. J. F. Martin, B. Hecht, and D. W. Pohl, *Resonant Optical Antennas,* Science **308**, 1607 (2005).

[34] J.-J. Greffet, *Nanoantennas for Light Emission,* Science **308**, 1561 (2005).

[35] J. N. Farahani, D. W. Pohl, H.-J. Eisler, and B. Hecht, *Single Quantum Dot Coupled to a Scanning Optical Antenna: A Tunable Superemitter,* Phys. Rev. Lett. **95**, 017402 (2005).

[36] P. Anger, P. Bharadwaj, and L. Novotny, *Enhancement and Quenching of Single-Molecule Fluorescence,* Phys. Rev. Lett. **96**, 113002 (2006).

[37] S. Kühn, U. Håkanson, L. Rogobete, and V. Sandoghdar, *Enhancement of Single-Molecule Fluorescence Using a Gold Nanoparticle as an Optical Nanoantenna,* Phys. Rev. Lett. **97**, 017402 (2006).

[38] P. Bharadwaj, B. Deutsch, and L. Novotny, *Optical Antennas,* Adv. Opt. Photon. **1**, 438 (2009).

[39] L. Novotny and N. van Hulst, *Antennas for light,* Nature Photon. **5**, 83 (2011).

[40] R. P. Feynman, *There's plenty of room at the bottom,* Presented at the 1959 Annual Meeting of the American Physical Society at the California Institute of Technology (Caltech), 1959.

[41] L. Novotny, *Effective Wavelength Scaling for Optical Antennas,* Phys. Rev. Lett. **98**, 266802 (2007).

[42] T. H. Taminiau, F. D. Stefani, F. B. Segerink, and N. F. van Hulst, *Optical antennas direct single-molecule emission,* Nature Photon. **2**, 234 (2008).

[43] A. G. Curto, G. Volpe, T. H. Taminiau, M. P. Kreuzer, R. Quidant, and N. F. van Hulst, *Unidirectional Emission of a Quantum Dot Coupled to a Nanoantenna,* Science **329** (2010).

[44] T. Coenen, E. J. R. Vesseur, A. Polman, and A. F. Koenderink, *Directional Emission from Plasmonic Yagi-Uda Antennas Probed by Angle-Resolved Cathodoluminescence Spectroscopy,* Nano Lett. **11**, 3779 (2011).

[45] T. Coenen, F. Bernal Arango, A. F. Koenderink, and A. Polman, *Directional emission from a single plasmonic scatterer,* Nat. Commun. **5**, null (2014).

[46] H. Mertens, J. S. Biteen, H. A. Atwater, and A. Polman, *Polarization-Selective Plasmon-Enhanced Silicon Quantum-Dot Luminescence,* Nano Lett. **6**, 2622 (2006).

[47] T. Ming, L. Zhao, Z. Yang, H. Chen, L. Sun, J. Wang, and C. Yan, *Strong Polarization Dependence of Plasmon-Enhanced Fluorescence on Single Gold Nanorods,* Nano Lett. **9**, 3896 (2009).

[48] O. L. Muskens, V. Giannini, J. A. Sánchez-Gil, and J. Gomez Rivas, *Strong Enhancement of the Radiative Decay Rate of Emitters by Single Plasmonic Nanoantennas,* Nano Lett. **7**, 2871 (2007).

[49] Y. Wang, T. Yang, M. T. Tuominen, and M. Achermann, *Radiative Rate Enhancements in Ensembles of Hybrid Metal-Semiconductor Nanostructures,* Phys. Rev. Lett. **102**, 163001 (2009).

[50] J. S. Biteen, N. S. Lewis, H. A. Atwater, H. Mertens, and A. Polman, *Spectral tuning of plasmon-enhanced silicon quantum dot luminescence,* Appl. Phys. Lett. **88**, (2006).

[51] M. Ringler, A. Schwemer, M. Wunderlich, A. Nichtl, K. Kürzinger, T. A. Klar, and J. Feldmann, *Shaping Emission Spectra of Fluorescent Molecules with Single Plasmonic Nanoresonators,* Phys. Rev. Lett. **100**, 203002 (2008).

[52] R. W. Wood, *On a Remarkable Case of Uneven Distribution of Light in a Diffraction Grating Spectrum,* Proc. Phys. Soc. London **18**, 269 (1902).

[53] L. Rayleigh, *III. Note on the remarkable case of diffraction spectra described by Prof. Wood,* Philos. Mag. Series 6 **14**, 60 (1907).

[54] L. Rayleigh, *On the Dynamical Theory of Gratings,* Proc. R. Soc. A **79**, 399 (1907).

[55] F. Bloch, *Über die Quantenmechanik der Elektronen in Kristallgittern,* Zeitschrift für Physik **52**, 555 (1929).

[56] G. Floquet, *Sur les équations différentielles linéaires à coefficients périodiques,* Ann. Sci. Ec. Norm. Sup. **3**, 181 (1884).

[57] A. Yariv and P. Yeh, *Photonics: Optical Electronics in Modern Communications*, Oxford University Press, Oxford, 6 edition, 2007.

[58] A. Christ, S. G. Tikhodeev, N. A. Gippius, J. Kuhl, and H. Giessen, *Waveguide-Plasmon Polaritons: Strong Coupling of Photonic and Electronic Resonances in a Metallic Photonic Crystal Slab*, Phys. Rev. Lett. **91**, 183901 (2003).

[59] S. R. K. Rodriguez, S. Murai, M. A. Verschuuren, and J. G. Rivas, *Light-Emitting Waveguide-Plasmon Polaritons*, Phys. Rev. Lett. **109**, 166803 (2012).

[60] M. Kerker, D.-S. Wang, and C. L. Giles, *Electromagnetic scattering by magnetic spheres*, J. Opt. Soc. Am. **73**, 765 (1983).

[61] H. Lochbihler, *Surface polaritons on gold-wire gratings*, Phys. Rev. B **50**, 4795 (1994).

[62] W. L. Barnes, T. W. Preist, S. C. Kitson, and J. R. Sambles, *Physical origin of photonic energy gaps in the propagation of surface plasmons on gratings*, Phys. Rev. B **54**, 6227 (1996).

[63] S. C. Kitson, W. L. Barnes, and J. R. Sambles, *Full Photonic Band Gap for Surface Modes in the Visible*, Phys. Rev. Lett. **77**, 2670 (1996).

[64] A. Krishnan, T. Thio, T. Kim, H. Lezec, T. Ebbesen, P. Wolff, J. Pendry, L. Martin-Moreno, and F. Garcia-Vidal, *Evanescently coupled resonance in surface plasmon enhanced transmission*, Opt. Commun. **200**, 1 (2001).

[65] C. Sauvan, C. Billaudeau, S. Collin, N. Bardou, F. Pardo, J.-L. Pelouard, and P. Lalanne, *Surface plasmon coupling on metallic film perforated by two-dimensional rectangular hole array*, Appl. Phys. Lett. **92**, 011125 (2008).

[66] C. Billaudeau, S. Collin, C. Sauvan, N. Bardou, F. Pardo, and J.-L. Pelouard, *Angle-resolved transmission measurements through anisotropic two-dimensional plasmonic crystals*, Opt. Lett. **33**, 165 (2008).

[67] C. Ropers, D. J. Park, G. Stibenz, G. Steinmeyer, J. Kim, D. S. Kim, and C. Lienau, *Femtosecond Light Transmission and Subradiant Damping in Plasmonic Crystals*, Phys. Rev. Lett. **94**, 113901 (2005).

[68] K. G. Lee and Q.-H. Park, *Coupling of Surface Plasmon Polaritons and Light in Metallic Nanoslits*, Phys. Rev. Lett. **95**, 103902 (2005).

[69] T. A. Kelf, Y. Sugawara, J. J. Baumberg, M. Abdelsalam, and P. N. Bartlett, *Plasmonic Band Gaps and Trapped Plasmons on Nanostructured Metal Surfaces*, Phys. Rev. Lett. **95**, 116802 (2005).

[70] I. Sersic, M. Frimmer, E. Verhagen, and A. F. Koenderink, *Electric and Magnetic Dipole Coupling in Near-Infrared Split-Ring Metamaterial Arrays*, Phys. Rev. Lett. **103**, 213902 (2009).

[71] R. Taubert, D. Dregely, T. Stroucken, A. Christ, and H. Giessen, *Octave-wide photonic band gap in three-dimensional plasmonic Bragg structures and limitations of radiative coupling,* Nat. Commun. **3** (2012).

[72] K. T. Carron, W. Fluhr, M. Meier, A. Wokaun, and H. W. Lehmann, *Resonances of two-dimensional particle gratings in surface-enhanced Raman scattering,* J. Opt. Soc. Am. B **3**, 430 (1986).

[73] S. Zou, N. Janel, and G. C. Schatz, *Silver nanoparticle array structures that produce remarkably narrow plasmon lineshapes*, J. Chem. Phys. **120**, 10871 (2004).

[74] S. Zou and G. C. Schatz, *Narrow plasmonic/photonic extinction and scattering line shapes for one and two dimensional silver nanoparticle arrays,* J. Chem. Phys. **121**, 12606 (2004).

[75] E. M. Hicks, S. Zou, G. C. Schatz, K. G. Spears, R. P. Van Duyne, L. Gunnarsson, T. Rindzevicius, B. Kasemo, and M. Käll, *Controlling Plasmon Line Shapes through Diffractive Coupling in Linear Arrays of Cylindrical Nanoparticles Fabricated by Electron Beam Lithography,* Nano Lett. **5**, 1065 (2005).

[76] Y. Chu, E. Schonbrun, T. Yang, and K. B. Crozier, *Experimental observation of narrow surface plasmon resonances in gold nanoparticle arrays,* Appl. Phys. Lett. **93**, 181108 (2008).

[77] B. Auguié and W. L. Barnes, *Collective Resonances in Gold Nanoparticle Arrays,* Phys. Rev. Lett. **101**, 143902 (2008).

[78] V. G. Kravets, F. Schedin, and A. N. Grigorenko, *Extremely Narrow Plasmon Resonances Based on Diffraction Coupling of Localized Plasmons in Arrays of Metallic Nanoparticles,* Phys. Rev. Lett. **101**, 087403 (2008).

[79] G. Vecchi, V. Giannini, and J. Gómez Rivas, *Surface modes in plasmonic crystals induced by diffractive coupling of nanoantennas,* Phys. Rev. B **80**, 201401 (2009).

[80] S. R. K. Rodriguez, A. Abass, B. Maes, O. T. A. Janssen, G. Vecchi, and J. Gómez Rivas, *Coupling Bright and Dark Plasmonic Lattice Resonances,* Phys. Rev. X **1**, 021019 (2011).

[81] W. Zhou and T. W. Odom, *Tunable subradiant lattice plasmons by out-of-plane dipolar interactions,* Nature Nanotech. **6**, 423 (2011).

[82] T. V. Teperik and A. Degiron, *Design strategies to tailor the narrow plasmon-photonic resonances in arrays of metallic nanoparticles,* Phys. Rev. B **86**, 245425 (2012).

[83] G. Weick, C. Woollacott, W. L. Barnes, O. Hess, and E. Mariani, *Dirac-like Plasmons in Honeycomb Lattices of Metallic Nanoparticles,* Phys. Rev. Lett. **110**, 106801 (2013).

[84] A. Vitrey, L. Aigouy, P. Prieto, J. M. García-Martín, and M. U. González, *Parallel Collective Resonances in Arrays of Gold Nanorods,* Nano Lett. **14**, 2079 (2014).

[85] S. Rodriguez, M. Schaafsma, A. Berrier, and J. G. Rivas, *Collective resonances in plasmonic crystals: Size matters,* Physica B **407**, 4081 (2012).

[86] G. Vecchi, V. Giannini, and J. Gómez Rivas, *Shaping the Fluorescent Emission by Lattice Resonances in Plasmonic Crystals of Nanoantennas,* Phys. Rev. Lett. **102**, 146807 (2009).

[87] G. Pellegrini, G. Mattei, and P. Mazzoldi, *Nanoantenna Arrays for Large-Area Emission Enhancement,* J. Phys. Chem. C **115**, 24662 (2011).

[88] S. R. K. Rodriguez, G. Lozano, M. A. Verschuuren, R. Gomes, K. Lambert, B. D. Geyter, A. Hassinen, D. V. Thourhout, Z. Hens, and J. G. Rivas, *Quantum rod emission coupled to plasmonic lattice resonances: A collective directional source of polarized light,* Appl. Phys. Lett. **100**, 111103 (2012).

[89] T. V. Teperik and A. Degiron, *Superradiant Optical Emitters Coupled to an Array of Nanosize Metallic Antennas,* Phys. Rev. Lett. **108**, 147401 (2012).

[90] G. Lozano, D. J. Louwers, S. R.K. Rodriguez, S. Murai, O. T. Jansen, M. A. Verschuuren, and J. Gomez Rivas, *Plasmonics for solid-state lighting: enhanced excitation and directional emission of highly efficient light sources,* Light Sci. Appl. **2**, e66 (2013).

[91] W. Zhou, M. Dridi, J. Y. Suh, C. H. Kim, D. T. Co, M. R. Wasielewski, G. C. Schatz, and T. W. Odom, *Lasing action in strongly coupled plasmonic nanocavity arrays,* Nature Nanotech. **8**, 506 (2013).

[92] P. Offermans, M. C. Schaafsma, S. R. K. Rodriguez, Y. Zhang, M. Crego-Calama, S. H. Brongersma, and J. Gómez Rivas, *Universal Scaling of the Figure of Merit of Plasmonic Sensors,* ACS Nano **5**, 5151 (2011).

[93] B. Špačková and J. Homola, *Sensing properties of lattice resonances of 2D metal nanoparticle arrays: An analytical model,* Opt. Express **21**, 27490 (2013).

[94] B. Auguié, X. M. Bendaña, W. L. Barnes, and F. J. García de Abajo, *Diffractive arrays of gold nanoparticles near an interface: Critical role of the substrate,* Phys. Rev. B **82**, 155447 (2010).

[95] E. Palik, *Handbook of optical constants of solids,* Academic Press, New York, 1985.

[96] A. Abass, S. R.-K. Rodriguez, J. Gómez Rivas, and B. Maes, *Tailoring Dispersion and Eigenfield Profiles of Plasmonic Surface Lattice Resonances,* ACS Photon. **1**, 61 (2014).

[97] R. H. Dicke, *Coherence in Spontaneous Radiation Processes,* Phys. Rev. **93**, 99 (1954).

[98] S. R. K. Rodriguez, O. T. A. Janssen, G. Lozano, A. Omari, Z. Hens, and J. G. Rivas, *Near-field resonance at far-field-induced transparency in diffractive arrays of plasmonic nanorods,* Opt. Lett. **38**, 1238 (2013).

[99] R. J. P. Engelen, D. Mori, T. Baba, and L. Kuipers, *Subwavelength Structure of the Evanescent Field of an Optical Bloch Wave,* Phys. Rev. Lett. **102**, 023902 (2009).

[100] M. A. Verschuuren, *Substrate Conformal Imprint Lithography for Nanophotonics,* PhD dissertation, Utrecht University, 2010.

[101] A. Wokaun, H.-P. Lutz, A. P. King, U. P. Wild, and R. R. Ernst, *Energy transfer in surface enhanced luminescence,* J. Chem. Phys. **79**, 509 (1983).

[102] L. Carbone, C. Nobile, M. De Giorgi, F. D. Sala, G. Morello, P. Pompa, M. Hytch, E. Snoeck, A. Fiore, I. R. Franchini, M. Nadasan, A. F. Silvestre, L. Chiodo, S. Kudera, R. Cingolani, R. Krahne, and L. Manna, *Synthesis and Micrometer-Scale Assembly of Colloidal CdSe/CdS Nanorods Prepared by a Seeded Growth Approach,* Nano Lett. **7**, 2942 (2007).

[103] A. V. Shchegrov, K. Joulain, R. Carminati, and J.-J. Greffet, *Near-Field Spectral Effects due to Electromagnetic Surface Excitations,* Phys. Rev. Lett. **85**, 1548 (2000).

[104] G. W. Bryant, F. J. Garcia de Abajo, and J. Aizpurua, *Mapping the Plasmon Resonances of Metallic Nanoantennas,* Nano Lett. **8**, 631 (2008).

[105] B. M. Ross and L. P. Lee, *Comparison of near- and far-field measures for plasmon resonance of metallic nanoparticles,* Opt. Lett. **34**, 896 (2009).

[106] V. Giannini, G. Vecchi, and J. Gómez Rivas, *Lighting Up Multipolar Surface Plasmon Polaritons by Collective Resonances in Arrays of Nanoantennas,* Phys. Rev. Lett. **105**, 266801 (2010).

[107] K.-J. Boller, A. Imamoglu, and S. E. Harris, *Observation of electromagnetically induced transparency,* Phys. Rev. Lett. **66**, 2593 (1991).

[108] S. Zhang, D. A. Genov, Y. Wang, M. Liu, and X. Zhang, *Plasmon Induced Transparency in Metamaterials,* Phys. Rev. Lett. **101**, 047401 (2008).

[109] N. Liu, L. Langguth, T. Weiss, J. Kästel, M. Fleischhauer, T. Pfau, and H. Giessen, *Plasmonic analogue of electromagnetically induced transparency at the Drude damping limit,* Nature Mater. **8**, 758 (2009).

[110] P. Tassin, L. Zhang, T. Koschny, E. N. Economou, and C. M. Soukoulis, *Low-Loss Metamaterials Based on Classical Electromagnetically Induced Transparency,* Phys. Rev. Lett. **102**, 053901 (2009).

[111] T. Zentgraf, S. Zhang, R. F. Oulton, and X. Zhang, *Ultranarrow coupling-induced transparency bands in hybrid plasmonic systems,* Phys. Rev. B **80**, 195415 (2009).

[112] V. Yannopapas, E. Paspalakis, and N. V. Vitanov, *Electromagnetically induced transparency and slow light in an array of metallic nanoparticles,* Phys. Rev. B **80**, 035104 (2009).

[113] S. Mukherjee, H. Sobhani, J. B. Lassiter, R. Bardhan, P. Nordlander, and N. J. Halas, *Fanoshells: Nanoparticles with Built-in Fano Resonances*, Nano Lett. **10**, 2694 (2010).

[114] R. D. Kekatpure, E. S. Barnard, W. Cai, and M. L. Brongersma, *Phase-Coupled Plasmon-Induced Transparency*, Phys. Rev. Lett. **104**, 243902 (2010).

[115] J. Zhang, L. Cai, W. Bai, and G. Song, *Hybrid waveguide-plasmon resonances in gold pillar arrays on top of a dielectric waveguide*, Opt. Lett. **35**, 3408 (2010).

[116] J. Zhang, W. Bai, L. Cai, Y. Xu, G. Song, and Q. Gan, *Observation of ultra-narrow band plasmon induced transparency based on large-area hybrid plasmon-waveguide systems*, Appl. Phys. Lett. **99**, 181120 (2011).

[117] S. N. Sheikholeslami, A. García-Etxarri, and J. A. Dionne, *Controlling the Interplay of Electric and Magnetic Modes via Fano-like Plasmon Resonances*, Nano Lett. **11**, 3927 (2011).

[118] P. Alonso-Gonzalez, M. Schnell, P. Sarriugarte, H. Sobhani, C. Wu, N. Arju, A. Khanikaev, F. Golmar, P. Albella, L. Arzubiaga, F. Casanova, L. E. Hueso, P. Nordlander, G. Shvets, and R. Hillenbrand, *Real-Space Mapping of Fano Interference in Plasmonic Metamolecules*, Nano Lett. **11**, 3922 (2011).

[119] M. Frimmer, T. Coenen, and A. F. Koenderink, *Signature of a Fano Resonance in a Plasmonic Metamolecule's Local Density of Optical States*, Phys. Rev. Lett. **108**, 077404 (2012).

[120] F. Hao, Y. Sonnefraud, P. V. Dorpe, S. A. Maier, N. J. Halas, and P. Nordlander, *Symmetry Breaking in Plasmonic Nanocavities: Subradiant LSPR Sensing and a Tunable Fano Resonance*, Nano Lett. **8**, 3983 (2008).

[121] F. Neubrech, A. Pucci, T. W. Cornelius, S. Karim, A. García-Etxarri, and J. Aizpurua, *Resonant Plasmonic and Vibrational Coupling in a Tailored Nanoantenna for Infrared Detection*, Phys. Rev. Lett. **101**, 157403 (2008).

[122] C. Weisbuch, M. Nishioka, A. Ishikawa, and Y. Arakawa, *Observation of the coupled exciton-photon mode splitting in a semiconductor quantum microcavity*, Phys. Rev. Lett. **69**, 3314 (1992).

[123] J. Bellessa, C. Bonnand, J. C. Plenet, and J. Mugnier, *Strong Coupling between Surface Plasmons and Excitons in an Organic Semiconductor*, Phys. Rev. Lett. **93**, 036404 (2004).

[124] J. Dintinger, S. Klein, F. Bustos, W. L. Barnes, and T. W. Ebbesen, *Strong coupling between surface plasmon-polaritons and organic molecules in subwavelength hole arrays*, Phys. Rev. B **71**, 035424 (2005).

[125] P. Vasa, R. Pomraenke, S. Schwieger, Y. I. Mazur, V. Kunets, P. Srinivasan, E. Johnson, J. E. Kihm, D. S. Kim, E. Runge, G. Salamo, and C. Lienau, *Coherent Exciton–Surface-Plasmon-Polariton Interaction in Hybrid Metal-Semiconductor Nanostructures*, Phys. Rev. Lett. **101**, 116801 (2008).

[126] A. Manjavacas, F. Garcia de Abajo, and P. Nordlander, *Quantum Plexcitonics: Strongly Interacting Plasmons and Excitons*, Nano Lett. **11**, 2318 (2011).

[127] T. Schwartz, J. A. Hutchison, C. Genet, and T. W. Ebbesen, *Reversible Switching of Ultrastrong Light-Molecule Coupling*, Phys. Rev. Lett. **106**, 196405 (2011).

[128] A. González-Tudela, P. A. Huidobro, L. Martín-Moreno, C. Tejedor, and F. J. García-Vidal, *Theory of Strong Coupling between Quantum Emitters and Propagating Surface Plasmons*, Phys. Rev. Lett. **110**, 126801 (2013).

[129] A. I. Väkeväinen, R. J. Moerland, H. T. Rekola, A.-P. Eskelinen, J.-P. Martikainen, D.-H. Kim, and P. Törmä, *Plasmonic Surface Lattice Resonances at the Strong Coupling Regime*, Nano Lett. **14**, 1721 (2014).

[130] J. A. Hutchison, T. Schwartz, C. Genet, E. Devaux, and T. W. Ebbesen, *Modifying Chemical Landscapes by Coupling to Vacuum Fields*, Angew. Chem. Int. Ed. **51**, 1592 (2012).

[131] J. A. Hutchison, A. Liscio, T. Schwartz, A. Canaguier-Durand, C. Genet, V. Palermo, P. Samorì, and T. W. Ebbesen, *Tuning the Work-Function Via Strong Coupling*, Adv. Mater. **25**, 2481 (2013).

[132] S. Murai, M. A. Verschuuren, G. Lozano, G. Pirruccio, A. F. Koenderink, and J. Gomez Rivas, *Enhanced absorption and emission of Y3Al5O12:Ce3+ thin layers prepared by epoxide-catalyzed sol-gel method*, Opt. Mater. Express **2**, 1111 (2012).

[133] J. P. Marangos, *Electromagnetically induced transparency*, J. Mod. Opt. **45**, 471 (1998).

[134] M. Fleischhauer, A. Imamoglu, and J. P. Marangos, *Electromagnetically induced transparency: Optics in coherent media*, Rev. Mod. Phys. **77**, 633 (2005).

[135] A. Alù and N. Engheta, *Cloaking a Sensor*, Phys. Rev. Lett. **102**, 233901 (2009).

[136] F. J. G. de Abajo, *Seeing without being seen*, Physics **2**, 47 (2009).

[137] C. L. G. Alzar, M. A. G. Martinez, and P. Nussenzveig, *Classical analog of electromagnetically induced transparency*, Am. J. Phys. **70**, 37 (2002).

[138] L. Novotny, *Strong coupling, energy splitting, and level crossings: A classical perspective*, Am. J. Phys. **78**, 1199 (2010).

[139] J. Zuloaga and P. Nordlander, *On the Energy Shift between Near-Field and Far-Field Peak Intensities in Localized Plasmon Systems*, Nano Lett. **11**, 1280 (2011).

[140] M. Février, P. Gogol, A. Aassime, R. Mégy, C. Delacour, A. Chelnokov, A. Apuzzo, S. Blaize, J.-M. Lourtioz, and B. Dagens, *Giant Coupling Effect between Metal Nanoparticle Chain and Optical Waveguide*, Nano Lett. **12**, 1032 (2012).

[141] F. Bernal Arango, A. Kwadrin, and A. F. Koenderink, *Plasmonic Antennas Hybridized with Dielectric Waveguides*, ACS Nano **6**, 10156 (2012).

[142] B. C. Buchler, T. Kalkbrenner, C. Hettich, and V. Sandoghdar, *Measuring the Quantum Efficiency of the Optical Emission of Single Radiating Dipoles Using a Scanning Mirror*, Phys. Rev. Lett. **95**, 063003 (2005).

[143] P. Alonso-González, P. Albella, F. Neubrech, C. Huck, J. Chen, F. Golmar, F. Casanova, L. E. Hueso, A. Pucci, J. Aizpurua, and R. Hillenbrand, *Experimental Verification of the Spectral Shift between Near- and Far-Field Peak Intensities of Plasmonic Infrared Nanoantennas*, Phys. Rev. Lett. **110**, 203902 (2013).

[144] M. Hentschel, M. Saliba, R. Vogelgesang, H. Giessen, A. P. Alivisatos, and N. Liu, *Transition from Isolated to Collective Modes in Plasmonic Oligomers*, Nano Lett. **10**, 2721 (2010).

[145] V. Savona, L. Andreani, P. Schwendimann, and A. Quattropani, *Quantum well excitons in semiconductor microcavities: Unified treatment of weak and strong coupling regimes*, Solid State Commun. **93**, 733 (1995).

[146] L. Li, *Formulation and comparison of two recursive matrix algorithms for modeling layered diffraction gratings*, J. Opt. Soc. Am. A **13**, 1024 (1996).

[147] V. Liu and S. Fan, *S^4 : A free electromagnetic solver for layered periodic structures*, Comput. Phys. Commun. **183**, 2233 (2012).

[148] L. Li, *Use of Fourier series in the analysis of discontinuous periodic structures*, J. Opt. Soc. Am. A **13**, 1870 (1996).

[149] D. J. Bergman and M. I. Stockman, *Surface Plasmon Amplification by Stimulated Emission of Radiation: Quantum Generation of Coherent Surface Plasmons in Nanosystems*, Phys. Rev. Lett. **90**, 027402 (2003).

[150] M. Noginov, G. Zhu, A. M. Belgrave, R. Bakker, V. M. Shalaev, E. E. Narimanov, S. Stout, E. Herz, T. Suteewong, and U. Wiesner, *Demonstration of a spaser-based nanolaser*, Nature (London) **460**, 1110 (2009).

[151] R. F. Oulton, V. J. Sorger, T. Zentgraf, R.-M. Ma, C. Gladden, L. Dai, G. Bartal, and X. Zhang, *Plasmon lasers at deep subwavelength scale*, Nature (London) **461**, 629 (2009).

[152] O. Hess, J. B. Pendry, S. A. Maier, R. F. Oulton, J. M. Hamm, and K. L. Tsakmakidis, *Active nanoplasmonic metamaterials*, Nature Mater. **11**, 573 (2012).

[153] F. van Beijnum, P. J. van Veldhoven, E. J. Geluk, M. J. A. de Dood, G. W. 't Hooft, and M. P. van Exter, *Surface Plasmon Lasing Observed in Metal Hole Arrays*, Phys. Rev. Lett. **110**, 206802 (2013).

[154] T. K. Hakala, J. J. Toppari, A. Kuzyk, M. Pettersson, H. Tikkanen, H. Kunttu, and P. Törmä, *Vacuum Rabi Splitting and Strong-Coupling Dynamics for Surface-Plasmon Polaritons and Rhodamine 6G Molecules*, Phys. Rev. Lett. **103**, 053602 (2009).

[155] Y. Sugawara, T. A. Kelf, J. J. Baumberg, M. E. Abdelsalam, and P. N. Bartlett, *Strong Coupling between Localized Plasmons and Organic Excitons in Metal Nanovoids*, Phys. Rev. Lett. **97**, 266808 (2006).

[156] N. I. Cade, T. Ritman-Meer, and D. Richards, *Strong coupling of localized plasmons and molecular excitons in nanostructured silver films*, Phys. Rev. B **79**, 241404 (2009).

[157] S. R. K. Rodriguez, J. Feist, M. A. Verschuuren, F. J. Garcia Vidal, and J. Gómez Rivas, *Thermalization and Cooling of Plasmon-Exciton Polaritons: Towards Quantum Condensation*, Phys. Rev. Lett. **111**, 166802 (2013).

[158] S. Rodriguez and J. G. Rivas, *Surface lattice resonances strongly coupled to Rhodamine 6G excitons: tuning the plasmon-exciton-polariton mass and composition*, Opt. Express **21**, 27411 (2013).

[159] H. Deng, G. Weihs, C. Santori, J. Bloch, and Y. Yamamoto, *Condensation of Semiconductor Microcavity Exciton Polaritons*, Science **298**, 199 (2002).

[160] J. Kasprzak, M. Richard, S. Kundermann, A. Baas, P. Jeambrun, J. M. J. Keeling, F. M. Marchetti, M. H. Szymańska, R. André, J. L. Staehli, V. Savona, P. B. Littlewood, B. Deveaud, and L. S. Dang, *Bose-Einstein condensation of exciton polaritons*, Nature (London) **443**, 409 (2006).

[161] R. Balili, V. Hartwell, D. Snoke, L. Pfeiffer, and K. West, *Bose-Einstein Condensation of Microcavity Polaritons in a Trap*, Science **316**, 1007 (2007).

[162] R. Houdré, R. P. Stanley, and M. Ilegems, *Vacuum-field Rabi splitting in the presence of inhomogeneous broadening: Resolution of a homogeneou s linewidth in an inhomogeneously broadened system*, Phys. Rev. A **53**, 2711 (1996).

[163] I. Diniz, S. Portolan, R. Ferreira, J. M. Gérard, P. Bertet, and A. Auffèves, *Strongly coupling a cavity to inhomogeneous ensembles of emitters: Potential for long-lived solid-state quantum memories*, Phys. Rev. A **84**, 063810 (2011).

[164] M. H. Anderson, J. R. Ensher, M. R. Matthews, C. E. Wieman, and E. A. Cornell, *Observation of Bose-Einstein Condensation in a Dilute Atomic Vapor*, Science **269**, 198 (1995).

[165] K. B. Davis, M. O. Mewes, M. R. Andrews, N. J. van Druten, D. S. Durfee, D. M. Kurn, and W. Ketterle, *Bose-Einstein Condensation in a Gas of Sodium Atoms,* Phys. Rev. Lett. **75**, 3969 (1995).

[166] H. Deng, H. Haug, and Y. Yamamoto, *Exciton-polariton Bose-Einstein condensation,* Rev. Mod. Phys. **82**, 1489 (2010).

[167] J. J. Hopfield, *Theory of the Contribution of Excitons to the Complex Dielectric Constant of Crystals,* Phys. Rev. **112**, 1555 (1958).

[168] N. Moiseyev, *Non-Hermitian quantum mechanics,* Cambridge University Press, 2011.

[169] P. Vasa, R. Pomraenke, G. Cirmi, E. De Re, W. Wang, S. Schwieger, D. Leipold, E. Runge, G. Cerullo, and C. Lienau, *Ultrafast Manipulation of Strong Coupling in Metal-Molecular Aggregate Hybrid Nanostructures,* ACS Nano **4**, 7559 (2010).

[170] P. Vasa, W. Wang, R. Pomraenke, M. Lammers, M. Maiuri, C. Manzoni, G. Cerullo, and C. Lienau, *Real-time observation of ultrafast Rabi oscillations between excitons and plasmons in metal nanostructures with J-aggregates,* Nature Photon. **7**, 128 (2013).

[171] R. Houdré, J. L. Gibernon, P. Pellandini, R. P. Stanley, U. Oesterle, C. Weisbuch, J. O'Gorman, B. Roycroft, and M. Ilegems, *Saturation of the strong-coupling regime in a semiconductor microcavity: Free-carrier bleaching of cavity polaritons,* Phys. Rev. B **52**, 7810 (1995).

[172] R. Butté, G. Delalleau, A. I. Tartakovskii, M. S. Skolnick, V. N. Astratov, J. J. Baumberg, G. Malpuech, A. Di Carlo, A. V. Kavokin, and J. S. Roberts, *Transition from strong to weak coupling and the onset of lasing in semiconductor microcavities,* Phys. Rev. B **65**, 205310 (2002).

[173] S. Kéna-Cohen and S. R. Forrest, *Room-temperature polariton lasing in an organic single-crystal microcavity,* Nature Photon. **4**, 371 (2010).

[174] A. Imamoglu, R. J. Ram, S. Pau, and Y. Yamamoto, *Nonequilibrium condensates and lasers without inversion: Exciton-polariton lasers,* Phys. Rev. A **53**, 4250 (1996).

[175] M. H. Szymańska, J. Keeling, and P. B. Littlewood, *Nonequilibrium Quantum Condensation in an Incoherently Pumped Dissipative System,* Phys. Rev. Lett. **96**, 230602 (2006).

[176] D. Bajoni, P. Senellart, A. Lemaitre, and J. Bloch, *Photon lasing in GaAs microcavity: Similarities with a polariton condensate,* Phys. Rev. B **76**, 201305 (2007).

[177] J. Kasprzak, D. D. Solnyshkov, R. André, L. S. Dang, and G. Malpuech, *Formation of an Exciton Polariton Condensate: Thermodynamic versus Kinetic Regimes,* Phys. Rev. Lett. **101**, 146404 (2008).

[178] I. Carusotto and C. Ciuti, *Quantum fluids of light,* Rev. Mod. Phys. **85**, 299 (2013).

[179] T. Elsaesser and W. Kaiser, *Vibrational and Vibronic Relaxation of Large Polyatomic Molecules in Liquids,* Annu. Rev. Phys. Chem. **42**, 83 (1991).

[180] T. Schwartz, J. A. Hutchison, J. Léonard, C. Genet, S. Haacke, and T. W. Ebbesen, *Polariton Dynamics under Strong LightMolecule Coupling,* Chem. Phys. Chem. **14**, 125 (2013).

[181] A. I. Tartakovskii, M. Emam-Ismail, R. M. Stevenson, M. S. Skolnick, V. N. Astratov, D. M. Whittaker, J. J. Baumberg, and J. S. Roberts, *Relaxation bottleneck and its suppression in semiconductor microcavities,* Phys. Rev. B **62**, R2283 (2000).

[182] J. Klaers, J. Schmitt, F. Vewinger, and M. Weitz, *Bose-Einstein condensation of photons in an optical microcavity,* Nature (London) **468**, 545 (2010).

[183] Y. Lu and A. Penzkofer, *Absorption behaviour of methanolic rhodamine 6G solutions at high concentration,* Chem. Phys. **107**, 175 (1986).

[184] J. D. Plumhof, T. Stöferle, U. Mai, L.and Scherf, and R. Mahrt, Nature Mater. **13**, 247 (2013).

[185] K. Daskalakis, S. A. Maier, R. Murray, and S. Kéna-Cohen, *Nonlinear interactions in an organic polariton condensate,* Nature Mater. **13**, 271 (2014).

[186] J. Pendry, A. J. Holden, D. J. Robbins, and W. J. Stewart, *Magnetism from conductors and enhanced nonlinear phenomena,* IEEE Trans. Microwave Theory Tech. **47**, 2075 (1999).

[187] D. R. Smith, W. J. Padilla, D. C. Vier, S. C. Nemat-Nasser, and S. Schultz, *Composite Medium with Simultaneously Negative Permeability and Permittivity,* Phys. Rev. Lett. **84**, 4184 (2000).

[188] R. A. Shelby, D. R. Smith, and S. Schultz, *Experimental Verification of a Negative Index of Refraction,* Science **292**, 77 (2001).

[189] V. M. Shalaev, *Optical negative-index metamaterials,* Nature Photon. **1**, 41 (2007).

[190] E. Verhagen, R. de Waele, L. Kuipers, and A. Polman, *Three-Dimensional Negative Index of Refraction at Optical Frequencies by Coupling Plasmonic Waveguides,* Phys. Rev. Lett. **105**, 223901 (2010).

[191] J. B. Pendry, *Negative Refraction Makes a Perfect Lens,* Phys. Rev. Lett. **85**, 3966 (2000).

[192] N. Fang, H. Lee, C. Sun, and X. Zhang, *Sub-Diffraction-Limited Optical Imaging with a Silver Superlens,* Science **308**, 534 (2005).

[193] S. Kawata, Y. Inouye, and P. Verma, *Plasmonics for near-field nano-imaging and superlensing,* Nature Photon. **3**, 388 (2009).

[194] D. Schurig, J. J. Mock, B. J. Justice, S. A. Cummer, J. B. Pendry, A. F. Starr, and D. R. Smith, *Metamaterial Electromagnetic Cloak at Microwave Frequencies,* Science **314**, 977 (2006).

[195] T. Ergin, N. Stenger, P. Brenner, J. B. Pendry, and M. Wegener, *Three-Dimensional Invisibility Cloak at Optical Wavelengths,* Science **328**, 337 (2010).

[196] M. Husnik, M. W. Klein, N. Feth, M. Konig, J. Niegemann, K. Busch, S. Linden, and M. Wegener, *Absolute extinction cross-section of individual magnetic split-ring resonators,* Nature Photon. **2**, 614 (2008).

[197] C. Rockstuhl, C. Menzel, S. Mühlig, J. Petschulat, C. Helgert, C. Etrich, A. Chipouline, T. Pertsch, and F. Lederer, *Scattering properties of meta-atoms,* Phys. Rev. B **83**, 245119 (2011).

[198] I. Sersic, C. Tuambilangana, T. Kampfrath, and A. F. Koenderink, *Magnetoelectric point scattering theory for metamaterial scatterers,* Phys. Rev. B **83**, 245102 (2011).

[199] M. Husnik, S. Linden, R. Diehl, J. Niegemann, K. Busch, and M. Wegener, *Quantitative Experimental Determination of Scattering and Absorption Cross-Section Spectra of Individual Optical Metallic Nanoantennas,* Phys. Rev. Lett. **109**, 233902 (2012).

[200] P. Lunnemann, I. Sersic, and A. F. Koenderink, *Optical properties of two-dimensional magnetoelectric point scattering lattices,* Phys. Rev. B **88**, 245109 (2013).

[201] I. M. Hancu, A. G. Curto, M. Castro-López, M. Kuttge, and N. F. van Hulst, *Multipolar Interference for Directed Light Emission,* Nano Lett. **14**, 166 (2014).

[202] F. Bernal Arango, T. Coenen, and A. F. Koenderink, *Underpinning Hybridization Intuition for Complex Nanoantennas by Magnetoelectric Quadrupolar Polarizability Retrieval,* ACS Photon. **1**, 444 (2014).

[203] A. García-Etxarri, R. Gómez-Medina, L. S. Froufe-Pérez, C. López, L. Chantada, F. Scheffold, J. Aizpurua, M. Nieto-Vesperinas, and J. J. Sáenz, *Strong magnetic response of submicron Silicon particles in the infrared,* Opt. Express **19**, 4815 (2011).

[204] J. Geffrin, B. García Cámara, R. Gómez-Medina, P. Albella, L. Froufe-Pérez, C. Eyraud, A. Litman, R. Vaillon, F. González, M. Nieto-Vesperinas, J. Sáenz, and F. Moreno, *Magnetic and electric coherence in forward- and back-scattered electromagnetic waves by a single dielectric subwavelength sphere,* Nat. Commun. **3**, 1171.

[205] S. Person, M. Jain, Z. Lapin, J. J. Sáenz, G. Wicks, and L. Novotny, *Demonstration of Zero Optical Backscattering from Single Nanoparticles,* Nano Lett. **13**, 1806 (2013).

[206] I. Staude, A. E. Miroshnichenko, M. Decker, N. T. Fofang, S. Liu, E. Gonzales, J. Dominguez, T. S. Luk, D. N. Neshev, I. Brener, and Y. Kivshar, *Tailoring Directional*

Scattering through Magnetic and Electric Resonances in Subwavelength Silicon Nanodisks, ACS Nano **7**, 7824 (2013).

[207] A. Alu and N. Engheta, *How does zero forward-scattering in magnetodielectric nanoparticles comply with the optical theorem?,* J. Nanophotonics **4**, 041590 (2010).

[208] S. K. Rodriguez, F. Bernal, T. Steinbusch, M. Verschuuren, and J. Koenderink, A.F. Gómez Rivas, *Breaking the symmetry of forward-backward light emission with localized and collective resonances in magnetoelectric nanopyramid arrays,* submitted.

[209] R. Carminati, M. Nieto-Vesperinas, and J.-J. Greffet, *Reciprocity of evanescent electromagnetic waves,* J. Opt. Soc. Am. A **15**, 706 (1998).

[210] B. Rolly, B. Stout, and N. Bonod, *Boosting the directivity of optical antennas with magnetic and electric dipolar resonant particles,* Opt. Express **20**, 20376 (2012).

[211] S. Zou and G. C. Schatz, *Silver nanoparticle array structures that produce giant enhancements in electromagnetic fields,* Chem. Phys. Lett. **403**, 62 (2005).

[212] P. Jin, M. Tazawa, and G. Xu, *Reversible tuning of surface plasmon resonance of silver nanoparticles using a thermochromic matrix,* J. Appl. Phys. **99**, 096106 (2006).

[213] S. Olcum, A. Kocabas, G. Ertas, A. Atalar, and A. Aydinli, *Tunable surface plasmon resonance on an elastomeric substrate,* Opt. Express **17**, 8542 (2009).

[214] J. Beeckman, K. Neyts, and P. J. M. Vanbrabant, *Liquid-crystal photonic applications,* Opt. Eng. **50**, 081202 (2011).

[215] C. Lumdee, S. Toroghi, and P. G. Kik, *Post-fabrication Voltage Controlled Resonance Tuning of Nanoscale Plasmonic Antennas,* ACS Nano **6**, 6301 (2012).

[216] I. V. Shadrivov, P. V. Kapitanova, S. I. Maslovski, and Y. S. Kivshar, *Metamaterials Controlled with Light,* Phys. Rev. Lett. **109**, 083902 (2012).

[217] J. Müller, C. Sönnichsen, H. von Poschinger, G. von Plessen, T. A. Klar, and J. Feldmann, *Electrically controlled light scattering with single metal nanoparticles,* Appl. Phys. Lett. **81**, 171 (2002).

[218] P. A. Kossyrev, A. Yin, S. G. Cloutier, D. A. Cardimona, D. Huang, P. M. Alsing, and J. M. Xu, *Electric Field Tuning of Plasmonic Response of Nanodot Array in Liquid Crystal Matrix,* Nano Lett. **5**, 1978 (2005).

[219] K. C. Chu, C. Y. Chao, Y. F. Chen, Y. C. Wu, and C. C. Chen, *Electrically controlled surface plasmon resonance frequency of gold nanorods,* Appl. Phys. Lett. **89**, (2006).

[220] P. R. Evans, G. A. Wurtz, W. R. Hendren, R. Atkinson, W. Dickson, A. V. Zayats, and R. J. Pollard, *Electrically switchable nonreciprocal transmission of plasmonic nanorods with liquid crystal,* Appl. Phys. Lett. **91**, 043101 (2007).

[221] W. Dickson, G. A. Wurtz, P. R. Evans, R. J. Pollard, and A. V. Zayats, *Electronically Controlled Surface Plasmon Dispersion and Optical Transmission through Metallic Hole Arrays Using Liquid Crystal,* Nano Lett. **8**, 281 (2008).

[222] S. Xiao, U. K. Chettiar, A. V. Kildishev, V. Drachev, I. C. Khoo, and V. M. Shalaev, *Tunable magnetic response of metamaterials,* Appl. Phys. Lett. **95**, (2009).

[223] M. Dridi and A. Vial, *FDTD Modeling of Gold Nanoparticles in a Nematic Liquid Crystal: Quantitative and Qualitative Analysis of the Spectral Tunability,* J. Phys. Chem. C **114**, 9541 (2010).

[224] S. Khatua, W.-S. Chang, P. Swanglap, J. Olson, and S. Link, *Active Modulation of Nanorod Plasmons,* Nano Lett. **11**, 3797 (2011).

[225] J. Li, Y. Ma, Y. Gu, I.-C. Khoo, and Q. Gong, *Large spectral tunability of narrow geometric resonances of periodic arrays of metallic nanoparticles in a nematic liquid crystal,* Appl. Phys. Lett. **98**, 213101 (2011).

[226] H. Li, S. Xu, Y. Gu, K. Wang, and W. Xu, *Active modulation of wavelength and radiation direction of fluorescence via liquid crystal-tuned surface plasmons,* Appl. Phys. Lett. **102**, 051107 (2013).

[227] C. Hu, T. Aubert, Y. Justo, S. Flamee, M. Cirillo, A. Gassenq, O. Drobchak, F. Beunis, G. Roelkens, and Z. Hens, *The micropatterning of layers of colloidal quantum dots with inorganic ligands using selective wet etching,* Nanotechnology **25**, 175302 (2014).

[228] S. Flamee, M. Cirillo, S. Abe, K. De Nolf, R. Gomes, T. Aubert, and Z. Hens, *Fast, High Yield, and High Solid Loading Synthesis of Metal Selenide Nanocrystals,* Chem. Mater. **25**, 2476 (2013).

[229] J. J. Li, Y. A. Wang, W. Guo, J. C. Keay, T. D. Mishima, M. B. Johnson, and X. Peng, *Large-Scale Synthesis of Nearly Monodisperse CdSe/CdS Core/Shell Nanocrystals Using Air-Stable Reagents via Successive Ion Layer Adsorption and Reaction,* J. Am. Chem. Soc. **125**, 12567 (2003).

[230] J. Li, C.-H. Wen, S. Gauza, R. Lu, and S.-T. Wu, *Refractive Indices of Liquid Crystals for Display Applications,* J. Display Technol. **1**, 51 (2005).

[231] J. Li, S.-T. Wu, S. Brugioni, R. Meucci, and S. Faetti, *Infrared refractive indices of liquid crystals,* J. Appl. Phys. **97**, 073501 (2005).

[232] A. Abass, S. Rahimzadeh-Kalaleh Rodriguez, T. Ako, M. Aubert, Tangi Verschuuren, D. Van Thourhout, J. Beeckman, Z. Hens, J. Gómez Rivas, and B. Maes, *Active Liquid Crystal Tuning of Plasmonic Enhanced Light Emission from Colloidal Quantum Dots,* submitted.

[233] S. Mühlig, C. Menzel, C. Rockstuhl, and F. Lederer, *Multipole analysis of meta-atoms,* Metamaterials **5**, 64 (2011).

[234] F. B. Arango and A. F. Koenderink, *Polarizability tensor retrieval for magnetic and plasmonic antenna design,* New J. Phys. **15**, 073023 (2013).

[235] A. Alù and N. Engheta, *Guided propagation along quadrupolar chains of plasmonic nanoparticles,* Phys. Rev. B **79**, 235412 (2009).

[236] I. Sersic, M. A. van de Haar, F. B. Arango, and A. F. Koenderink, *Ubiquity of Optical Activity in Planar Metamaterial Scatterers,* Phys. Rev. Lett. **108**, 223903 (2012).

[237] A. M. Kern and O. J. F. Martin, *Surface integral formulation for 3D simulations of plasmonic and high permittivity nanostructures,* J. Opt. Soc. Am. A **26**, 732 (2009).

[238] L. Novotny and B. Hecht, *Principles of Nano-Optics,* Cambridge University Press, 2011.

[239] R. Sprik, B. A. van Tiggelen, and A. Lagendijk, *Optical emission in periodic dielectrics,* Europhys. Lett. **35**, 265 (1996).

[240] M. Agio, *Optical antennas as nanoscale resonators,* Nanoscale **4**, 692 (2012).

[241] P. Lalanne and J.-P. Hugonin, *Bloch-wave engineering for high-Q, small-V microcavities,* IEEE J. Quant. Electron. **39**, 1430 (2003).

[242] J. Yao, X. Yang, X. Yin, G. Bartal, and X. Zhang, *Three-dimensional nanometer-scale optical cavities of indefinite medium,* Proc. Natl. Acad. Sci. U.S.A. **108**, 11327 (2011).

[243] X. Yang, J. Yao, J. Rho, X. Yin, and X. Zhang, *Experimental realization of three-dimensional indefinite cavities at the nanoscale with anomalous scaling laws,* Nature Photon. **4**, 450 (2012).

[244] A. F. Koenderink, *On the use of Purcell factors for plasmon antennas,* Opt. Lett. **35**, 4208 (2010).

[245] I. S. Nikolaev, P. Lodahl, and W. L. Vos, *Fluorescence Lifetime of Emitters with Broad Homogeneous Linewidths Modified in Opal Photonic Crystals,* J. Phys, Chem. C **112**, 7250 (2008).

[246] J. A. Veerman, M. F. Garcia-Parajo, L. Kuipers, and N. F. van Hulst, *Time-Varying Triplet State Lifetimes of Single Molecules,* Phys. Rev. Lett. **83**, 2155 (1999).

[247] A. Femius Koenderink, L. Bechger, A. Lagendijk, and W. L. Vos, *An experimental study of strongly modified emission in inverse opal photonic crystals,* Phys. Status Solidi A **197**, 648 (2003).

[248] R. G. S. El-Dardiry, S. Faez, and A. Lagendijk, *Classification of light sources and their interaction with active and passive environments,* Phys. Rev. A **83**, 031801 (2011).

[249] P. Lunnemann, F. T. Rabouw, R. J. A. van Dijk-Moes, F. Pietra, D. Vanmaekelbergh, and A. F. Koenderink, *Calibrating and Controlling the Quantum Efficiency Distribution of Inhomogeneously Broadened Quantum Rods by Using a Mirror Ball,* ACS Nano **7**, 5984 (2013).

COUPLING LIGHT AND MATTER IN METALLIC NANOPARTICLE ARRAYS:

SUMMARY

Advancing the current understanding of light-matter interactions is at the forefront of fundamental and applied physics. The advent of nanotechnology constitutes a milestone in this endeavour. Advanced nanofabrication and characterization methods have enabled humankind to create and observe fascinating phenomena that emerge when matter is structured on the length scale of its interaction with light: the nanoscale. This thesis brings together a number of experiments, and accompanying theoretical description, aimed at deepening the current understanding of how light behaves at the nanoscale. The system of choice is a periodic array of metallic nanoparticles. Emphasis is placed on the potential of this system for enhancing light emission. The investigations here presented were performed in the context of an industrial partnership program between FOM Institute AMOLF and Philips Research.

This thesis focuses on the observation of distinct optical resonances in the light extinction and emission spectra of periodic arrays of metallic nanoparticles. Experimental optical methods include angle and polarization resolved light extinction spectroscopy, photoluminescence spectroscopy and dynamics. Chemical methods were used for the fabrication of luminescent layers in the vicinity of metallic nanoparticle arrays. Numerical methods were employed to model wave propagation in complex nanophotonic systems. Further insight is obtained by means of analytical methods describing the interaction of multiple resonances in coupled systems. Given the variety of optical modes studied in this thesis, each chapter is devoted to the coupling between two or more of these modes with different properties. In this summary, we provide a brief description of each chapter, highlighting the main achievements and concluding with an outlook for the future.

Chapter 1 provides a general introduction to the coupling of light and matter. We begin with a discussion of the characteristic length and energy scales involved in this coupling. Since optical resonances permeate every chapter of this thesis, a general discussion of resonance conditions is here presented. We proceed to review some of the most significant contributions to the field of optical resonances in metallic nanoparticles, and arrays of such nanoparticles. In particular, we discuss localized surface plasmon resonances (LSPRs) associated with the collective oscillation of conduction electrons driven by the electromagnetic field. Metallic nanoparticles sustaining LSPRs can act as optical antennas, converting free-space radiation into localized energy and viceversa. We then explain the origin of diffracted and refractive index guided optical waves. The necessary conditions for the excitation of these waves in periodic arrays of metallic nanostructures are explained. Finally, we introduce the general properties of coupled modes, including their relation to the underlying bare modes.

In Chapter 2 we explore the coupling of LSPRs to Rayleigh anomalies (RAs), i.e. diffracted waves in the plane of a periodic array. This coupling leads to hybrid plasmonic-photonic collective resonances, known as surface lattice resonances (SLRs). We investigate the physics of SLRs in arrays of metallic nanoparticles with variable dimensions. All these arrays are embedded in a fully homogeneous dielectric medium, which simplifies the physics with respect to stratified media. Next, we cover a metallic nanoparticle array with a thin luminescent layer to demonstrate how SLRs can enhance the directionality and polarization of the emitted light.

In Chapter 3 we investigate the coupling of LSPRs to refractive index guided modes. First, we investigate a metallic nanoparticle array standing on a light-emitting slab waveguide. Signatures of strong coupling between LSPRs and guided modes are shown. We demonstrate that when the LSPR-guided mode frequency detuning is zero, the hybrid light-matter quasi-particle known as waveguide plasmon polariton (WPP) displays an extraordinarily enhanced light emission at frequencies and wave vectors of far-field induced transparency. In the second part of this chapter, we investigate the physics of the transition from weak to strong coupling between LSPRs and guided modes in a luminescent slab. For this purpose, we use a complementary system wherein the metallic nanoparticle array stands in, rather than on, a light-emitting waveguide. The transition from weak to strong coupling occurs as a function of the waveguide thickness. It is shown that this thickness modifies the coupling and loss rates of the modes in a non-trivial way. Hence, the waveguide thickness drastically modifies the light emission spectrum and directionality of the nanoantenna array.

Chapter 4 builds on the knowledge of SLRs presented in Chapter 2, to access the strong coupling regime between SLRs and excited electronic states (excitons) in organic molecules. This strong coupling leads to a hybrid light-matter quasi-particle called plasmon-exciton-polariton (PEP). The PEPs we investigate display an exceptionally light effective mass which is furthermore tunable via the periodicity of the array. This is relevant for the realization of a quantum condensed state of light and matter in a plasmonic system — a yet unreported phenomenon. Here, by optically pumping the sample we demonstrate that PEPs can thermalize, and their effective temperature cool upon increased optical pumping. Optical pumping also induces a saturation of the strong SLR-exciton coupling, which is explained with a phenomenological analytical model. Due to experimental limitations, condensation was not observed. Nevertheless, it is envisaged that the results in this chapter may serve as a stepstone for its future observation in periodic arrays of metallic nanoparticles.

Chapter 5 deals once more with the coupling between LSPRs and RAs in the presence of luminescent molecules, but with an additional complexity. In contrast to most plasmonic structures displaying a dominant electric dipole moment, the structures here investigated display enhanced magnetic and quadrupolar moments. This unconventional electromagnetic response is due to the tapering and height of the particles. We investigate tall metallic pyramids, rather than pillars. Previous work had established that enhanced magnetic and quadrupolar moments hold the key to tailor the ratio of forward to backward scattering in anomalous ways. Here, we demonstrate that periodic arrays of metallic nanopyramids can tailor the forward to backward light emission in unconventional ways. The pyramids we investigate are shown to operate distinctly at different frequencies, directing the emitted light of one color mostly in the forward direction, and of a different color in the backward direction. This new effect holds great promise for its application to solid-state light-emitting devices, where light that is emitted backwards into the device is often re-absorbed and limits the system's efficiency. Therefore, the results in this chapter provide a design principle for overcoming a long-standing problem of the increasingly present light-emitting device technology.

In Chapter 6 we combine a resonant metallic nanoparticle array, a liquid crystal, and a colloidal quantum dot waveguide, to create a tunable light source with unprecedented spectral and directional selectivity. This system supports hybrid plasmonic-photonic resonances which arise from the interaction between the nanoparticle array and the quantum dot waveguide. The liquid crystal provides the tuning mechanism via a temperature-dependent phase transition which modifies its optical properties. In turn, this transition modifies the resonance conditions of the coupled system, allowing us to actively control the emission wavelength and directionality via an applied heating. The narrow resonance linewidths of this system, in both wavelength and angle, enable strong emission enhancement peaks with a bandwidth of a few nanometers and an angular width of less than one degree. The results in this chapter pave the way for a new generation of light-emitting devices where the various effects discussed in the previous chapters, and in other works, could be actively modified.

Overall, the research presented in this thesis contributes to a deeper understanding of light-matter interactions at the nanoscale, and in particular to the field of plasmonics or metallic nano-optics. Many of the effects here discussed will serve to enable new functionalities for light-emitting devices. In fact, several patent applications related to this work have already been filed in collaboration with Philips Research. It is presently envisaged that large area ($> \text{cm}^2$) metallic nanoparticle arrays, such as those investigated here, may become an important future techonology in the field of solid-state lighting. For this to occur, important questions related to the overall system efficiency need to be explored in further detail. Furthermore, for applications intended to direct light into a limited angular cone, metallic nanoparticle arrays with higher rotational symmetry would be beneficial. Nonetheless, the general guidelines here presented for coupling light and matter in metallic nanoparticle arrays are expected to serve as a stepstone for the emergence of new physics and applications in the fascinating field of metallic nano-optics.

LIST OF PUBLICATIONS

This thesis is based on the following publications:

1. *Coupling Bright and Dark Plasmonic Lattice Resonances*, S.R.K. Rodriguez, A. Abass, B. Maes, O. T. A. Janssen, G. Vecchi, and J. Gómez Rivas, Phys. Rev. X **1**, 021019 (2011)**(Chapter 2)**
2. *Tailoring dispersion and eigenfield profiles of plasmonic surface lattice resonances*, A. Abbas*, S.R.K. Rodriguez*, J. Gómez Rivas, and B. Maes, ACS Photon. **1**, 61 (2014). **(Chapter 2)**
3. *Quantum rod emission coupled to plasmonic lattice resonances: A collective directional source of polarized light*, S.R.K. Rodriguez, G. Lozano, M. A. Verschuuren, R. Gomes, K. Lambert, B. De Geyter, A. Hassinen, D. Van Thourhout, Z. Hens and J. Gómez Rivas, Appl. Phys. Lett. **100**, 111103 (2012).**(Chapter 2)**
4. *Light-emitting waveguide-plasmon polaritons*, S.R.K. Rodriguez, S. Murai, M.A. Vershuuren and J. Gómez Rivas, Phys. Rev. Lett. **109**, 166803 (2012).**(Chapter 3)**
5. *From weak to strong coupling of localized surface plasmons to guided modes in a luminescent slab*, S.R.K. Rodriguez, Y. Chen, T.P. Steinbusch, M. A. Verschuuren, A.F. Koenderink and J. Gómez Rivas, submitted.**(Chapter 3)**
6. *Thermalization and cooling of plasmon-exciton-polaritons: Towards quantum condensation*, S.R.K. Rodriguez, J. Feist, M.A. Vershuuren, F.J. Garcia Vidal and J. Gómez Rivas, Phys. Rev. Lett. **111**, 166802 (2013). **(Chapter 4)**
7. *Surface lattice resonances strongly coupled to Rhodamine 6G excitons: tuning the plasmon-exciton-polariton mass and composition*, S.R.K. Rodriguez and J. Gómez Rivas, Opt. Express **21**, 27411 (2013). **(Chapter 4)**
8. *Breaking the symmetry of forward-backward light emission with localized and collective resonances in magnetoelectric nanopyramid arrays*, S.R.K. Rodriguez*, F. Bernal Arango*, T.P. Steinbusch*, M. Verschuuren, A.F. Koenderink and J. Gómez Rivas, submitted.**(Chapter 5)**

9. *Active liquid crystal tuning of plasmonic enhanced light emission from quantum dots*, A. Abbas*, S.R.K. Rodriguez*, T. Ako, T. Aubert, M.A. Verschuuren, D. van Thourhout, Z. Hens, J. Beeckman, J. Gómez Rivas, and B. Maes, submitted. **(Chapter 6)**

* Equal contribution

Other publications by the author:

1. *Variable modal excitation efficiency in plasmonic dolmens through nanoscale electron beam positioning*, T. Coenen, D. T. Schoen, B. J. M. Brenny, S. R. K. Rodriguez, S. Mann, A. Polman, and M. L. Brongersma, in preparation.

2. *New paths for efficient lighting*, G. Lozano, S. R. K. Rodriguez, and J. Gómez Rivas. Invited review article in preparation.

3. *Lichtemissie van roosters van nanoantennes*, S.R.K. Rodriguez, G. Lozano, M. Verschuuren and J. Gómez Rivas, Nederlands Tijdschrift voor Natuurkunde, January (2014).

4. *Near-field resonance at far-field induced transparency in diffractive arrays of plasmonic nanorods*, S.R.K. Rodriguez, O.T.A. Janssen, G. Lozano, A. Omari, Z. Hens and Jaime Gómez Rivas, Opt. Lett. **38**, 1238 (2013).

5. *Plasmonics for solid-state lighting: Enhanced excitation and directional emission of highly efficient light sources*, G. Lozano, D.J. Louwers, S.R.K. Rodriguez, S. Murai, O.T.A. Janssen, M.A. Vershuuren and Jaime Gómez Rivas, Light: Science & Applications, **2**, e66 (2013).

6. *Hybrid plasmonic-photonic modes in diffractive arrays of nanoparticles coupled to light-emitting optical waveguides*, S. Murai, M.A. Vershuuren, G. Lozano, G. Pirruccio. S.R.K. Rodriguez and Jaime Gómez Rivas, Opt. Exp. **21**, 4250 (2013).

7. *Collective resonances in plasmonic crystals: Size matters*, S.R.K. Rodriguez*, M.C. Schaafsma*, A. Berrier and J. Gómez Rivas, Phys. B: Condensed Matter, **407**, 4081 (2012).

8. *Coherent absorption and enhanced photoluminescence in thin layers of nanorods*, G. Pirruccio, G. Lozano, Y. Zhang, S.R.K. Rodriguez, R. Gomes, Z. Hens, and J. Gómez Rivas, Phys. Rev. B **85**, 165455 (2012).

9. *Universal Scaling of the Figure of Merit of Plasmonic Sensors*, P. Offermans, M.C. Schaafsma, S.R.K. Rodriguez, Y. Zhang, M. Crego-Calama, S.H. Brongersma, and J.Gómez Rivas, ACS Nano, **5**, 5151 (2011).

10. *Analysis of Voltage Spikes in Superconducting Nb_3Sn Magnets*, S. Rahimzadeh-Kalaleh, G. Ambrosio, G. Chlachidze, C. Donnelly, M. Tartaglia, IEEE Trans. Appl. Superconduct. **19**, 2442-2445 (2009).

11. *Reliability in the Fermilab Main Injector and Implications for the ILC*, M.A. Tartaglia, J. Blowers, D. Capista, D.J. Harding, O. Kiemschies, S. Rahimzadeh-Kalaleh, J.C. Tompkins, IEEE Trans. Appl. Superconduct. **18**, 338-341 (2008).

Conference proceedings:

1. *Diffractively induced transparency and extraordinary light emission at the plasmon band edge*, S.R.K. Rodriguez, proceedings of Metamaterials '2012: The Sixth International Congress on Advanced Electromagnetic Materials in Microwaves and Optics, pp. 788-790, St. Petersburg, Russia (2012).

Patents:

1. *Nanoantenna arrays for efficient and designed LED emission*, S. Rahimzadeh-Kalaleh Rodriguez, J. Gómez Rivas, R. Balkenende, M.A. Verschuuren, G. Lozano, S. Murai. Patent numbers US20130286633, CN103370803A, EP2477240A1, EP2666192A1.

2. *Luminescent solar concentrator with nanostructured luminescent layer*, D. de Boer, S. Rahimzadeh-Kalaleh Rodriguez, S. L. Diedenhofen, J. Gómez Rivas, WO patent application number PCT/IB2012/057116.

3. *Anisotropic enhanced emission from plasmonic coupled emitters for solid state lighting*, M. A. Verschuuren, S. Murai, S. Rahimzadeh-Kalaleh Rodriguez, G. Lozano, D. Louwers, D. de Boer, J. Gómez Rivas, M. Ivan. EU and US Patent Application in collaboration with Philips, Patent pending.

4. *Phosphor-converted plasmonic LED injecting in a light guide*, D. de Boer, M. A. Verschuuren, J. Gómez Rivas, S. Rahimzadeh-Kalaleh Rodriguez. EU and US Patent Application in collaboration with Philips, Patent pending.

ACKNOWLEDGMENTS

This thesis would have been impossible without the help and support from several people. Here, I would like to express my gratitude to them. Firstly, I thank my supervisor Jaime Gómez Rivas. Jaime: Thank you for your commitment to your students, your high ethical standards, and your openness in discussions. I have learned a lot from you — at both scientific and personal levels — during these past few years. I feel fortunate to have worked with you at the intersection between academic and industrial research. I thank you for accepting me in your group, for giving me freedom in research topics, and for making me feel that my voice was always heard. This was a great learning experience for me!

The beauty of experimental physics is more easily recognizable with high quality samples. In this sense, I feel fortunate to have worked so closely to Marc A. Verschuuren at Philips Research. All the metallic nanostructures in Chapters 3, 4, 5, and 6, were fabricated by Marc, so his contribution to these results has been pivotal. Thank you Marc for sharing your skill and expertise with us in a friendly manner, and for the many lively discussion we had.

As a member of the Surface Photonics group, I had the pleasure to meet many great colleagues: Silke Diedenhofen, Gabriele Vecchi, Vincenzo Giannini, Christophe Arnold, Audrey Berrier, Yichen Zhang, Grzegorz Grzela, Martijn Schaafsma, Gabriel Lozano, Giuseppe Pirruccio, Shunsuke Murai, Tom Steinbusch, Tommy Barten, Yannick Fontana, Giorgos Georgiou, Hemant Tyagi, Arkabrata Bhattacharya, Dick van Dam, Mohammed Ramezani, and Imre Dehner. While all of them have contributed to the well-being of the group, I would like to especially thank those who have contributed in a more direct way to my particular experience. Gabriel: Thank you for your friendship, for the numerous scientific and personal advices you gave me, and for your team-spirit. I enjoyed our time at Philips together, and thank you for the hard work that helped to consolidate the link between our group and Philips. Martijn: Thank you for your friendship, for the collaboration while you were at Philips, and for sharing our mutual enthusiasm for physics on numerous occasions. It was great to have you as a neighbor and that you came to my wedding in Mexico! Tom and Imre: Thank you for allowing me to provide guidance during the time we worked together. I especially acknowledge Tom for contributing to the results in Chapter 5, and Imre for pointing out some typographical mistakes in the first few chapters of this thesis. It was nice to work together. Shunsuke: Thank you for your important contribution to the results in Chapter 3, and for your kindness and dedication that made it nice to work with you. Grzegorz and Giuseppe: Thank you for being helpful at the lab and for many stimulating discussions. Giorgos: Thank you for the many exciting discussions we had, and for your great hospitality when I stayed at your place.

Thanks to the collaboration with Philips, I met many great people at the High-Tech Campus in Eindhoven. During most of my PhD, I attended weekly discussions of the Metamaterials project at Philips, for which I especially thank Marc Vershuuren, Manuela Lunz, Dick de Boer, and Remco van Brakel. I feel thankful for the opportunity to participate in an interesting synergy between fundamental and applied research. Thanks to Hans van Sprang, the leader of the Photonic Materials and Devices group, for ensuring a nice and safe working atmosphere at all times. I thank Hans Cillessen for his advice and assistance in numerous practical situations during my time at Philips. Multiple times during my PhD I was given the opportunity to set up a demo for visitors to see the practical relevance of enhancing light emission with metallic nanoparticle arrays. I appreciate the help of Paul van Hal and Hans Cillesen in setting up these demos. I thank Bas Keterlass for the fabrication of the gold nanorod arrays investigated in Chapter 2, and I thank Toon de Win for ellipsometry data that was helpful for the analysis of several results contained in this thesis. At Philips, I also had the pleasure to meet Olaf Janssen and Davy Louwers, students from Delft University collaborating with our group. Davy: Thank you for your great attitude and the extraordinary talent to work together on a scientifically challenging topic. It is a pity that our work together did not culminate in a publication, but I nevertheless learned a lot from you and I am thankful for that. Olaf: It was a pleasure to collaborate with you on numerous topics, and I enjoyed the time we worked together very much. Your great computational skills were very helpful in revealing several interesting properties of lattice resonances. At the High-Tech Campus, I also had the pleasure to meet Peter Offermans, from the Holst Centre. Thank you Peter for the collaboration, and for a nice paper together on the relevance of lattice resonances for sensing. Finally, I thank Pauline Deuning for her kind and helpful administrative assistance.

An important source of motivation during my PhD came from the numerous colloquia and poster sessions of the Center for Nanophotonics at AMOLF, to which I attended most Wednesdays. I thank the group leaders Albert Polman, Kobus Kuipers, Femius Koenderink, Ad Lagendijk, Ewold Verhagen, Yves Rezus, and Eric Garnett, for ensuring a lively discussion and a rigorous training for us students. The Nanophotonics colloquia have been a major platform for improving my presentation skills, and I am extremely grateful for that. I would like to especially acknowledge Femius Koenderink, with whom I had the pleasure to collaborate in relation to the results in Chapters 3 and 5. Femius: Thank you for the many stimulating discussions, your sharp and critical comments that helped me to deepen my understanding and improve my clarity, and for your openness to collaborate. I was also fortunate to meet many friends and colleagues at AMOLF

to whom I am grateful for being a great source of scientific stimulus. In particular, I acknowledge Sander Mann, Felipe Bernal, and Toon Coenen, with whom I had the pleasure to collaborate in depth in different projects. Working with you guys was very much enjoyable! I also acknowledge Hinke Schokker and Claire van Lare for their kind and friendly assistance a couple of times I visited labs at AMOLF. I also acknowledge Yuntian Chen, former post-doc at AMOLF, with whom I started a collaboration through Femius. Thank you Yuntian for your contribution to the results in Chapter 3, and for your positive attitude while working together. I also thank the entire support staff at AMOLF for making AMOLF such a pleasant and smooth place to work at. In this sense, I particularly thank Albert Polman and Vinod Subramian, who are the former and current directors of AMOLF, for ensuring that things flow smoothly at the institute, and for making it stand out in the outside world as a great place to work at! Last but not least, I thank Anouk Nelissen and Roos Luthart for a friendly and helpful administrative assistance, and Henk-Jan Boluit for providing several creative and beautiful graphics I used in publications and presentations.

Since my second Masters year at Ghent University (2009-2010), I have enjoyed a fruitful and continuous collaboration with several people at Ghent. I am thankful to Aimi Abass and Bjorn Maes for many stimulating discussions, for their friendly and positive outlook on the projects we undertook together, and for their important contribution to the numerical results in Chapters 2 and 6. Besides being a great scientific partner, Aimi has also been a great friend for many years, and I am thankful to him for that. From Ghent University, I would also like to acknowledge Zeger Hens for a long standing collaboration, in which several of his group members (Tangi Aubert, Abdoulghafar Omari, Raquel Gomes, Yolanda Justo, Karel Lambert, and Bram de Geyter) have provided quantum dots that we have studied in combination with metallic nanoparticle arrays. I feel fortunate to have taken a course with Zeger at Ghent, and to continue collaborating with his group since then. Also from Ghent University, I thank Jeroen Beeckman and Thomas Ako for contributing with their expertise in liquid crystals to the results in Chapter 6, and for several stimulating discussions. I also thank Dries Van Thourhout for advice on the results in Chapter 6.

In 2013, I had the pleasure to visit for 8 weeks the theory group of Francisco J. García Vidal at Universidad Autonoma de Madrid (UAM). There, I was fortunate to engage in many inspiring discussions with Francisco and with Johannes Feist. I am very thankful for their friendly spirit and for their constructive criticism. Their contribution to the interpretation of the results in Chapter 4 was very important. I thank Paloma Arroyo Huidobro for receiving me so friendly in Madrid, and taking care of the practical matters of my visit. I also enjoyed many interesting discussions with several people at Madrid, and I especially thank Jorge Bravo, Juan Antonio Porto, Esteban Moreno, Felix Rüting, Zhang Pu, Alexandre Delga, Diego Martín, Carlos González, Javier Cuerda, and Ricardo Quesada. In the last few days of my stay at Madrid I had the pleasure to meet Francesca Marchetti, also at UAM. I enjoyed many inspiring discussions with Francesca, and I am very thankful for her critical advice on the results in Chapter 4.

During the writing of this thesis I received various comments from the committee members whose names are written in the opening pages of this thesis. I would like to thank them all for their encouraging words and their critical advice which helped me to improve several aspects of this book. In particular, I take the opportunity to thank Andrea Fiore, who is the second promotor for this thesis.

Last but not least, I thank my family for their loving support. To my wife Marina: Thank you for being the most loving, caring, and comprehensive companion I could ever dream of. Thank you for making my happiness grow, and my disappointments fade. To my parents Abbas and Genoveva: Thank you for your continuous love and support throughout my life. I feel blessed to be your son, and none of this would have been possible had it not been because of your unbending belief in me.

To all of you, Thank you.
Said

ABOUT THE AUTHOR

Said Rahimzadeh-Kalaleh Rodriguez was born in 1983 in Monterrey, Mexico. He studied Engineering Physics at Embry-Riddle Aeronautical University in the USA, and graduated with Magna Cum Laude Honors in 2008. Afterwards, he was awarded a full scholarship by the European Commission to study the Erasmus Mundus Masters of Science in Photonics. He studied the first Masters year at the Royal Institute of Techonolgy (KTH), Sweden, and the second Masters years at Ghent University, Belgium. He completed the Masters with the Greatest Distinction, and his thesis entitled "Light scattering and quantum dot emission close to nanoantenna arrays" was co-awarded the best thesis prize by a consortium of 5 European Universities. In 2010, Said started his PhD studies in the Surface Photonics group under the supervision of Jaime Gomez Rivas, in the context of an industrial partnership program between FOM Institute AMOLF and Philips. His PhD research focuses on the physics and applications of metallic nanoparticle arrays coupled to light emitters. Said has co-authored 15 peer-reviewed scientific publications (plus several more under review), filed for 4 patents, given 14 talks at national and international conferences, won the best student paper presentation at two international conferences (2012 Metamaterials Congress in Russia, and 2014 SPIE Photonics Europe - Photonic Crystal Materials and Devices), was one of three finalists at the 2014 Dutch national physics society young speaker contest, and serves regularly as reviewer for several scientific journals.

In his free time, he enjoys the company of his wife Marina, traveling, listening and playing music (guitar and piano), and learning physics.